Joint Institute for Nuclear Research

FUNDAMENTAL INTERACTIONS & NEUTRONS, NUCLEAR STRUCTURE, ULTRACOLD NEUTRONS, RELATED TOPICS

XXXII International Seminar on Interaction of Neutrons with Nuclei

Dubna, May 24–30, 2026

Proceedings of the Seminar

Dubna • 2026

УДК 539.125.5(042)
ББК 22.383.2я431+22.383.5я431+22.383.25я431
F97

Organized by

Frank Laboratory of Neutron Physics, JINR, Dubna
China Spallation Neutron Source Science Center (CSNS), China
State Key Laboratory of Intense Pulsed Radiation Simulation and Effect,
Northwest Institute of Nuclear Technology (NINT), China

The contributions are reproduced directly from the originals presented by the Organizing Committee.

F97 **Fundamental** Interactions & Neutrons, Nuclear Structure, Ultracold Neutrons, Related Topics: Proceedings of the XXXII International Seminar on Interaction of Neutrons with Nuclei (Dubna, May 24–30, 2026). — Dubna: JINR, 2026. — 131 p.

ISBN 978-5-9530-0682-8

This collection of papers reflects the present state of neutron-aided investigations of the properties of the nucleus, including fundamental symmetries, properties of the neutron itself, neutron-excited reactions, and the parameters of the nucleus that determine the reaction cross section, as well as the latest theoretical development of all these problems. The works on experimental investigations in the physics of fission by neutrons of various energies are presented in great detail. The present state of experiments on the physics of ultracold neutrons and facilities to obtain them is described at length. The status achieved by now of the latest (from the viewpoint of technique) experiments and environment studies is covered as well.

Фундаментальные взаимодействия и нейтроны, структура ядра, ультрахолодные нейтроны, связанные темы: Труды XXXII Международного семинара по взаимодействию нейтронов с ядрами (Дубна, 24–30 мая 2026 г.). — Дубна: ОИЯИ, 2026. — 131 с.

ISBN 978-5-9530-0682-8

В сборнике представлено современное состояние исследований свойств ядра с помощью нейтронов: фундаментальных симметрий и свойств самого нейтрона, возбуждаемых им реакций и параметров ядра, определяющих их сечения, а также последние теоретические разработки всех этих вопросов. Очень детально представлены работы по всем аспектам, связанным с экспериментальными исследованиями физики деления ядра нейтронами различных энергий. Достаточно полно описано современное состояние экспериментов по физике ультрахолодных нейтронов и установок для их получения, а также достигнутый к настоящему времени статус методически новейших экспериментов и результаты экологических исследований.

УДК 539.125.5(042)
ББК 22.383.2я431+22.383.5я431+22.383.25я431

ISBN 978-5-9530-0682-8

© Joint Institute for Nuclear Research, 2026

ORGANIZING COMMITTEE

Conference Chairs

Egor Lychagin (JINR) Dongwei Hei (NINT) Sheng Wang (CSNS)

Directors of Local Organizing Committee

Walter Furman (JINR) Mengtong Qiu (NINT) Tianjiao Liang (CSNS)

Scientific Secretaries

Inga Zinicovscaia (JINR) Xiufeng Weng (NINT) Ruirui Fan (CSNS)

Committee Members

Polina Filonchik (JINR) Constantin Hramco (JINR) Yuri Kopatch (JINR)
Ludmila Mitsyna (JINR) Alexander Nezvanov (JINR) Valery Shvetsov (JINR)
Zhanna Sorokina (JINR) Nikita Yushin (JINR) Maxim Zakharov (JINR)
Xichao Ruan (NINT) Tianjiao Liang (CSNS) Xin Tong (NINT)
Xiao Li (CSNS) Liang Sheng (NINT) Quanlin Shi (NINT)
Wei Chen (NINT)

Secretariat

Diana Al-Maaita (JINR) Elena Kopach (JINR) Jianxin Zhang (NINT)
Haoqing Li (NINT) Bochen Wang (NINT) Zhaofeng Su (NINT)
Wei Jiang (CSNS) Yonghao Chen (CSNS)

CONTENTS

Preface ……6

Adiabatic Spin Flipper for Resonance Neutrons in a Spatially Varying Magnetic Field
Akmaletdinov R.D., Kuznetsov V.L., Rebrova N.V., Voynov V.S., Pchelnikov V.V., Sedyshev P.V., Smolyanov I.A. **……7**

Characterization of Secondary Activated Elements Generated during the Production of ^{18}F-Fluorodeoxyglucose Using Cyclotron at INCART
Coronado E.M., Montero F. **……..13**

Coincidence-Summing Effects and Positronium-Annihilation-Photon Lines Appearing in CNT-Enhanced NaI(Tl)-Detector Response to ^{60}Co- and ^{137}Cs-Decays
Grushevskaya H.V., Timoshchenko A.I. **……...21**

Predictions of Asymptotic Correlation Function of Scattered Neutrons Oscillations Based on Algebraic Theory of Spontaneous Symmetry Breaking
Gudkov E.L. **…….....28**

Search and Analysis of the Double Hit Events in the Study of (γ, f) Reactions
Kamanin D.V., Pyatkov Yu.V., Zhuchko V.E., Solodov A.N., Vilane T.H., Goryainova Z.I., Strekalovsky O.V., Kuznetsova E.A., Zhukova A.O., Sereda Yu.M., Ngcobo P.Z., Le B.A. **……...40**

The Process Opposite to the Neutron Radiative Decay
Khafizov R.U., Semenov S.V. **……...46**

Conversion of the Monte-Carlo Neutron Transport Program Code 'SHIELD' to Work Together with the 299-Group Cross Sections of Neutron–Nucleus Interactions 'ABBN-93'
Sobolevsky N.M., Djilkibaev R.M., Khliustin D.V. **……52**

Measurement of Holmium-165 Spectra at the INES TOF Spectrometer of the Spallation Neutron Source RADEX
Djilkibaev R.M., Khliustin D.V. **……...61**

Investigation of Low-Energy *p*-Wave Resonance of ^{35}Cl Nucleus at the IREN Facility
Kuznetsov V.L., Golubkov E.A., Kopatch Yu.N., Mitsyna L.V., Rebrova N.V., Rogov A.D., Sedyshev P.V., Yergashov A. **.....77**

About a Possibility to Obtain the Forward-Backward Asymmetry of Gamma Emission Studying the ^{81}Br(n, γ) Reaction
Kuznetsov V.L., Mitsyna L.V., Oprea A.I., Oprea C., Rebrova N.V., Sedyshev P.V. **.....87**

System of Thermal Stabilization of BGO Scintillation Detectors
Lihachev A.N., Akmaletdinov R.D., Kopatch Yu.N., Kuznetsov V.L., Mitsyna L.V., Rebrova N.V., Sedyshev P.V., Yergashov A. **.....94**

From Fermi Total Reflection & Tunneling of Cold Neutrons to Their Trapping in Fabry–Perot Nano-Resonators within the Picosecond Time Regime Precision
Maaza M. **.....98**

Monte Carlo Simulation of the Multi-Detector System of the FISCO Facility
Olkhovich N.M., Tiagelskaia A.M., Vorobyev A.S. **.....105**

Phytoremediation Potential of *Eichhornia crassipes* for Heavy Metal Removal from Industrial Wastewater Assessed by TXRF
Pham Thi Ngoc Ha, Nguyen Thi Nguyet Ha, Nguyen An Son, Le Hong Khiem, Zinicovscaia I., Vu Duc Cong, Nguyen Thi Minh Sang **.....111**

Modeling of the Neutron Beam Parameters of the Time-of-Flight Spectrometer GNEIS Using GEANT4
Tiagelskaia A.M., Olkhovich N.M., Vorobyev A.S. **.....126**

Preface

The annual International Seminar on Interactions of Neutrons with Nuclei (ISINN-32) was convened from 24 to 30 May in Dubna, Russia. On this occasion, ISINN was jointly organized by its founder and longstanding coordinator, the Frank Laboratory of Neutron Physics (FLNP) of JINR, together with the China Spallation Neutron Source Science Center (CSNS) and the State Key Laboratory of Intense Pulsed Radiation Simulation and Effect (NINT). The conference brought together 164 participants representing JINR laboratories (FLNP, VBLHEP, FLNR, DLNP, and BLTP) and ten countries, among them the People's Republic of China, the Socialist Republic of Vietnam, the Arab Republic of Egypt, the Republic of India, the Russian Federation, and the Republic of Serbia. The programme comprised a total of 5 plenary, 24 invited, 75 oral, and 48 poster presentations (see https://indico.jinr.ru/event/5590/ for more details).

Opening the Seminar, E.V. Lychagin, Co-Chairman of the Organizing Committee and Director of the FLNP, expressed his particular satisfaction at welcoming the participants of ISINN-32 to Dubna. Prof. Tianjiao Liang, Vice Director of the CSNS, conveyed his gratitude to his colleagues in Dubna for their efforts in organizing ISINN-32 — a conference that has gathered scientists from across the world annually for thirty-two consecutive years. The participants of the Seminar were addressed by Dr. Sergey Kulikov, Vice Director of the JINR, who expressed his hope that the traditional exchange of knowledge between experienced and early-career researchers would be sustained. The considerable participation of young scientists from all countries participating in this conference was noted as an indication that neutron research possesses a promising future.

The plenary sessions were opened with plenary talks by Egor Lychagin "Current state of development of a new perspective neutron source for FLNP JINR", Ruirui Fan "Current status and experiments of the CSNS and its upgrade project CSNS-II ", and invited talks by Tianjiao Liang “Design of neutron physics and application instrument of CSNS (PGNNA/NDP/UCN)”, Anatolii Serebrov “Precise research of neutron decay and the need for Standard Model extension. Baryonic and lepton asymmetries of the Universe”, and Inga Zinicovscaia "Instrumental neutron activation analysis at the IBR-2 reactor: current status".

The second half of the first day, together with the second and fourth days of the Seminar, was conducted in the format of two parallel sessions and a joint two-hour poster session. These sessions addressed the traditional themes of the Seminar, ranging from the fundamental properties of the neutron to modern neutron sources, and from promising experiments in the fields of nuclear fission and fast-neutron-induced nuclear reactions to reactor physics and experimental methodology. As is customary, investigations employing nuclear and related analytical techniques in the environmental and materials sciences were extensively represented.

This year, the Organizing Committee proposed publishing the conference proceedings as original scientific papers in *Physics of Elementary Particles and Atomic Nuclei, Letters* (PEPAN Letters), *Chinese Physics C*, and *Natural Science Review*. Accordingly, only those proceedings that fell beyond the scope of these journals or were submitted directly for publication in the present volume are included herein. Nevertheless, we greatly appreciate the valuable contribution of each participant to the 32nd ISINN Seminar!

Co-director of the ISINN-32 Organizing Committee
Walter Furman

Adiabatic Spin Flipper for Resonance Neutrons in a Spatially Varying Magnetic Field

R.D. Akmaletdinov[2], V.L. Kuznetsov[1,3], N.V. Rebrova[1], V.S. Voynov[2], V.V. Pchelnikov[1], P.V. Sedyshev[1], I.A. Smolyanov[2]

[1]*Frank Laboratory of Neutron Physics, Joint Institute for Nuclear Research, Dubna*
[2]*Institute of Physics and Technology, Ural Federal University, Yekaterinburg, Russia*
[3]*Institute for Nuclear Research of the Russian Academy of Sciences, Moscow, Russia*

Introduction

Polarized neutron beams are widely used in fundamental and applied research. In experiments carried out at the flight path No. 4 of the IREN facility ("Gamma-7") in preparation for experiments with polarized neutrons, it became necessary to develop a device capable of reversing the orientation of the neutron beam polarization vector by 180° relative to the direction of beam propagation. In the present work, the theoretical design and computational modeling of an adiabatic spin flipper were carried out. Numerical simulations of the magnetic field and heat generation in the coil systems were performed in COMSOL Multiphysics using the «Magnetic Fields» and «Heat Transfer in Solids» modules.

Design and Parameters of the Adiabatic Spin Flipper

The experimental study of polarized neutron beams requires an evaluation of the degree of beam polarization. This quantity is determined from the measured intensities (counts) of according to the following formula:

$$f \cdot P_a(\lambda)P_p(\lambda) = \frac{N^+ - N^-}{N^+ + N^-},$$

where f is a spin reversal probability, $P_a(\lambda)$ and $P_p(\lambda)$ are polarizations of the neutron beam at the exit of the analyzer and polarizer, N^+, N^- are the numbers of neutrons in the beam, polarized along and against the selected direction, correspondingly.

A spin flipper is a device that reverses the orientation of the neutron beam polarization vector by 180° relative to the direction of the guiding magnetic field. In the spin flipper, the neutron magnetic moment μ_n interacts with the magnetic field.

The neutron spin precesses around the magnetic field vector B with the Larmor frequency ω_L:

$$\omega_L = \gamma_n B,$$

where γ_n is the gyromagnetic ratio. The rate of change of the magnetic field direction along the neutron trajectory is:

$$\omega_B = \frac{d\varphi}{dt} = \frac{d\varphi}{dz} \cdot \frac{dz}{dt}.$$

The adiabaticity parameter is defined as:

$$K = \frac{\omega_L}{\omega_B} = \frac{LB}{119\sqrt{E_n}},$$

where L is the length of the spin-flip region, and B is the constant magnitude of the resultant field.

Values above 10 correspond to the adiabatic regime, lower values do not. The magnitude of the magnetic field can be expressed as:

$$B \geq \frac{1190\sqrt{E_n}}{L}.$$

In our case, the neutron beam propagates along the y-axis:

$$\vec{B}(y) = B_x(y)\vec{e}_x + B_y(y)\vec{e}_y + B_z(y)\vec{e}_z.$$

The idealized field model corresponding to a smooth rotation of the magnetic induction vector at an almost constant field magnitude can be written as

$$B_x(y) = Bcos\left(\frac{\pi y}{L}\right), \quad B_z(y) = -Bsin\left(\frac{\pi y}{L}\right).$$

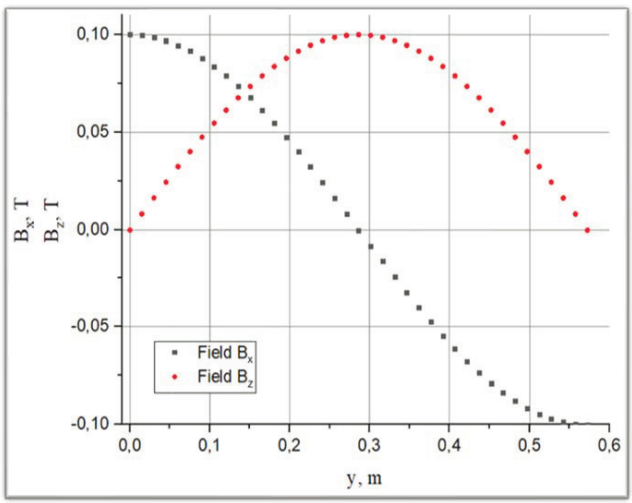

Figure 1. Idealized spatial distributions of the magnetic field components $B_x(y)$ and $B_z(y)$ in the spin-flip region.

Technically, this configuration is implemented by two coll systems that generate the transverse B_x and longitudinal B_z components of the magnetic field.

The spin flipper is a 570 mm long magnetic system with a target magnetic induction in the working gap of up to 1000 G. The required field configuration is provided by two C-shaped permalloy cores and a set of excitation coils. One core is positioned within the cutout of the other. The first core forms the transverse component of the magnetic field, while the second forms the longitudinal component. An additional coil system generates the negative transverse component. Coils 4 and 5 have 50 turns each and operate at a current of 70 A. The pair of rectangular coils has 25 turns and operates at 300 A.

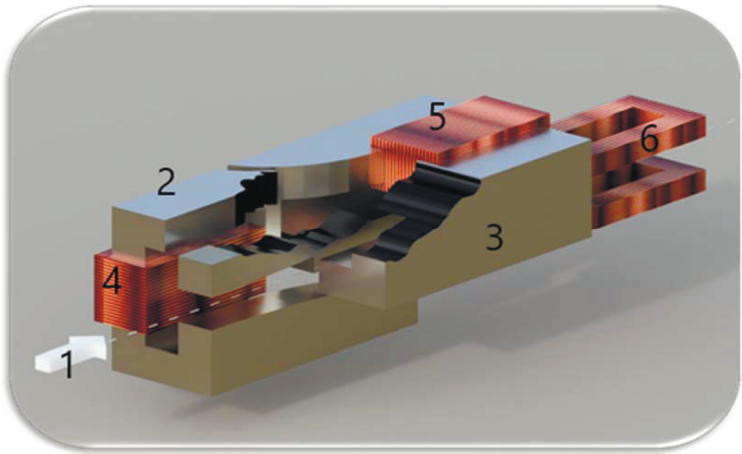

Figure 2. Adiabatic spin flipper. (1) Neutron beam aperture; (2) first magnetic core; (3) second magnetic core; (4) coil of the first magnetic core; (5) coil of the second magnetic core; (6) rectangular coils.

Control Scheme for a Pair of Rectangular Coils

The electronic control unit provides power supply and commutation for a pair of coils of the adiabatic spin flipper. It includes an input three0phase rectifier, a DC link, a high-frequency DC/LC converter, an output LC filter, a polarity-switching H-bridge, current measurement, stabilization and protection units, as well as a PWM controller and gate drivers for the power switches. The circuit operates in two modes – with spin flip and without spin flip – and provides current stabilization while limiting ripple to 1–5%.

Results and Discussion

Numerical simulation showed that the required field configuration is achieved through the combined action of the C- shaped magnetic cores and the coil system. At the same time, the magnetic field in the gap does not exceed 1000 G, since the permalloy enters the saturation region.

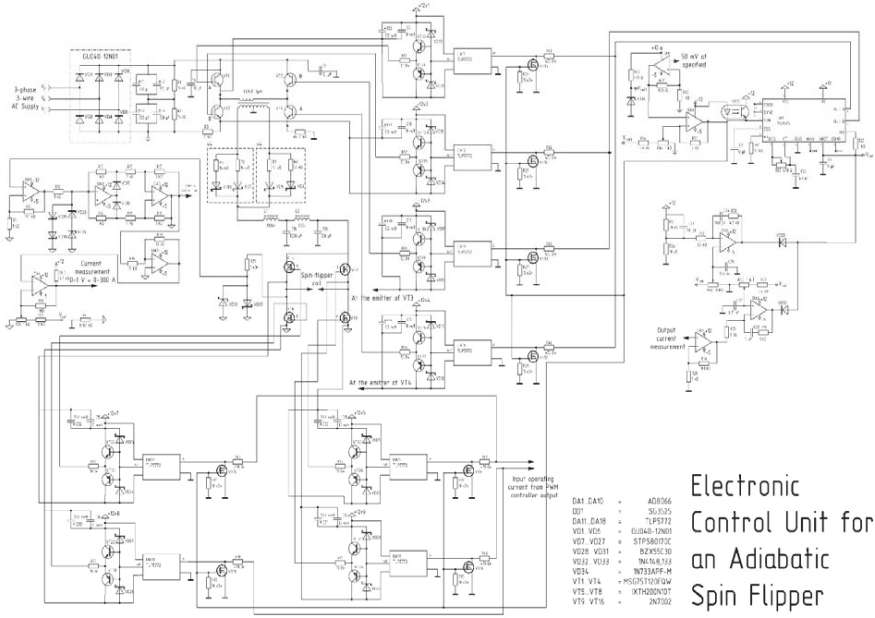

Figure 3. Electronic control and power supply circuit for a pair of spin-flipper coils.

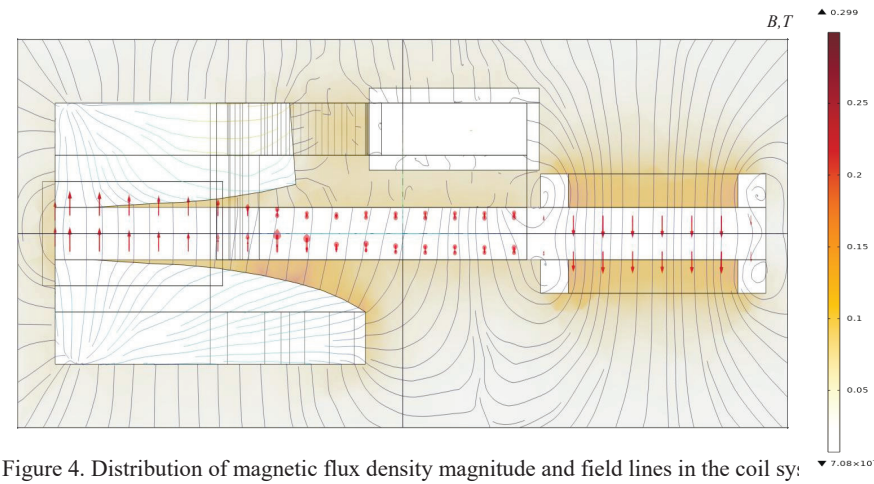

Figure 4. Distribution of magnetic flux density magnitude and field lines in the coil sy
obtained in COMSOL Multiphysics 6.3.

The calculated approximation formula for $B_x(y)$ and $B_z(y)$ takes the form:

$$B_x(y) = 0{,}00338 + 0{,}05882\left[tg\left(\frac{y-0{,}15102}{0{,}02613}\right) - tg\left(\frac{y-0{,}39404}{0{,}02613}\right)\right],$$

$$B_z(y) = 0{,}00242 - 0{,}04777 \cdot tg\left(\frac{y-0{,}17095}{0{,}05626}\right) - 0{,}05100 \cdot tg\left(\frac{y-0{,}40034}{0{,}01038}\right).$$

The structure has a considerable mass of about 48 kg, of which approximately 40 kg corresponds to the core. A more practical solution would be a magnetic core made of electrical steel assembled from laminated sheets. Since direct currents are used in the system, eddy currents in the core are absent. At the same time, the third coil requires water cooling because it operates at a high current density. The C-shaped elements must also be rigidly mechanically fixed, since their mutual arrangement determines the resulting field configuration in the working gap.

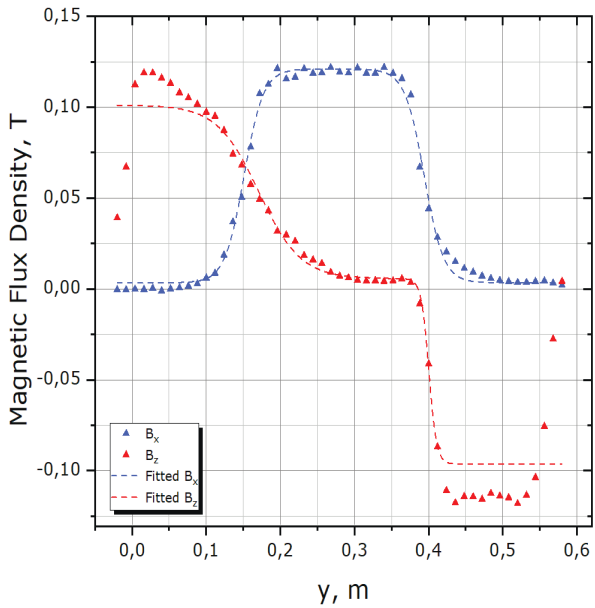

Figure 5. Distribution of magnetic flux components $B_x(y)$ and $B_z(y)$ along the spin-flipper axis.

The calculated adiabaticity parameter of the spin flipper is K = 24, which means that the adiabaticity condition is satisfied for neutrons with an energy of 400 eV.

Conclusions

The initial concept of an adiabatic spin flipper was based on the coil-based approach described by J.D. Bowman. However, in the present work this idea was further developed into a different structural implementation adapted to the operating conditions of the IREN. Numerical modeling showed that the proposed magnetic-core configuration is capable of forming the required field distribution in the working gap while preserving compact dimensions. At the same time, the study revealed important practical limitations related to core saturation, total mass, mechanical fixation of the C-shaped elements, and the need for water cooling of the third coil.

References

1. J.D. Bowman, S.I. Penttilä, and W.B. Tippens, Nucl. Instrum. Methods Phys. Res. A 369, 195–204 (1996).
2. Yu.G. Abov, A.D. Gulko, P.A. Krupchitsky, Polarized slow neutrons, Atomizdat, 1966 (in Russian).
3. I.A. Smolyaninov, F.N. Sarapulov, S.F. Sarapulov, S.A. Bychkov, F.E. Tarasov, Matematical modelling of electromechanical installations using Comsol Multiphysics, Publishing office of the Ural University, 2021 (in Russian).

Characterization of Secondary Activated Elements Generated during the Production of ^{18}F-Fluorodeoxyglucose Using Cyclotron at INCART

E.M. Coronado[1] and F. Montero[1,2]

[1]*School of Chemistry, Science and Technology Faculty, Pedro Henríquez Ureña National University (UNPHU), Santo Domingo, Dominican Republic*
[2]*National Cancer Institute Rosa Emilia Sanchez Perez de Tavares (INCART), Santo Domingo, Dominican Republic*

Nuclear medicine has emerged as a fundamental tool in oncological diagnosis, establishing the radiopharmaceutical ^{18}F-fluorodeoxyglucose (18F-FDG) as one of the most widely used in PET studies. In the Dominican Republic, the National Cancer Institute Rosa Emilia Sánchez Pérez de Tavares (INCART) leads its production using an 18 MeV cyclotron. This research focuses on the characterization of secondary activated elements generated during this process. Using gamma spectroscopy, radionuclides were identified in components such as the target, synthesis filters, and cooling water. The results confirmed the presence of activation products such as ^{93}Mo in the target and validated the effectiveness of radioactive waste management protocols, demonstrating regulatory compliance and the environmental safety of the operations.

Introduction

The growing demand for radiopharmaceuticals, driven by the high incidence of cancer, has increased the generation of radioactive waste in production centers such as INCART. The process of accelerating protons to bombard a cyclotron target containing ^{18}O enriched water involves collateral challenges inherent to nuclear physics. During irradiation, the proton beam does not interact exclusively with the target material; it also impacts structural components of the system, such as separation foils and the metallic body of the target.

This interaction produces secondary nuclear reactions that “activate” these materials, generating radionuclides with both long and short half-lives that are not part of the final product but constitute radioactive waste that must be rigorously managed.

The main objective of this work is to describe and characterize these secondary radioactive elements. The study seeks to answer questions regarding which specific radionuclides are produced, how they affect the environment, and to evaluate the management of these wastes in relation to national and international (IAEA) regulations.

General description of the experiment

The study was conducted at the Cyclotron and Radiopharmacy Center facilities of the National Cancer Institute Rosa Emilia Sánchez Pérez de Tavares (INCART). A descriptive and experimental field research design was adopted in order to perform a comprehensive radiological characterization of the byproducts generated during the synthesis of ^{18}F-FDG.

The methodology was based on the qualitative and quantitative identification of radionuclides using gamma spectrometry techniques. The experimental protocol consisted of the selection and monitoring of critical components of the production system, including the niobium

target, the purification cartridges of the synthesis module, and the coolant fluid, in order to determine their activation profile after irradiation with 18 MeV protons.

Sample collection and preparation

For the characterization of secondary activated elements, representative samples from the different stages of the production and waste management process were selected:

- **Niobium Target:** A thallium-doped niobium target (Nb(Tl)) removed from operation in 2019 was analyzed. This sample was selected to identify long-lived isotopes that persist after an extended decay period, allowing the isolation of the activity of metallic activation products.
- **^{18}F Pre-synthesis:** Samples of freshly produced fluorine-18 were collected prior to entering the synthesis module. Due to the initially high specific activity, a serial dilution protocol using distilled water was performed, as illustrated in Figure 1. This procedure aimed to reduce the activity to measurable levels that would not saturate the Thallium-doped sodium iodide (NaI(Tl)) scintillation detector for the multichannel analyzer (MUCHA) (dead time < 10%) and would allow observation of the natural decay curve.

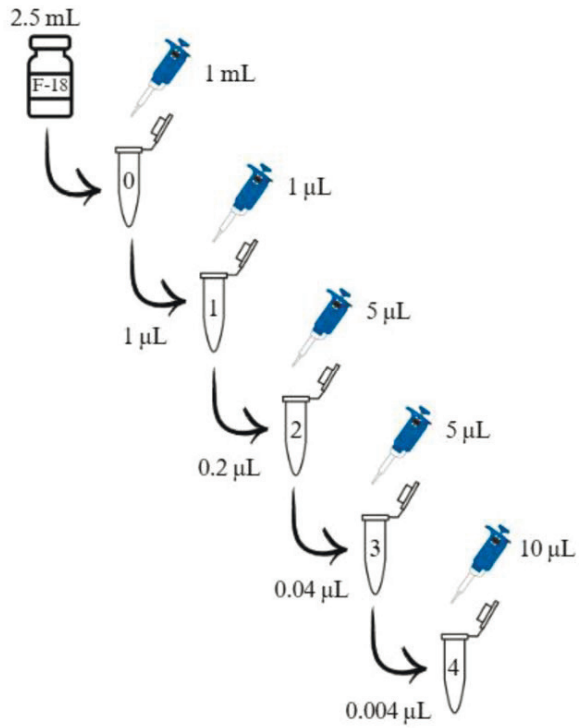

Figure 1: Representative diagram of serial dilutions of pre-synthesis ^{18}F.

The presented measurements correspond to the dilution identified in the diagram of Figure 1 as number 1. The results of this dilution are shown because the spectra obtained from the analysis of this sample were the most clearly defined.

The dilution of ^{18}F was measured a total of 11 times over a period of 18 hours until it reached 0.000 MBq in the dose calibrator. Table 1 presents the measurement number, activity, and elapsed hours for the dilution containing 1 μL of ^{18}F.

Table 1: Activity behavior in the ^{18}F dilution

Measurement Number	Activity (MBq)	Elapsed Time (h)
1	1.952	0
2	1.469	1
3	1.029	2
4	0.787	3
5	0.676	4
6	0.525	5
7	0.174	14
8	0.103	15
9	0.065	16
10	0.039	17
11	0.000	18

- **Synthesis Filters:** Consumable components from the Synthera synthesis module were collected after a standard production cycle. The samples included QMA ion-exchange filters (for 18F conditioning), 18C columns (for purification), alumina cartridges, and SCX filters. These samples were stored in lead containers and analyzed after a 24-hour decay period.
- **Cyclotron cooling water:** A 1 mL aliquot was extracted from the closed-loop target cooling system (target cavity water) to evaluate the possible migration of radionuclides or corrosion products into the cooling system.

Table 3 provides information on geometry sizes of the targets, their total masses, areal densities and homogeneity, as well as target masses and activities.

To determine the scaling factor (N_{Pu2}/N_{U5}), we made α-spectrometry of the active spots with surface barrier detector in precisely known geometry.

Instrumentation

For radionuclide identification, the gamma spectrometry technique was employed using a Multichannel Analyzer (MUCHA) with a NaI(Tl) scintillation detector. The spectral acquisition time was set to 8 minutes (480 seconds). Additionally, a dose calibrator was used to measure the total activity of the samples.

Results and discussion

Gamma energy spectra

In the gamma spectra obtained from the crude (pre-synthesis) 18F samples, the characteristic peaks and interaction phenomena of the radionuclide were clearly identified, as shown in Figure 2. The spectral profile is dominated by the photoabsorption peak at 511 keV, corresponding to the positron annihilation of ^{18}F, accompanied by the Compton edge at ~ 640 keV and a detectable sum peak at 1300 keV.

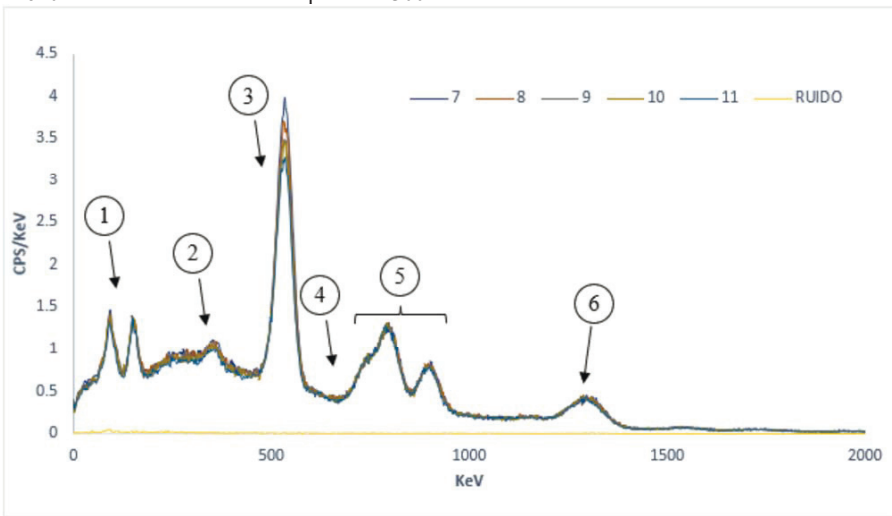

Figure 2: Gamma spectra of pre-synthesis ^{18}F.

Table 2: Peak identity and end energy in pre-synthesis ^{18}F

Peak Number	Peak Identity	Energy
1	X-ray Escape Peak	~ 100 ~ 160 KeV
2	Backscatter Peak	350 KeV
3	^{18}F	~ 511 KeV
4	Compton Edge	~ 640 KeV
5	Multiple Compton	720-950 KeV
6	Sum Peak	1300 KeV

The details of the energy composition are systematized in Table 2, where additional components such as the backscatter peak and multiple scattering events are presented.

The absence of photopeaks unrelated to the characteristic signature of ^{18}F suggests that there is no significant presence of impurities or secondary activated elements in the liquid precursor generated by the cyclotron. This validates the radionuclidic purity of the material intended for the synthesis of ^{18}FDG.

On the other hand, the analysis of the niobium target removed in 2019 revealed a distinct isotopic composition, characterized by long-lived radionuclides derived from neutron and proton activation of the structural material.

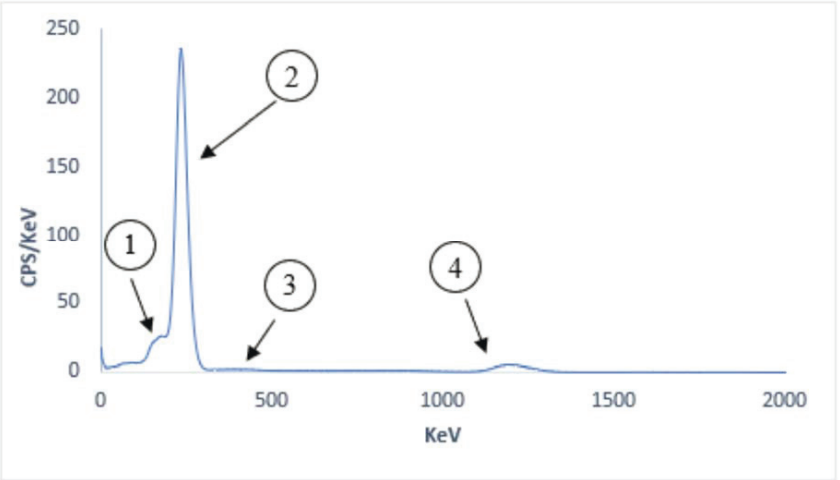

Figure 3: Gamma spectra of target used in cyclotron.

Table 3: Peak identity and energy of 2019 cyclotron target

Peak Number	Peak Identity	Energy
1	Backscatter Peak	$\sim 100 \sim 180$ KeV
2	^{93m}Mo	~ 234 KeV
3	Multiple Compton	$\sim$ 300-900 KeV
4	Sum Peak	1300 KeV

The isotope ^{93}Mo was prominently identified at $\sim$ 234 keV, a byproduct of the reaction shown in Equation 1.

$$^{93}Nb + p \rightarrow {}^{93m}Mo + n$$

Environmental impact indicators

To evaluate the environmental impacts, the critical stages of the radiopharmaceutical production process were correlated with the generated waste. This analysis was systematized using the Pres sure–Status–Response framework, whose results are summarized in Table 4.

Figure 4 illustrates the residual activity concentration (expressed in Bq/kg) in the different components of the ^{18}F-FDG synthesis process that presented detectable radioactivity (target and filters). A logarithmic scale was used to facilitate the visualization of the magnitude differences among the elements.

The analysis of the cooling water did not reveal radiological activity above natural background levels after 24 hours of decay; consequently, the corresponding spectra are omitted from this report.

Table 4: Pressure-Status-Response Indicators

Stage/System	Pressure Indicator	Status Indicator	Response Indicator
Radionuclide Production (Cyclotron)	Cyclotron operation generating ^{18}F	Highly radioactive target (Bq/kg)	Contain the target until activity decreases to safe levels through decay.
Synthesis (Synthera)	Synthesis generating ^{18}F-FDG	Radioisotopes in filters (Bq/kg)	Keep cartridge in hot cells after production for 24 hours.
Cooling System using High-Purity Water	Nuclear activation of water	Activity present in water (Bq/mL)	Retain water after production until activity decreases by decay.
Environmental Factors	Natural disasters	Structural damage (physical integrity)	Structural reinforcement.

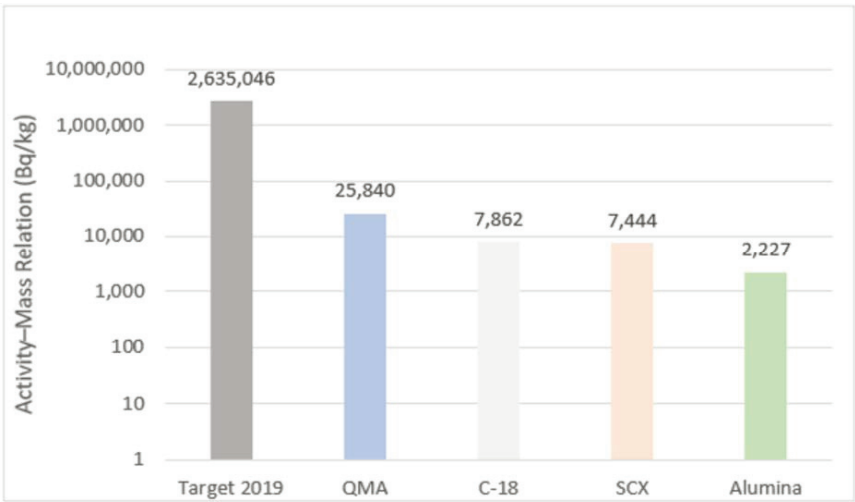

Table 4: Activity of Environmental Impact Indicators (Bq/kg).

Conclusions

The radiological characterization performed at the INCART production center has allowed us to establish a detailed profile of the secondary activated elements, validating the effectiveness of gamma spectrometry as an operational monitoring tool. The most relevant findings of this research are detailed below:

1. It was confirmed that the critical component in terms of long-term waste management is the niobium target. The spectral analysis identified the presence of Molybdenum-93 (^{93}Mo), a long-lived radionuclide, on the surface of the target housing.
2. In contrast to what was observed in the target, the components of the synthesis module (QMA, C-18, and Alumina filters) and the ^{18}F freshly generated in the cyclotron showed a radiological behavior dominated mainly by the residual activity of ^{18}F and traces of short-lived impurities.
3. The absence of detectable radiological activity in the water of the closed-loop cooling system constitutes a key indicator of the mechanical integrity of the system. This result rules out the presence of cracks or corrosion in the target cavity that could allow the migration of radioactive material into auxiliary systems, ensuring that there is no risk of cross-contamination to uncontrolled areas.

The future incorporation of High-Purity Germanium (HPGe) detectors is recommended to improve the spectral resolution of closely spaced lines.

Acknowledgements

Special thanks to Msc. Frank Montero Díaz for his scientific advice and guidance throughout this project. We also extend our recognition to Ing. Ramón Alonso and the Instituto Nacional del Cancer Rosa Emilia Sánchez Pérez de Tavares (INCART) for providing access to the facilities and for the valuable technical collaboration of their multidisciplinary team.

References

1. E.Q. Barbosa, D.M. Bonotto, C.R. Duarte, L.H. Mancini, Appl. Radiat. Isot. 221, 111822 (2025).
2. I.H. González, Radiopharmaceutical Applications: Current Status and Future Perspectives, Int. School of Research and Applied Nuclear Methods Conf., Varadero, Cuba (2024).
3. A. Zhemchugov, Radiation Detectors and Medical Imaging, Int. School of Research and Applied Nuclear Methods Conf., Varadero, Cuba (2024).
4. R. Lange, N. Schreuder, H. Hendrikse, in Practical Pharmaceutics: An International Guideline for the Preparation, Care and Use of Medicinal Products, Springer Nature, 531 (2023).
5. Comunicaciones INCART. (2020). Centro Ciclotrón-Radiofarmacia del Instituto Nacional del Cáncer.
6. P.S. Gil, Application of SiPMs in NaI(Tl) Scintillation Detectors: Challenges and Opportunities (2019).
7. Instrumentation and Equipment in Nuclear Medicine and Radiotherapy (2016).
8. U.F.O. Themes, Radiation Interactions with Tissue, Radiology Key (2016).

9. Radioactive Waste Classification, Int. At. Energy Agency (IAEA), Vienna (2015).
10. Gamma Spectrometry in Experimental Physics Teaching, Rev. Inv. Fis. 17 (2014).
11. IAEA. (2012). Cyclotron Produced Radionuclides: Guidance on Facility Design and Production of [18F] Fluorodeoxyglucose (FDG). Radioisotopes and Radiopharmaceuticals Series No. 3.
12. The Interaction of Radiation with Matter, Springer (2011).
13. L. Aragón, N. Borda, J. Meza, Gamma Spectroscopy, Instituto Balseiro (2010).
14. I.M.M. López, Bachelor Thesis in Physics and Mathematics, Instituto Politécnico Nacional (2010).
15. Spectroscopy with a NaI(Tl) Detector (2010).
16. Radionuclide Identification (Water, Food, Soils, Minerals), Geological Survey of Colombia (n.d.).
17. J.C.P. Acosta, L.A.P. Durán, Specialization in Radiochemistry and Nuclear Applications (n.d.).
18. Radiological Protection Authorization Regulation in the Dominican Republic (n.d.).

Coincidence-Summing Effects and Positronium-Annihilation-Photon Lines Appearing in CNT-Enhanced NaI(Tl)-Detector Response to ^{60}Co- and ^{137}Cs-Decays

H.V. Grushevskaya[1], A.I. Timoshchenko[2]

[1]Department of Computer Modelling, Belarussian State University, 220030 Minsk, Belarus
grushevskaj@bsu.by

[2]Department of Nuclear Physics, Belarussian State University, 220030 Minsk, Belarus
timoshchenkoAI@bsu.by

Today, high-resolution gamma-detectors for registering (true) coincidence events from positronium-annihilation photons are in great demand. Revealing of both internal-conversion mechanisms and an internal structure of the positronium-anion rays is complicated by the smallness of the internal conversion coefficients. We offer a method for detecting internal energy conversion that is based on carbon-nanotube (CNT) enhancement of the beta-decay energy deposition to an intermediate-size detector NaI(Tl) crystal. Responses of this detector-system graphene CNT-wall/NaI(Tl) crystal to gamma-rays of ^{60}Co and ^{137}Cs decays comprise the (true) coincidence-sum peaks from de-excitation. We investigate the generation mechanisms of (true) coincidence-summing effects in the decays and the creation of bound electron–positron pairs in electrical fields of atom-shell electrons. We propose that the energy of virtual gamma-photons in the electrical fields of the electrons which enter excited nuclei ^{60}Ni or ^{137m}Ba at that moment is converted into the energy of positronium anions. The resulting annihilation of bound pairs leads to secondary-emission (true) coincidence-sum lines at ~1190, 1210, and 1230 keV.

1. Introduction

Today developments are underway for improved and upgrade gamma detectors which will be capable of recording cascade-event energy deposition during rare nuclear decays. Such events occur when quantum entanglement plays a role in governing the nuclear decays. The entangled states are revealed in the radiation spectra of radioactive sources as peaks of the simultaneous emission of several photons in a true correlated state. Quantum entangled photon states arise from annihilation of positronium Ps [1]. The smallness of internal conversion coefficients prevents the internal-energy-conversion detection by using gamma-spectroscopy methods. Reliable registration of such events is also challenging because of the summation over the photons randomly scattered in the detector that leads to a significant broadening of the spectrum. Photon noise in the most sensitive superconducting photon detectors triggers avalanche events at energy scales of several eV, which provide their ultimate sensitivity limit does not allow for recording fine coherent events occurring in nuclei [2]. Thus, it is necessary to design gamma detectors on principles different from silicon electronics, for example, to develop graphene electronics. In [3], it has been proposed to use crystalline bilayers of carbon nanotubes (CNTs) for enhancing the response of the scintillation

detector NaI(Tl) crystal. Electrons have probability of entering the nuclei; virtual gamma quanta generate electron–positron pairs in electric fields of electrons which have penetrated into the nuclear space. The phenomenon of internal energy conversion happens in excited nuclei, for example, ^{60}Ni and ^{137m}Ba that are products of the beta decay of radioactive ^{60}Co and ^{137}Cs, respectively.

A goal of this paper is to discover mechanisms of (true) coincidence-summing effects by studying CNT-enhanced scintillation-crystal responses to deposition of gamma-rays energy from ^{60}Co and ^{137}Cs beta decays. The effects are brought out by internal conversion of the energy of virtual gamma quanta into the energy of electron–positron pair generated in an electrical field of electrons which at that moment are entering the nuclei of ^{60}Ni or ^{137m}Ba.

2. Materials and Methods

Activities, A, of radioactive decay of ^{60}Co and ^{137}Cs (CsI) ionized-radiation sources (IRSs) were of 28.1 and 62.2 kBq, respectively, at the moment of irradiation. The low-intensive beta-particles beams have been attenuated by a thin-film aluminium shield.

Walls of carbon nanotubes were used as rolled-up graphene sheets in our designed detector system. The raw few-walled CNTs purchased from Fibermax (Greece) are covalently modified by carboxyl groups and non-covalently functionalized by stearic acid molecules. The radiation responses of scintillation detector crystal and such a detector system as CNT-bilayer/scintillation-crystal with intermediate crystal dimensions were studied. The scintillation crystal thallium-activated sodium iodide, NaI(Tl) (a diameter of 25 mm, a height of 40 mm) was utilized as a detector crystal. The relative error of the 1-hour and 5-min measurements, δ_k, for ^{60}Co- and ^{137}Cs- decays, respectively, was assessed as the error for the Poisson temporal distribution with variance D_k [4]:

$$\delta_k = 1/\sqrt{D_k} = 1/\sqrt{A\,t_m} \tag{1}$$

and amounted to 0.99×10^{-4} (0.0099%) and 2.3×10^{-4} (0.023%), respectively. Here t_m is a measurement time.

The analysis of secondary electrons spectra has been performed by a lab-quality radiation spectrometric facilities “Nuclear Physics” (BSU, Minsk, Belarus). Channel number is proportional to the impulse height.

3. Model of Internal Energy Conversion

Quantum configurations of two bound electron (denoted by e'^{-} and e^{-}) – positron (denoted by e^{+} and e'^{+}) pairs, $e^{+}-e'^{-}$ and $e'^{+}-e^{-}$, which are generated by two virtual photons in an electrical field of atom-shell electron $e^{-}_{K-shell}$, are entangled in our model of internal conversion of excited-nucleus energy. This model is shown in Figs. 1a and 1b. The three-body system, denoted by $e^{+}_{\uparrow,E_0}-e^{-}_{\uparrow(\downarrow),E_1}-e^{-}_{K-shell,\uparrow,E_0}$, composed of the two electrons being linked to the positron is named as negative positronium ion P^{-}_{S}. Its energy-level diagram can be constructed by analogy with the Pauli principle. The ground P^{-}_{S} state is shown in Fig. 1c,

from the left. Since there is only the one electron–positron pair, $e^{+}_{\uparrow,E_0} - e^{-}_{\downarrow,E_1}$, which possesses zero spin and the energy being equal to $E_{p_1} = E_0 - E_1$, the ground state is forbidden by the law of angle-momentum conservation. The high-energy photons γ_1 and γ_2 can excite transitions of both the P^{-}_{S} positron and the P^{-}_{S} electron from the states with energy E_0 and spin "up" into the states with energy E_2 and spin "up" due to the Pauli principle (see Fig. 1c, from the right). It turns out that there exists a way to transit into a low-lying excited entangled P^{-}_{S} state satisfying the angle-momentum-conservation law. We consider this de-excitation process in the next section.

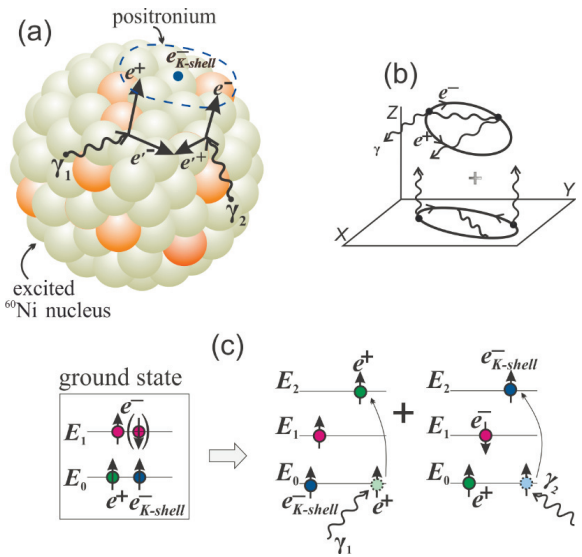

Fig. 1. Internal conversion of virtual-photon energy into electron–positron-pair energy (a) and model of quantum entanglement of states of two annihilating bound electron-positron pairs (b); (c) the diagrams of energy levels for ground (left) and excited (right) states of P^{-}_{S}.

4. True Summing Events from Positronium-Anion Annihilation-Photon

After transition of the positron $e^{+}_{\uparrow,E_0}$ into the unoccupied high-energy level E_2 the Pauli principle permits simultaneous transitions of the positron $e^{+}_{\uparrow,E_2}$ and the electron $e^{-}_{\uparrow,E_1}$ into the energy levels E_1 and E_0, respectively, after emission of two photon γ'' and γ'. The de-excitation process is shown in Fig. 2a. Both the bound electron–positron pairs, denoted by $e^{+}_{\downarrow,E_1} - e^{-}_{K-shell,\uparrow,E_0}$ and $e^{+}_{\uparrow,E_0} - e^{-}_{\downarrow,E_1}$, being constituents of the de-excited P^{-}_{S} state possess zero

spin and, correspondingly, the high- and low-energy excited P_S^- entangled states satisfy the angular-momentum-conservation law. It means that positronium-annihilation-photon lines should appear in gamma-radiation spectra and the sum of energies, E_{p_1} and $E_{p_2} = E_1 - E_0$, of the electron–positron pairs in the low- and high-energy P_S^- states, respectively, is equal to zero. Correspondingly, the scintillation crystal records the three spectral bands with maxima at the γ'-photon energy $E_{\gamma'}$, at the γ''-photon energy $E_{\gamma''}$, and at the conversion-electron energy $E_2 - E_0$ and the one (true) coincidence sum peak at energy of $E_{sum} = E_{\gamma'} + E_{\gamma''} + (E_2 - E_0) = 2(E_2 - E_0)$ as the events of the cascade occur coherently because of the annihilation-photons entanglement.

Hole and electron currents of bipolar graphene neutralize the positronium ions and, correspondingly, the beam is affected by environment to a lesser extent. As a result, the radiation-line intensities should grow. Fig. 2b shows the neutralizing action of graphene currents on P_S^-.

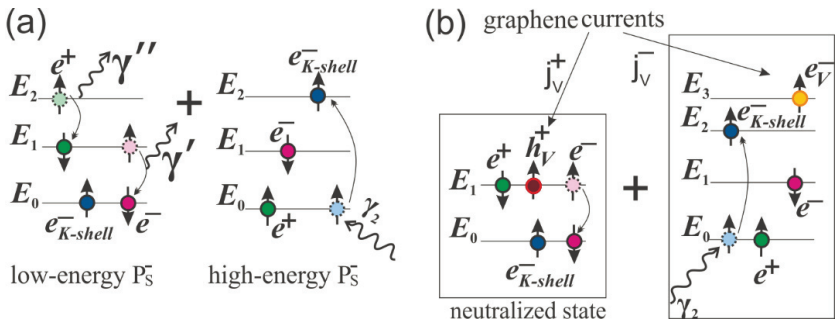

Fig. 2. De-excitation (a) and graphene-current neutralization (b) of P_S^- states.

The pulse-count rate in channel for the ^{60}Co-IRS and the three CNT-bilayer-sample/^{60}Co-IRS systems was measured during different times. The response functions are shown in Fig. 3a. The relation between the full widths $FWHM_{CNT}$ and FWHM at half maximum of 1173.21-keV-peak in the NaI(Tl)/CNT- and NaI(Tl)-detector responses, respectively, is of order of ½ that indicates the enhancement of NaI(Tl)-crystal response through the interaction between graphene and incident beam.

The diagram "0" in violet color which is shown in Fig. 3a, presents properly the rate of the response of the scintillation crystal on the ^{60}Co gamma-radiation in the following irradiation regime: the number of events was counted over 46 minutes. The radiation spectra of the three CNT-bilayer/^{60}Co systems were recorded by the NaI(Tl) detector crystal in the following irradiation regimes: 1) simultaneous 30-min exposure of the first sample and 30-min recording of NaI(Tl)/first-sample response (light-blue plot "1"), 2) simultaneous 61-min exposure of the second sample and 61-min recording of NaI(Tl)/second-sample

response (green plot "2"), 3) simultaneous 86-min exposure of the third sample and 86-min recording of NaI(Tl)/third-sample response (red plot "3"), 4) simultaneous additional 34-min exposure of the third sample (total 2-hour irradiation) and 34-min recording of NaI(Tl) /third-sample response (dark-blue plot "4").

Comparison between the response functions reveals that against the background of narrowed peaks of the CNT/NaI(Tl) detector-system response, the true coincidence-sum peaks appear; the true coincidence summing of events is hidden in the broad 1.172-MeV full-energy peak (photopeak) of the NaI(Tl)-detector response. Thus, in Fig. 3a, the 1.172-MeV photopeak for the ^{60}Co decay in the NaI(Tl)-crystal responses narrows in width and its intensity increases relative to the detector system. Due to both the narrowing and the enhancement of the response, the following peaks are statistically distinguished: 1) the "1.332-MeV Single Compton Edge" of single Compton scattering of the 1.332-MeV gamma-ray and 2) the three "Coincidence Sum Peak$_i$", i=1,2,3 peaks from the true summing of simultaneous events with quantum entangled states.

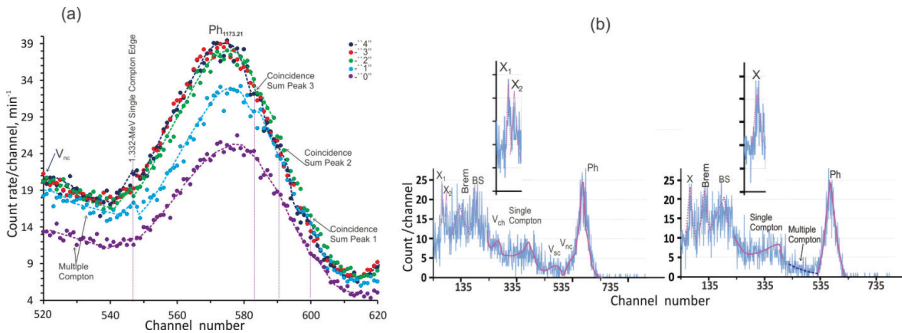

Fig. 3. Response functions (a) for the ^{60}Co beta-decay in the region of the 1.173-MeV photopeak: "0" and "i", i = 1,…4 denote the usual and CNT-enhanced responses of the NaI(Tl) detector crystal at various irradiation times; and (b) for the ^{137}Cs beta-decay.

The true coincidence summing "Coincidence Sum Peak$_1$" of pulses from two 612.31-keV bound-positron-annihilation photons is observed by both the detector crystal and the CNT/NaI(Tl) detection system. The peaks at the channel no. 299 and the channel with doubled number 598–600 are evidence of the P_S^--states quantum entanglement. The "Coincidence Sum Peak$_2$" recorded by the CNT/NaI(Tl) detector brings out the true coincidence summing of pulses from the gamma-rays which appear with $E_3 - E_0 = 693.91$ keV and $E_1 - E_0 = 516.43$ keV after the interactions of P_S^- with graphene vortical electron-density defects in the CNT/NaI(Tl) detector, the "Coincidence Sum Peak$_3$" brings out the true coincidence summing of pulses from the gamma-rays which appear with $E_2 - E_0 = 675$ keV and $E_1 - E_0 = 516.43$ keV in the CNT/NaI(Tl)-detector responses also after the interactions of P_S^- with graphene. Let us choose $E_0 = 0$. Then, after summing the energies, $E_1 - E_0$ and $E_3 - E_0$, of the annihilation peaks and the energy E_{X-ray} of the X-ray

γ''-radiation peak and then subtracting the gap energy E_g of P_S from the obtained total one can get a value which should be equal to the energy, $E_{1332keV-\gamma}$, of the 1.33243-MeV photon from the ^{60}Co beta decay:

$$E_{1332keV-\gamma} = E_1 + E_3 + E_{X-ray} - E_g \tag{2}$$

and, thus, the experimental data give evidence that $E_g = 3.89$ keV.

Let us show that, similarly as for the ^{60}Co beta-decay, the interaction with graphene enhances intensity of the gamma-photon beam from ^{137}Cs beta decay. Making comparison between response functions recorded by the scintillation-crystal and CNT/NaI(Tl) detectors one can see that the resolution of the detector system increases due to narrowing of both the photopeak "*Ph*" and the characteristic- "X"-ray and backscattering "*BS*" peaks. The responses to γ-rays from ^{137}Cs beta decay are shown in Fig. 3b. In the radiation spectrum recorded by the CNT/NaI(Tl) detection system, there are two narrow X-ray-escape peaks, X_1 with a maximum at the 68th channel (at the energy of 85 keV) and X_2 with a maximum at the 74th channel (at the energy $E_{sum,conv}^{CNT-exper}$ of 92.2 keV), instead of the single broad X-ray-escape peak "X" with a maximum at the 68th channel of scintillation crystal detector.

K-, *L*-, and *M*-line conversion-electron energies ($E_{e_i,con}, i = 1,2,3$) for ^{137m}Ba are of 624.2, 655.7, and 660.4 keV, respectively. Correspondingly, since the ^{137}Cs-decay gamma-ray energy measured to date is of $E_{\gamma_v} = 661.657$-keV the *K*-, *L*-shell, and *M*-shell- electrons binding energies ($E_i^{theor} \equiv E_{\gamma_v} - E_{e_i,con}$) should be of 37.457, 5.957, and 1.257 keV, respectively. Now, we can theoretically assess an energy, $E_{sum,conv}^{theor}$, deposited by the X-ray-summing event originated from the internal conversion of virtual E_{γ_v} photons at the ^{137m}Ba de-excitation as

$$E_{sum,conv}^{theor} = 2\sum_{i=1}^{3} E_i^{theor} = 89.34\,\text{keV}. \tag{3}$$

Here the factor of 2 takes into account the spin value of $\pm$**½.** Then, one can theoretically predicts an energy E_t^{theor} per one X ray of the order of

$$E_t^{theor} = E_{sum,conv}^{theor} / 3 = 29.74\,\text{keV}. \tag{4}$$

The prediction (4) is different from an experimental value of 29.45-keV for the characteristic X ray which was along with 630-keV conversion electrons recorded by [5] in the (true) coincidence-summing event from the ^{137}Cs decay.

To the binding energy $E_{sum,conv}$ of electrons in the atom shell, the binding energy E_g of positronium is added when the internal conversion of virtual-photon energy into the P_S^- energy occurs in the ^{137m}Ba nucleus. It means that the atom missing an inner electron can

relax by a cascade of X -ray emissions and, correspondingly, the true-coincidence summing event deposits the energy (in keV) of

$$E_{sum,conv} = E_{sum,conv}^{CNT-exper} - E_g = 88.31. \quad (5)$$

As a result, the energy, E_t, per one characteristic X -ray equal to

$$E_t = \frac{1}{3} E_{sum,conv} = 29.44\,\text{keV}. \quad (6)$$

It is very close to the experimental value recorded by [5].

Thus, in the phenomenon of internal conversion of gamma-quantum energy into the energy of a positronium ion, the annihilation photons are generated in an entangled quantum state.

5. Conclusion

So, based on using the CNT enhancement of the detector-crystal response, the mechanisms of the internal energy conversion in ^{60}Ni and ^{137m}Ba nuclei have been offered. It is shown that the bound electron–positron pairs are generated in quantum entangled states. The resulting annihilation of these bound pairs leads to appearing secondary-emission (true) coincidence-sum lines in CNT-enhanced NaI(Tl)-detector response at ~ 1190, 1210, and 1230 keV for ^{60}Co beta-decay and at 92.2 keV for ^{137}Cs beta-decay.

Funding

This work has been supported in part by Research grant No.3.18 within the Basic Research Program “Development of nuclear power engineering, nuclear and radiation technologies”, the Republic of Belarus.

REFERENCES

1. Shi Y. Chien-Shiung Wu as the experimental pioneer in quantum entanglement // Modern Phys. Lett. A. – 2025. – V. 40. – P. 2530001.
2. Chang C.L. *et al.* [TESSERACT Collaboration] Spontaneous generation of athermal phonon bursts within bulk silicon causing excess noise, low energy background events and quasiparticle poisoning in superconducting sensors // Appl. Phys. Lett. – 2025. – V. 127. – P. 263502.
3. Grushevskaya H.V., Timoshchenko A.I. Impact of graphene currents on positronium anion beam produced through internal photon-energy conversion in ^{60}Co and ^{137}Cs decays // Int. J. Nonlin. Phen. in Compl. Sys. – 2025. – V. 278. – P. 397.
4. Avdanina E.A., et al. // *Handbook of Nuclear Physics* / Ed. By V. G. Baryshevsky. – Belarussian State University Publishing, 1983.
5. Ukaegbu I., Gamage K. A model for remote depth estimation of buried radioactive wastes using CdZnTe detector // Sensors. – 2018. – V. 18. – P. 1612.

Predictions of asymptotic correlation function of scattered neutrons oscillations based on algebraic theory of spontaneous symmetry breaking

Gudkov E. L.
Dubna State University

This paper presents an algebraic formalism for spontaneous symmetry breaking based on C*- algebras, ideals, and factor norms. The main theorem, a combination of results by Roos and Sturmer, provides a quantitative criterion for symmetry breaking: the positivity of the factor norm $\|a\|_I$. It is shown that this condition leads to persistent correlations and oscillatory behavior of the correlation function at large distances. This explains anomalies in neutron scattering spectra and temperature dependences observed in thin ferromagnetic films and other systems. Modifications of the dynamic structure factor are obtained, including non-Lorentzian peaks, power-law tails, and periodic contributions from Poincaré recurrences.

1 Introduction

At the beginning of the 1960s, an algebraic (axiomatic) interpretation of quantum field theory was developed. One of the leading scientific groups was the Bogoliubov school, which initiated the "method of large translations"[1, 2] for describing phase transitions — a project that has remained unfinished until now. In this work, we present a new realization of this method based on a combination of theorems on spontaneous symmetry breaking.

The main consequence of the general theorem is a new behavior of correlation functions at large distances: they are shown to oscillate periodically with an approximately constant period. In the literature on neutron scattering, there are many examples of unusual tendencies in energy spectra and energy fluctuations. While oscillations of correlation functions have not yet been directly observed, there is initial evidence for their existence in the RESEDA detector. More compelling evidence comes from the deviation of the spectral function from the standard Lorentzian spectrum. In the work of Groitl et al., another type of distribution was described, differing from the Lorentzian peak by an exponential periodic factor. Our theory provides a deep theoretical justification for the non-Lorentzian peak and is completely consistent numerically.

There is also a large body of anomalies in temperature characteristics, particularly interesting in the case of $WCrO_2$, where a slow decrease in temperature fluctuations was detected, each depending on the value of the order parameter. In addition, anomalies in

scaling factors are predicted. All these phenomena, according to our model, are caused by Poincaré recurrences, as in the trivial spin chain model with "time peak revivals." The anomalies in the temperature behavior of correlation functions are called "Boni-Shirane anomalies[6]." In this paper, we propose a new way to describe such anomalies in temperature behavior and phase transitions.

This is an algebraic theory of spontaneous symmetry breaking, based on the mathematical foundations of operator algebras. The main achievement of the theory is the unification of numerical criteria for spontaneous symmetry breaking. The article includes both mathematical and physical aspects, starting with the mathematical foundations.

2 General theorem of spontaneous symmetry breaking in algebraic interpretation

The general theorem of this work is a combination of two classical results: the Roos theorem [3] on double-sided ideals and the Kaplansky-Stormertheorem [11] on asymptotically abelian sequences of Banach operators.

Let us formulate the general theorem:

there exists a C*-algebra with unit element, $I \subset A$ – closed double-sided ideal, $\pi : A \to B(H)$ – irreducible representation, $\omega \in H$ – cyclic vector with unit norm $\|\omega\| = 1$, α-invariant state, $\{g_n\} \subset G$ – sequence tending to infinity for Banach operators. Consider the state $\omega, \phi(a)$ is satisfied such equalities:

(i) Estimate of the difference of matrix elements:

$$\left|\langle\omega, \pi(a)\omega\rangle - \langle\omega, \pi(\alpha(a))\omega\rangle\right| \leq \|a\|_q.$$

(ii) If $I = \mathcal{K}(H)$ is an ideal of compact operators, then there exists a sequence $\{g_n\}$ for which the limit equality is attained:

$$\lim_{n\to\infty} \|\pi(\alpha_{g_n}(a)) - \langle\omega, \pi(\alpha_{g_n}(a))\omega\rangle I_H\| = 2\|a\|_q,$$

where convergence is understood in the weak operator topology.

(iii) The operator $T(a) = \text{w-lim}_{n\to\infty} (\pi(\alpha_{g_n}(a)) - \langle\omega, \pi(\alpha_{g_n}(a))\omega\rangle I_H)$ is weakly closed.

This theorem is a combination of Roos theorem and asymptotical Størmer theorem. This theorem defines a fixed value of the norm between the closed two-sided ideal and observable a in phase space. The system is in a general state without ω. Mathematically, this state is an irreducible representation.

The state ω is invariant with respect to the symmetry α. So, on average, the symmetry of the ground state is not broken.

Nevertheless, the representation $\pi \cdot \alpha$ could be not equivalent to $\pi(\omega)$. This is the condition of spontaneous symmetry breaking.

3 Proof of the general theorem

Described state $\varphi(a) = \langle \omega, \pi(a)\omega \rangle$. By the condition there is $\varphi(\alpha(a)) = \varphi(a)$. Describe the differences:

$$\Delta(a) = \varphi(a) - \varphi(\alpha(a)).$$

Note that $\Delta(x) = 0$ for every $x \in I$, because φ is a state and α is an automorphism. Therefore, Δ factors through A/I:

$$\Delta(a) = \tilde{\Delta}([a]),$$

where $[a] \in A/I$ is the class of element a.

Since $\|\tilde{\Delta}\| \leq 1$ (the difference between the two states), we obtain:

$$|\Delta(a)| = |\tilde{\Delta}([a])| \leq \|[a]\| = \|a\|_q.$$

3.1 Proof for part (ii)

Let $I = \mathcal{K}(H)$. Consider the sequence of operators:

$$T_n(a) = \pi(\alpha_{g_n}(a)) - \langle \omega, \pi(\alpha_{g_n}(a))\omega \rangle I_H.$$

By irreducibility of π and asymptotical abelianness $\{\alpha_{g_n}\}$ (in the sense of Størmer):

$$\lim_{n\to\infty} \|T_n(a)\| = 2 \cdot \mathrm{dist}(\pi(a), \mathbb{C}I + \mathcal{K}(H)).$$

But $\mathrm{dist}(\pi(a), \mathbb{C}I + \mathcal{K}(H)) = \|a\|_q$, which completes the proof of the limit equality. So from this we have the conclusion: when the factor norm is positive defined, i.e. $\|a\|_q > 0$, the symmetry is spontaneously broken.

3.2 Proof of part (iii)

Now the argument of the operator sequence tends asymptotically to zero. By the Banach-Alaoglu theorem and the Haagerup theorem, we have:

$$\lim_{n\to\infty} \|T_n(a)\| = 2 \cdot \mathrm{dist}(\pi(a), \mathbb{C}I + \mathcal{K}(H)).$$

The weak closedness follows from the uniform boundedness and the fact that the limit is unique.

3.3 Consequence 1

If the norm on the factor space of any element in C^* algebra:

$$\|a_q\| > 0$$

for some $a \in A$, the symmetry is spontaneously broken.

4 Theorem of correlators: generalization of Bogoliubov inequality

Exploring the connection between the double-sided ideal and the norm of the order parameter in phase factor space on the behavior of the correlation function for some two elements of A, we formulate the theorem of correlators:

For $a, b \in A$ and an ideal $I = \{x : \omega(x) = 0\}$:

$$\|ab\|_I \leq \sqrt{\omega(a^*a)\,\omega(b^*b)}.$$

Using the Cauchy-Bunyakovsky inequality:

$$|\omega(a^*b)|^2 \leq \omega(a^*a)\,\omega(b^*b).$$

Consider the element $x = ab - \omega(ab) \cdot 1_A \in I$. Then:

$$\|ab - x\| = |\omega(ab)| \leq \sqrt{\omega(a^*a)\,\omega(b^*b)}.$$

Therefore:

$$\|ab\|_I \leq \sqrt{\omega(a^*a)\,\omega(b^*b)}.$$

In the case $a = b$ and $\omega(a) = 0$:

$$\|a^2\|_I \leq \omega(a^*a).$$

Equality is achieved when a and b are "maximally uncorrelated" in the state ω.

When we have a state with observables set in the ideal, the distance from an observable in a general state and the value of this observable as an ordering parameter in phase space gives the numerical criterion of spontaneous symmetry breaking:

$$\|a\|_q = \inf_{y \in \inf} \|a - x\|_q > 0,$$

where $\|a - x\|_q$ is the distance from observable x to the closed subspace, which is called $\|a\|_q$.

In the standard theory of Bogoliubov inequality, In the standard theory of the Bogoliubov inequality,

$$|\omega(a^*b)|^2 \leq \omega(a^*a)\,\omega(b^*b)$$

[2], but it can be extended to the factor space...[2], which leads to the generalization to the factor space on C^*-algebras:

$$\|[a][b]\|_{A/I} \leq \sqrt{\omega([a]^*[b]^*)\,\omega([b]^*[b])}.$$

$\omega([a]^*[a]) = \omega(a^*a)$, which in the ideal is equal to zero for $\|a\|_q > 0$. From Roos theorem, the condition of invariance of the double-sided ideal is equivalent to a non-zero factor norm.

$$I \subset I(\alpha) = I(\omega) : \{x : \omega(x) = 0\} \subset I(\omega(a)) \subset I(\omega(a)) \tag{1}$$

Here

$$I_0 = \{a \in A \mid \omega(a^* a) = 0\} = \{a \in A \mid \pi_\omega(a)\Omega = 0\}. \tag{2}$$

Thus, the ideal consists of operators that annihilate the vacuum vector Every such vector operator could not generate states (also on action to vacuum gets spontaneous symmetry broken state). Physical states save the vector by definition of the kernel of representation.

$$I = \{a \in A \mid \pi_\omega(a) = 0\} \tag{3}$$

is a closed double-sided ideal, so describe the condition of physical observables $\omega(a)_I = 0$:

$$\|ab\|_I = 0. \tag{4}$$

Thus, every non-pure state did not appear by correlators; it is unobservable and localized in the marked product:

$$\|ab\|_I > 0. \tag{5}$$

As a result, Bogoliubov's theorem is generalized to the case where the space of observables is extended to factor algebras by an ideal, and the possibility that the product may remain in the ideal (be "non-physical") is observed. This is especially important for gauge theories and theories with spontaneous symmetry breaking, where ideals play a key role.

To prove the criteria of construction for ideal:

$$I = \{\overline{a \in A \mid \pi_\Omega(a) = 0}\} \tag{6}$$

In standard quantum theory, the products in linear space of operators are localized. Two cases of ideals may be introduced. In Bogoliubov's works, the phase subspace values in observables are put in average; in the class of observables in the factor-class at C^*-algebra, the commutant of such observable is equal to zero:

1. If observables are set in a subspace on the ideal (there is no spontaneous symmetry breaking), operators $\|ab\|_I$ commute with $\{I : \omega(x) : \pi(a)\}$.
2. When the observable does not set in the ideal $\{I : \omega(\pi(a)) \to \pi(\omega \circ \beta[a])\}$, the products of correlated functions are compared to a general pure state.

Correlator inequality could be described as consequence of Mazur inequality

5 Application of the theorem of correlators for neutron correlation function

The most explicit way to verify this effect by experimental data is neutron scattering, because the angle distribution depends only on the order parameter. These correlation inequalities would be used to analyze oscillation effects.

$$C(r,t) = \int \frac{d^3q}{(2\pi)^3} \int \frac{d\omega}{2\pi} e^{iqr-\omega t} S(\mathbf{q},\omega) \tag{7}$$

Now substitution to the correlation function from the correlators inequality, the cluster property gives limits for each $\pi(a)$ to the correlation function:

$$\lim_{g_n\to\infty} \|[a][b]\|_{I/2} = \|ab\|_\omega(a^*a)\omega(bb^*) = \lim_{g_n\to\infty} = |\omega(\alpha_g(b)) - \omega(b(a)\omega)| \to \infty \tag{8}$$

Thus, the correlation function caused a modification of the spectral function which approximated Fourier imaginary by the Oswald-Cernicke formula with an additional exponent term. From the factor norm: $\|S^z\|_q = M_0(1 - T/T_c)$.

$$S(\vec{q},\omega) = (2\pi)^3\delta(\vec{q})\delta(\omega)\cdot\|M\|_q^2 + \frac{\chi_0\Gamma_q}{\omega^2+\Gamma_q^2}\cdot\frac{1}{1+(q\xi)^2}$$

$$S(\vec{q},\omega) = \frac{\chi_0\Gamma_q}{\omega^2+\Gamma_q^2}\cdot\frac{1}{1+(q\xi)^2}\cdot F(\omega), \quad F(\omega) = [1+\alpha_R e^{-\beta_R\omega^2}]$$

Periodically time-revivals caused factor:

$$F_R(\omega,T) = 1 + \sum_{k=1}^{N} A_k(T)\,\frac{\gamma_k}{(\omega-\omega_k)^2+\gamma_k^2} + G(\omega,T)$$

$$G(\omega,T) = A_0(T)\exp\left(-\frac{\omega^2}{\sigma(T)^2}\right)$$

In an alternative way, the existence of periodical factors could be understood for two conditions: non-zero oscillation and the saving of the full spin of level as a superposition. So we have the constant spin condensate density for unitary non-residual representation of pure state to the factor space. We have such limits of cluster state which include a discrete unitary subgroup at factor space when the spectral function is maximized on spin continuum; this exponentially fluctuates.

Describes the Oswald-Cernicke spectrum function for frequency distribution:

$$\rho(\omega) = \frac{1}{2\pi}\int dt\, C(t) \tag{9}$$

$$C(t) = \langle a(t)a(0)\rangle \tag{10}$$

Fourier transform of the time-dependent correlator function:

$$C(t) = \int_{-\infty}^{\infty} e^{-i\omega t}\rho(\omega)d\omega \tag{11}$$

$$C(t) = Ze^{-i\Omega_0 t-\Gamma|t|+C_{\text{const}}(t)} \tag{12}$$

$$C(t) = Ze^{-i\Omega_0 t-\Gamma|t|} + C_{\text{const}}(q,t) \tag{13}$$

$$\rho(\omega) = \frac{1}{2\pi}\int_{-\infty}^{\infty} dt\, e^{i\omega t}C(t) \tag{14}$$

$$\rho_{\text{osc}}(\omega) = \frac{Z}{\pi}\frac{Z}{(\omega-\Omega)^2+\Gamma^2} \tag{15}$$

Hence:

$$S(q) = \frac{Z(q)}{\pi}\frac{\Gamma(q)}{(\omega-\Omega(q))^2+\Gamma(q)^2} + [1+\alpha_R e^{-\Omega t-\Gamma(q)t}] \tag{16}$$

Linear broadening is increased in spectral function:

$$S(q,\omega) = \frac{Z(q)}{\pi}\frac{\Gamma(q)}{\omega-\Omega(q)-\delta(q)^2+\Gamma(q)^2}\left(1+\lambda(q)\frac{\omega-\Omega(q)}{\Gamma(q)}\right) + S_{\text{continuum}}(q,\omega) \tag{17}$$

where

$$S_{\text{continuum}} = \text{Im}\,\frac{\chi_0(\tau,\omega)}{(\omega-\Omega(q)\Gamma(q))^2} = \frac{1}{1-e^{\beta\mu}}\int e^{\Omega t\cos\omega} = \frac{1}{\pi}\frac{1}{\pi}\frac{1}{\omega/\Gamma-\alpha(\omega\Gamma)}$$

$$S(q,\omega) = \frac{Z(q)}{\pi}\frac{\Gamma(q)}{\omega-\Omega(q)-\delta(q)^2+\Gamma(q)^2}\left(1+\lambda(q)\lim_{N\to p}\frac{\omega-\Omega(q)}{\Gamma(q)}\right) \to \frac{1}{1+\omega\Gamma-\alpha(\omega\Gamma)}$$

$$S_{\text{st an}}(\mathbf{q},\omega) = \frac{Z(q)}{\pi}\frac{\Gamma_q}{(\omega-\Omega_q)^2+\Gamma_q^2}\cdot\frac{1}{1-e^{-\beta\omega}} \tag{18}$$

Here: $\Omega(\vec{q}) \approx 0$ – quasielastic scattering length; $\Gamma(q) = \Gamma_q$ – width depends on transmitted momentum.

For the factor norm of the spin-order parameter, we get explicit dependence on temperature:

$$\|S\|^z = M_0\left(1-\frac{T}{T_c}\right) \tag{19}$$

$$Z(q) = 2M_0\left(1-\frac{T}{T_c}\right) \tag{20}$$

$$S = \frac{\chi_0}{\pi}\frac{\Gamma_q}{\omega^2+\Gamma_q^2}\cdot\frac{1}{1+(q\xi)^2} \tag{21}$$

$$\chi_0 \approx M_0\left(1-\frac{T}{T_c}\right) \tag{22}$$

$$G(\omega,T) = A_0(T)\exp\left(-\frac{\omega^2}{\sigma(T)^2}\right) \tag{23}$$

$$S(q,0) = \frac{\chi_0}{\pi(1+(q\xi)^2)}\frac{\Gamma_q}{\omega^2+\Gamma_q^2}[1+A_0e^{-\omega/k^2}+\sum_k A_k] \tag{24}$$

So the full asymmetric distribution factor contributes as:

$$S(\mathbf{q},\omega) = \frac{Z(q)}{\pi}\frac{\Gamma_q}{(\omega-\Omega_q)^2+\Gamma_q^2}\left(1+\lambda(q)\frac{\omega-\Omega_q}{\Gamma_q}+\mu(q)\frac{(\omega-\Omega_q)^2}{\Gamma_q^2}\right) \tag{25}$$

When the asymmetric distribution depends on eigenfrequency:

$$S(\mathbf{q},\omega) = \frac{Z(q)}{\pi}\frac{\Gamma_q}{(\omega-\Omega_q)^2+\Gamma_q^2}\left(1+\lambda(q)\frac{\omega-\Omega_q}{\Gamma_q}+\mu(q)\frac{(\omega-\Omega_q)^2}{\Gamma_q^2}\right) \tag{26}$$

In the statistical limit we get:

$$S(\mathbf{q},\omega) = \frac{Z(q)}{\pi}\frac{\Gamma_q}{\omega^2+\Gamma_q^2}\left(1+\lambda\frac{\omega}{\Gamma_q}+\mu\frac{\omega^2}{\Gamma_q^2}\right) \tag{27}$$

where the Lorentzian is approximately valid where N is a small number of particles. Describing the general width of the spectrum, we have:

$$S(q,\omega) = \frac{Z(q)}{\pi}\frac{\Gamma_q^{\text{eff}}}{(\omega-\Omega_q)^2+(\Gamma_q^{\text{eff}})^2}\cdot\frac{1}{e^{-\beta\omega}} \tag{28}$$

Thus we can produce the dependence of the exponential factor from time. We propose numerical estimates for the width of generalization with periodicity:

$$S(q,\omega) = \frac{1}{\pi}\frac{\Gamma(q)}{\omega^2+\Gamma(q)^2}\left[\frac{1}{e^{\beta\omega}}+1\right]+\sum_{n=1}^{\infty}\frac{A_n(q)}{\pi}\frac{\gamma_n(q)}{(\omega-\omega_n(q))^2+\gamma_n(q)^2}\cdot[n(\omega_n)+1] \tag{29}$$

$$C(\mathbf{r},t)\sim Ae^{-\Gamma t}\cos(\mathbf{Q}\cdot\mathbf{r}-\Omega t+\phi) \tag{30}$$

Notes, that:

$$\|S_q^+S_{-q}\|_I \le \sqrt{\omega(S_q^+S_q^-)\omega(S_q^-S_q^+)} \tag{31}$$

$$S(\mathbf{q},\omega) = \int d^3r\int_{-\infty}^{\infty}dt\; e^{-i(\mathbf{q}\cdot\mathbf{r}-\omega t)}\;C(\mathbf{r},t) \tag{32}$$

Let A be a C*-algebra, α_g an asymptotically abelian family of automorphisms (e.g. space translations), ω an α-invariant state, and $I\subset A$ a closed two-sided ideal such that $\|a\|_q>0$ for some a with $\omega(a)=0$. Consider the scaling limit:

$$T=\lim_{n\to\infty}\lambda_n\pi_\omega(\alpha_{g_n}(a_0)), \tag{33}$$

where $\{g_n\}$ is a sequence with $|g_n|\to\infty$ and λ_n are chosen so that the limit exists and is non-zero. Then the limit algebra A_∞ generated by all such limits is **commutative** and **unital** (i.e. generated by a single element T). Consequently,

$$A_\infty\cong C(\sigma(T)),$$

the algebra of continuous functions on the spectrum of T.

For the automodel (depends on time correlation function):

$$C(\mathbf{r},t)=\int\frac{d^3q}{(2\pi)^3}\int\frac{d\omega}{2\pi}e^{i(\mathbf{q}\cdot\mathbf{r}-\omega t)}S(\mathbf{q},\omega).$$

In the case of spontaneous symmetry breaking we get:

$$C(\mathbf{r},t)\sim Ae^{-\Gamma t}\cos(\mathbf{Q}\cdot\mathbf{r}-\Omega t+\phi).$$

From the correlators inequality, when the concrete example such as the Bloch operator depending on order parameter is the spin operator:

$$\|S^+_{\mathbf{q}} S^-_{-\mathbf{q}}\|_I \leq \sqrt{\omega(S^+_{\mathbf{q}} S^-_{-\mathbf{q}})\,\omega(S^-_{-\mathbf{q}} S^+_{\mathbf{q}})}.$$

From correlators inequality, non-trivial dynamics at asymptotics with constant periodicity exponential behavior:

$$S(\mathbf{q},\omega) = \int d^3r \int_{-\infty}^{\infty} dt\, e^{-i(\mathbf{q}\cdot\mathbf{r}-\omega t)} C(\mathbf{r},t).$$

6 Characters of the unital algebra

For systems with a single double-sided ideal, we can use the relevant subalgebra with a non-trivial character of non-residual representations. Let us describe this case more mathematically.

Since A_∞ is commutative and generated by T, all its non-zero representations are one-dimensional and given by **characters** $\chi_z : A_\infty \to \mathbb{C}$ defined by:

$$\chi_z(f(T)) = f(z), \qquad z \in \sigma(T).$$

The time evolution α_t (or space translations) induces an automorphism on A_∞ because the scaling limit commutes with the group action. Because A_∞ is commutative, the restriction of α_t to A_∞ must be a composition with a homeomorphism of the spectrum:

$$\alpha_t(T) = \Phi_t(T),$$

where $\Phi_t : \sigma(T) \to \sigma(T)$ is a continuous map. Moreover, $\{\alpha_t\}$ is a one-parameter group: $\alpha_{t+s} = \alpha_t \circ \alpha_s$.

For a system with a local excitation, the spectrum $\sigma(T)$ contains an isolated point z_0 corresponding to the one-particle state. On this point, the automorphism α_t acts as multiplication by a phase because the representation is one-dimensional. Hence:

$$\chi_{z_0}(\alpha_t(T)) = e^{i\phi(t)}\chi_{z_0}(T),$$

with $\phi(t)$ a continuous function. The group property forces linearity: $\phi(t) = \Omega t$ for some constant Ω (the excitation energy). Thus:

$$\chi_{z_0}(\alpha_t(T)) = e^{i\Omega t}\chi_{z_0}(T).$$

So the periodic factor is exponential.

Now substituting into the correlation function from the correlators inequality, the cluster property gives limits for each $\pi(a)$ to the correlation function:

$$\lim_{g_n\to\infty} \|[a][b]\|_{I/2} = \|ab\|_\omega(a^*a)\omega(bb^*) = \lim_{g_n\to\infty} = |\omega(\alpha_g(b)) - \omega(b(a)\omega)| \to \infty \tag{34}$$

In alternative way, the existence of periodical factors could be understood for two conditions: non-zero oscillation and the saving of the full spin of level as a superposition. So we have the constant spin condensate density for unitary non-residual representation of pure state to the factor space. We have such limits of cluster state which include a discrete unitary subgroup at factor space when the spectral function is maximized on spin continuum; this exponentially fluctuates.

Describes the Oswald-Cernicke spectrum function for frequency distribution.

7 Space translation analogy with Kapitza-Dirac effect

Another case of anomalies besides increasing spectrum width is the resonant phase transmitting for eigenvalues for non-oscillated part (perpendicular polarization) for frequency ρ_{osc}. It is a periodic equation:

$$S(q_{\parallel}, q_z) = A \cdot \frac{1}{\kappa_{\parallel}^2 + q_{\parallel}^2} \cdot F(q_z). \tag{35}$$

$(1 + e^{-\beta\epsilon}) = F(q)$-periodical potential for time peak revivals

This profile of correlation function caused for thin Fe film oscillation periodicity for transmitted momentum fluctuations:

$$\Delta q_z = \frac{2\pi}{Ld} = \frac{2\pi}{3 \times 2.86} \approx 0.73\,\text{Å}^{-1}.$$

where $L = 3$-number of layers, $d = 2.86nm$-distance between layers

Thus peaks are settled.

This correlates with the resonance effect arising from the material's periodic crystal structure — specifically, the interplay between the natural oscillation frequency and the return frequencies — which predicts a "plateau" for point-like features of the spectral function.

Thus peaks settled are: In the case of Fourier transform of the correlation function for the tangent part of the spectrum, the double-sided ideal is nilpotent. For a system with spontaneous symmetry breaking, the spectrum at the factor space is discrete.

For eigenfrequency of the system:

$$\omega_n = \omega_0 + n\Delta\omega, \qquad n \in \mathbb{Z}. \tag{36}$$

Correlation function is similar to many-magnon interactions contribution:

$$C(t) = \sum_n |c_n|^2 e^{i\omega_n t - \Gamma_n t}. \tag{37}$$

If the scaling decrement parameter is small, periodically appearing peaks:

$$t_{\text{rev}} = \frac{2\pi}{\Delta\omega}. \tag{38}$$

For three-layer film, we get:

$$\Delta q_z = \frac{2\pi}{Ld}, \qquad L = 3,\ d = 2.86\ \text{Å}. \tag{39}$$

Substitution gives the opportunity to describe:

$$\Delta q_z = \frac{2\pi}{3 \times 2.86} = 0.732\ \text{Å}^{-1}. \tag{40}$$

Thus, in peaks of recurrences in structure factors appeared for:

$$q_z^{(n)} = n\Delta q_z = n \cdot 0.732\ \text{Å}^{-1}. \tag{41}$$

$$q_z^{(1)} = 0.732 \text{ Å}^{-1}, \quad q_z^{(2)} = 1.464 \text{ Å}^{-1}, \quad q_z^{(3)} = 2.196 \text{ Å}^{-1}.$$

Another proposal for experimental detection is to analyze the intensity ratio for nearby peaks. The peak intensity is inversely proportional to the width:

$$I_n \propto \frac{1}{\Gamma(q_z^{(n)})}. \tag{42}$$

So for three-layer peaks, the ratio would be:

$$\frac{I_2}{I_1} = \frac{\Gamma_1}{\Gamma_2} = \frac{108.2}{429.6} \approx 0.252 \approx 0.25. \tag{43}$$

Note that the temperature profile of this oscillation differs from another transition symmetry breaking effect because it decreases more slowly than space non-homogeneous generated effects; each spectral function does not depend on time (for example, Kiessig oscillation).

Alternatively, the same exponential factor can be obtained using the Haar measure on the double-sided ideal associated with the maximal character of the algebra. The Haar measure selects a minimal solvable subalgebra, and its restriction to the factor space yields a Gaussian distribution of frequencies, which after Fourier transform gives exactly the same exponential contribution $e^{-\beta\omega^2}$. This approach further reinforces that the algebraic origin of the anomaly is independent of the specific kinematic details.

Hence, the combination of the kinematic peak positions (given by L and d) and the dynamical features (exponential factor, asymmetry, temperature scaling) constitutes a direct, experimentally testable prediction of the algebraic theory.

References

[1] Khoruzhiy S.S. Introduction to Algebraic Quantum Field Theory. — M.: Mir, 1986. — P. 304.

[2] Bogoliubov N.N., Logunov A.A., Todorov I.T. Foundations of Axiomatic Approach in Quantum Field Theory. — 1986. — P. 304.

[3] Roos C. Darstellung von C*-Algebren und Ideale // Math. Ann. — 1967. — Vol. 168, No. 4. — P. 270–298.

[4] Størmer E. Asymptotic Abelianness and Symmetry Breaking // Commun. Math. Phys. — 1974.

[5] Lynn J.W. Measurements of the magnetic excitations above T_c in iron and nickel. — 1985. — P. 3006.

[6] Boni P., Shirane G., Wicksted J.P., Martinez J.L. — 1984. — Vol. 29, No. 9. — P. 488.

[7] Mazur P. Non-ergodicity of phase functions in certain systems // Physica. — 1969. — Vol. 43. — P. 533.

[8] Haag R. Local Quantum Physics: Fields, Particles, Algebras. — 2nd ed. — Berlin: Springer, 1996.

[9] Bratteli O., Robinson D.W. Operator Algebras and Quantum Statistical Mechanics, Vol. 1–2. — New York: Springer-Verlag, 1979–1981.

[10] Strocchi F. Symmetry Breaking. — Berlin: Springer, 2008.

[11] Størmer E. Spectra of states, and asymptotic abelian C*-algebras // Commun. Math. Phys. — 1972. — Vol. 24. — P. 279–294.

[12] Doplicher S., Kastler D., Størmer E. Invariant states and asymptotic abelianness // J. Funct. Anal. — 1969. — Vol. 3. — P. 419–434.

[13] Bikchentaev A.M. The Peierls–Bogoliubov inequality in C*-algebras and characterization of tracial functionals // Lobachevskii J. Math. — 2011. — Vol. 32. — P. 175–1.

Search and Analysis of the Double Hit Events in the Study of (γ, f) Reactions

D.V. Kamanin[1], Yu.V. Pyatkov[1,2], V.E. Zhuchko[1], A.N. Solodov[1], T.H. Vilane[1,3], Z.I. Goryainova[1], O.V. Strekalovsky[1,3], E.A. Kuznetsova[1], A.O. Zhukova[1], Yu.M. Sereda[1], P.Z. Ngcobo[4], B.A. Le[1]

[1]*Joint Institute for Nuclear Research, 141980 Dubna, Russia*

[2]*National Nuclear Research University MEPhI, 115409 Moscow, Russia*

[3]*University of North West, 2790 Mahikeng, Republic of South Africa*

[4]*University of Zululand, 3886, Republic of South Africa*

Introduction

A large series of our experiments with $^{252}Cf_{sf}$ and $^{235}U(n_{th},f)$ sources of fission fragments (FFs) revealed a new ternary decay channel [1–3]. The channel is characterized by the nearly collinear emission of three fragments, with at least one possessing magic nucleon numbers, and is termed the Collinear Cluster Tri-partition (CCT) due to the observed features. It was established that one of the FFs from binary fission can undergo a break-up while passing through the fission source backing. The effect of breakup has been confirmed using different experimental approaches, including the double-hit method [4].

In this work, we analyze the ternary decays of ^{242}Pu accompanied by the emission of polar low-energy light charged particles (LCP) resulting from FF break-up in the target backing. This process can be considered a special case of CCT.

Experimental setup

The experiment was performed using the VEGA (Velocity-Energy Guide based Array) setup installed in the MT-25 microtron hall [5, 6] (FLNR, JINR). The layout of the spectrometer and kinematical scheme of ternary decay are shown in fig. 1.

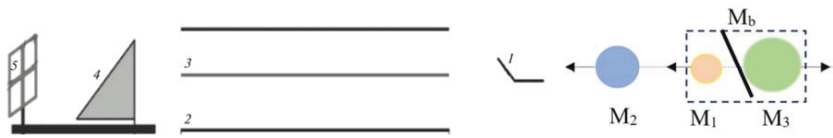

a b

Fig. 1. (a) VEGA layout: *1* – the ^{242}Pu isotope target; *2* – a guide tube of EGS; *3* – a central wire of EGS; *4* – a time-stamp detector; *5* – an array of four PIN diodes of the detector. (b) Kinematical scheme of ternary decay. The target backing is represented by a tilted line.

The target (1) of the ^{242}Pu isotope is irradiated with gamma rays of bremsstrahlung radiation from the electron beam of the MT-25 microtron. A fraction of the FF is captured by the field of the EGS (Electrostatic Guide System), consisting of a guide tube (2), 4 m long, at zero potential, and a central wire (3), to which a voltage of 10 kV is applied. At the output of the EGS, there is a detection system consisting of a time-stamp detector based on microchannel plates (4) and an array of four PIN diodes (5).

A fraction of the FFs from the (γ, f) reaction in the target is captured by the EGS field. In the presented experiment, turning on the EGS increased the counting rate of the detected FFs by 15 times compared to the situation when the EGS was switched off. A typical angle of the FFs captured in the EGS is approximately $\pm 1.5^0$. The energy E and velocity V of fission fragments, necessary to determine the mass in the frame of the (V-E) method, are measured using a time-of-flight spectrometer consisting of a timing detector and an array of four PIN diodes.

In this work, we focus on the registered events in which two "start" signals were detected by the timing detector during a 200 ns registration gate. Two FFs provided the start signals that were detected in two different PIN diodes (the registration mode "mul-2"– multiplicity two) or in the same PIN diode (the double-hit registration mode).

Below, we compare the results obtained for both registration modes.

Baseline correction algorithm

A typical signal is presented in fig. 2a and appears as a positive waveform followed by an undershoot at ~ 50 ns time interval. Because the undershoot is caused by signal reflection from the input circuit of the preamplifier, the waveform/undershoot ratio is constant and was established to be equal to 0.023.

While the presence of the undershoot does not negatively impact the area and timing calculation of the first waveform, in a double-hit signal, it may disturb the second waveform if it follows the first one by ≤50 ns. In such a case, the part of the baseline affected by the undershoot must be corrected. The correction algorithm first determines the amplitude (Ampl) of the first waveform. In the second step, a correction factor of 0.023 × Ampl was added to every point within the undershoot region, which allowed the calculation of the true area and timing for the second waveform.

To test the performance of the algorithm, we created artificial double-hit signals (fig. 2). Because the energy of the second fragment in a real experimental double-hit event is very close to that of an α-particle, the ratio between the amplitudes of the first and second waveforms is approximately 10/1. Thus, the second waveform in a test double-hit signal was synthesized from the first one, with the amplitude of 0.1 × Ampl at a time interval substantially larger than the end of the negative undershoot region (100 ns from the beginning of the first waveform).

The second waveform was then computationally shifted towards the first one by 50 ns (blue waveform in fig. 2b). The restoration algorithm was applied to restore the second waveform (red waveform in fig. 2b) true shape by correcting the baseline.

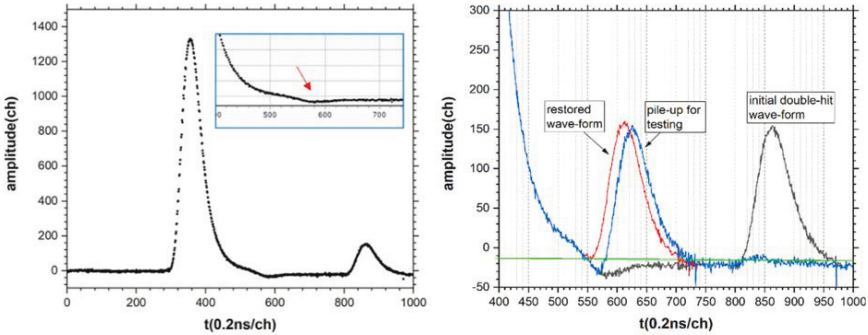

a b

Fig. 2. Validation of the baseline restoration algorithm: (a) waveform with an undershoot and a synthetic second waveform superimposed at a 100 ns distance; (b) comparison of double-hit profiles: initial reference waveform (black), uncorrected synthetic double-hit signal exhibiting baseline distortion (blue), and restored signal following undershoot compensation (red).

The baseline correction algorithm was validated by comparing the areas (S) and timing (t) of the unrestored and restored second waveforms in the double-hit (Table 1).

Table 1: Comparison of the restoration results

DT, ns	**S**	**ΔS**	**δS%**	**t, ns**	**Δt, ns**	**δt%**
*100	12017	0	0	160.4	0	0
**50	10484	1533	12.8	153.8	6.6	4.1
***50	11960	57	0.4	162	1.6	1

* Second waveform before the 50 ns shift
** The unrestored second waveform after the shift
*** The restored second waveform

Table 1 demonstrates that the algorithm produces a satisfactory level of error of the second waveform area (~0.5%) and timing (~1%) calculations, even in cases where those parameters are distorted by 13% and 4%, respectively.

Results

In the previous section, we demonstrated that the developed baseline correction algorithm produced satisfactory results when dealing with double-hit signals distorted by the negative undershoot. We applied the algorithm to the experimental data from the VEGA setup, which allowed us to save a substantial part of the double-hit signals that would otherwise have been discarded from the data processing.

Figure 1b illustrates the kinematics of the ternary decays. The arguments in favor of such a decay scenario are presented in the next section. A two-stage decay process was assumed. In the first stage, binary fission of the mother nucleus occurs, resulting in the formation of FFs with masses M2 and Mb. The first is captured by the EGS, with subsequent detection in the time-of-flight spectrometer. The FF with mass Mb undergoes breakup in the

target backing, forming two decay products with masses M1 and M3. The first one reaches the time-of-flight spectrometer, whereas the latter hits the target backing.

The spectrum of the light-charged particles (LCP) detected in registration mode mul-2 (fig. 3a) is compared with that measured in the same experiment using the double-hit experimental approach (fig. 3b). The LCP yields obtained in each mode did not exceed 2.4×10^{-3} /bin. fiss. and 1.2×10^{-3} /bin. fiss., respectively.

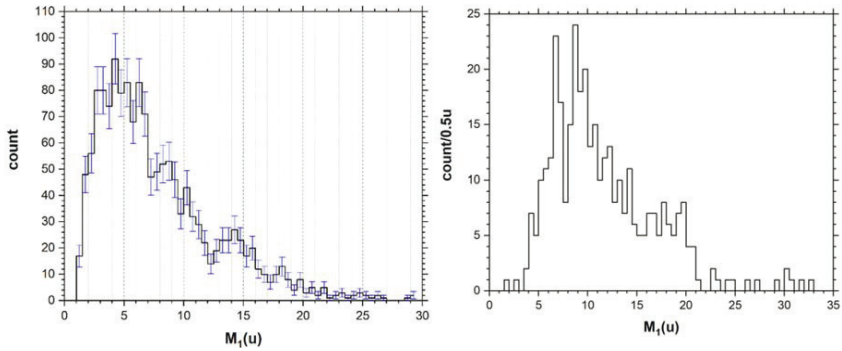

a b

Fig. 3. LCP spectra from the ^{242}Pu (γ, f) reaction measured in the frame of the mul-2 (a), and double-hit (b) registration modes.

The energy spectrum of the detected LCP is shown in fig. 4a. An example of the LCP mass-energy distribution is shown in fig. 4b.

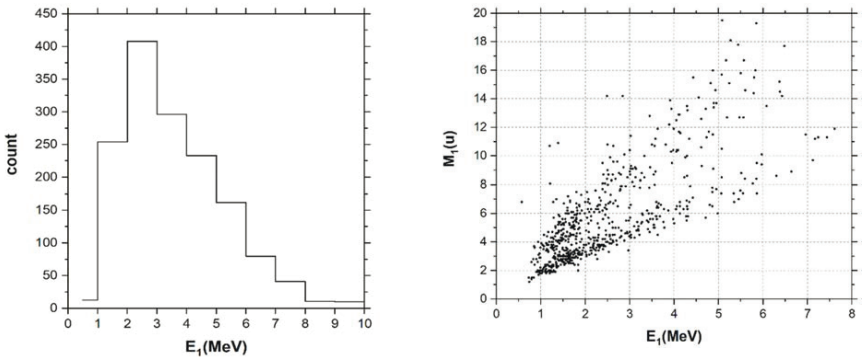

a b

Fig.4. LCP energy spectrum (a) and an example of the LCP mass-energy distribution (b) from the ^{242}Pu(γ, f) reaction. The abrupt left edge of the energy spectrum corresponds to an experimental energy threshold.

Discussion

Due to the setup geometry (fig. 1a), it can be concluded that in the ternary events under discussion, all the decay partners, including the LCP (fig. 3), fly apart almost collinearly within the accuracy of the capture angle of the FFs into the EGS ±1.50. In the well-known α-particles accompanied ternary fission, a small fraction of ternary alphas is also emitted at small angles with respect to this axis (the so-called polar α-particles) [7]. It is reasonable to compare our results with those dedicated to polar emission in ^{252}Cf(sf), in particular those obtained using the 4π charged particle detector BSiB (Berlin Silicon Ball) [8] assembled from 151 independent Si detectors arranged into a 20 cm diameter sphere. In this work, along with "conventional" polar α-particles with an energy E ≈ 25 MeV additional peak of α-particles with an energy E1 ≈ 5 MeV and a yield of ~10^{-6}/bin. fiss. was observed. Following the polar emission evaporation model [9], the velocity of the emitter should be added to the velocity vector of the evaporated particle. Therefore, particles evaporated in the direction of the velocity vector of FF have high kinetic energy, and vice versa: particles emitted in the opposite direction (backward emitted alphas) have low kinetic energy.

Thus, in our experiment, we observed the backward polar LCP similar to those detected at BSiB. Simultaneously, there are two differences between the experimental findings from the compared experiments. We observed a wide range of LCP (fig. 4) and the LCP yield ratio Y(VEGA)/Y(BSiB) ~ 103. The Coulomb interaction of the decaying fragment in the shape-isomer state with the target is presumably decisive for both differences. As was shown in ref. [10, 11], such interactions can increase the breakup probability by several orders of magnitude.

The comparison of the spectrum in fig. 4a with that shown in fig. 4b leads to the conclusion that the left edge of the latter is almost cut up to the LCP mass 6u. This peculiarity can be explained by considering the LCP mass-energy distribution in fig. 4b from one hand and the fact that the EGS was used in the experiment. It is evident that the LCP energy increases with mass, and the lightest particles have the smallest energies. The efficiency of the EGS is known to be proportional to the ratio q/E, where q is the ionic charge of the particle and E is its kinetic energy [12]. Thus, the detection efficiency of lighter LCP (or the angle at which they are caught in the EGS) is greater than that of heavier LCPs. If the mean catching angle of one of the particles from the FF pair to be detected in the double-hit registration mode exceeds the aperture of the PIN diode, which is approximately 5^0, such events will be rejected. The "truncation effect" should be considered when using the double-hit approach in studies of LCP emissions.

There is another positive interpretation of the "truncation effect." Low-energy LCP, which are rejected in the double-hit registration mode (the left edge of the spectrum in fig. 3b), are detected in two adjacent PIN diodes when the mul-2 mode is used (also the left edge of the spectrum in fig. 3a). Owing to the EGS, two initially collinear particles can be detected in adjacent detectors when they have different q/E parameters.

As mentioned above, the ratio of the LCP yields Y(mul-2)/Y(double-hit) ≈ 2 (fig. 3). A very rough estimate of this ratio can be obtained as follows: if the exposure of the PIN diodes array surface is homogeneous, there are 10 different opportunities for the detection of a pair of fragments in the adjacent PIN diodes, whereas there are only four options for double-hit detection. The obtained estimate of 2.5 is not far from the experimental value.

Conclusions

1. For the first time, the backward polar emission of the low-energy LCP from the ^{242}Pu (γ,f) reaction was observed using two different registration modes, namely when two decay partners were detected in the adjacent PIN diodes and within the double-hit approach.
2. Compared to the results obtained at the Berlin silicon ball (BSiB) for ^{252}Cf(sf) , we observed a whole range of LCP instead of only α-particles in that experiment, and the LCP yield ratio Y(VEGA)/Y(BSiB) was ~103, that is, three orders of magnitude higher in our experiment.
3. According to modern theoretical indications, the Coulomb interaction of the decaying fragment in the shape-isomer state with the target backing is presumably decisive for both differences.

References

1. Yu.V. Pyatkov et al., Proceedings of the International Symposium on Exotic Nuclei, Peterhof, Russia, 5-12 July 2004. Published by World Scientific Publishing Co. Pte. Ltd., 2005, pp. 351−356.
2. Yu.V. Pyatkov et al., Romanian Reports in Physics. 2007. V. 59, No 2. pp. 569−581.
3. Yu.V. Pyatkov et al., Eur. Phys. J. A: Hadrons and Nuclei. 2010. V. 45, No. 1. pp. 29–37.
4. D.V. Kamanin et al., Int. Journal of Modern Physics E. 2025. Vol. 34, No. 2 & 3. 2541002 (9 pages).
5. Yu.V. Pyatkov et al., Proceedings of the 27th International Seminar on Interaction of Neutrons with Nuclei (ISINN-27), Dubna, Russia, 10-14 June 2019. Dubna. 2020, pp. 249−252.
6. D.V. Kamanin et al., Physics of Particles and Nuclei Letters. 2025. Vol. 22, No. 2, pp. 272−275.
7. G.F. Knoll. Radiation detection and measurement. John Wiley & Sons, 2010p 625.
8. Yu.V. Pyatkov et al., Physics of Particles and Nuclei Letters. 2025. Vol. 22, No. 2. pp. 312−315.
9. The Nuclear Fission Process. Edited by Cyriel Wagemans. CRC Press. 1991.
10. V.G. Tishchenko et al., Study of ternary and quaternary spontaneous fission of ^{252}Cf with the NESSI detector, preprint HMI-B-588. Berlin, 2002.
11. E. Piasecki, et al., Nuclear Physics. A255 (1975). pp. 387−404.
12. F.O. Otakhonov et al., Int. J. Mod. Phys. E, 2641017 (2026).

The Process Opposite to the Neutron Radiative Decay

Khafizov R.U., Semenov S.V.

NRC "Kurchatov Institute"

Khafizov_RU@nrcki.ru

The report discusses the process opposite to neutron radiative decay, which we discovered experimentally at the FRMII reactor of the Physics Department at the Technical University of Munich in 2005. At that time, we were able to identify neutron radiative decay events using the triple coincidence method of three particles: a beta electron, a proton, and an additional particle - a radiative gamma quantum - and for the first time measure the relative intensity of neutron radiative decay B.R. = $(3.2\pm1.6)\cdot10^{-3}$ (where C.L. = 99.7% and the gamma-quantum energy threshold is 35 Kev) [1]. The experimental value we obtained is one and a half times higher than the theoretical value B.R.=$2.1\cdot10^{-3}$ [2], i.e., we registered additional gamma quanta. In this regard, it is interesting to study the process of reverse neutron radiative decay, namely, electron capture by a proton in strong electromagnetic fields. The report presents calculations of the cross section for the capture of a high-energy electron by a proton, which is of the order of 10^{-38} cm^2 for electrons with the energy of 1 GeV [3].

INTRODUCTION

In 2005, we performed an experiment in which, for the first time, we identified events of radiative neutron decay and measured its branching ratio (B.R.) It turned out to be B.R. = $(3.2\pm1.6)\cdot10^{-3}$ (the confidence level was C.L. = 99.7%, and the threshold in the photon energy was 35 keV) [1], which is 1.5 times as large as that which we calculated on the basis of the Standard Model B.R.= $2.1\cdot10^{-3}$ at the above energies of bremsstrahlung photons emitted by the beta electron and proton involved [2]. It is necessary to note here that we have indicated the C.L. value of 99.7%, which corresponds to an uncertainty of 3σ, whence it follows that the theoretical value of B.R. turned out to be lower than its experimental counterpart by more than two standard errors σ. This fact is indicative of detection of additional, so-called structural, photons.

Figure 1 shows neutron-decay processes in terms of Feynman diagrams. The first diagram corresponds to ordinary neutron beta decay, which, as is well known, leads to the production of three particles − a beta electron, a proton, and an antineutrino; this diagram describes a dominant mode of neutron decay. In our experiment, we recorded the number of such decays on the basis of double electron–proton coincidences. However, any decay process where charged particles appear in the final state involves a so-called radiative mode in which a photon is detected in addition to ordinary decay products. This extra photon is a bremsstrahlung photon that is emitted from a charged particle propagating in the braking electric field of the other charged particle. In the case of neutron decay, a bremsstrahlung photon may be emitted from the proton (second diagram in Fig. 1) and from the beta electron (third diagram in Fig. 1). However, yet another photon-emission process occurring in response to a change in the structure of the decaying particle itself may also exist. In the case of neutron decay (the respective process is depicted in the form of the fourth diagram in Fig. 1, where the photon escapes from the decay vertex itself), this is a so-called structural photon. In our experiment, we estimated the possible contribution of structural photons at a

level of 30% of the bremsstrahlung photon contribution corresponding to the second and third diagrams in Fig. 1.

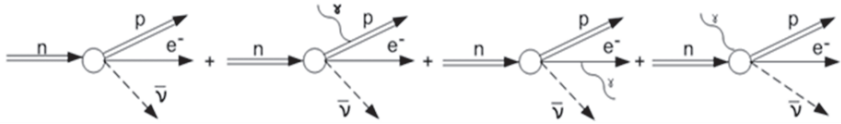

Fig. 1. Scheme of an ordinary beta decay and neutron decay involving photon emission.

In addition to radiative neutron beta decay, the inverse process of electron capture by a proton in the field of an electromagnetic wave is allowed. In the present study, we calculate the cross section for the capture of 1-GeV electrons by protons. The results show that this cross section is about 10^{-38} cm^2, which is six orders of magnitude larger than the cross section for reactor-antineutrino capture by protons. According to the results of numerous experiments aimed at detecting reactor antineutrinos in water, the detection rate for product neutrinos is about several hundred events per day [3–5]. But in our case of electron capture by protons, the neutron-detection rate at the same electron flux incident to the target as in the case of reactor-antineutrino flux incident to the detector in the experiments reported in [3–5] should be 103 to 104 neutrons per second, which is quite acceptable for implementing experiments in electron beams. According to the experimental results from [1], the inclusion of additional irradiation in the form of a laser electromagnetic field should lead to an increase in the neutron-production rate. Thus, it will be possible to estimate experimentally an increase in the cross section for the capture of high-energy electrons by protons in the field of an electromagnetic wave. Investigation of the reaction inverse to radiative neutron decay is of practical importance since this process is a source of particles of two species: the neutron and the neutrino. In a dedicated study, we will consider electron capture by a proton in a laser field.

CROSS SECTION FOR THE CAPTURE OF HIGH-ENERGY ELECTRONS BY PROTONS

The process

$$e^- + p \rightarrow n + \nu_e, \qquad (1)$$

which is allowed by the Standard Model, has been adequately studied for the K-capture case – that is the capture of a bound orbital electron by the respective nucleus. For example, this process is of great importance in implementing the gallium–germanium method for solar-neutrino detection [6] both for the determination of the counting rate (electron capture in ^{71}Ge) and for the creation of artificial neutrino sources for detector calibration—in the case of a ^{51}Cr source (electron capture by this nucleus) [7]. It is of interest to consider this reaction at high electron energies accessible at modern accelerators, $E_e \geq 1$ GeV.

We denote by q_1 the electron 4-momentum, by p the proton 4-momentum, by k the neutron 4- momentum, by q_2 the neutrino 4-momentum, and by and by E_e the electron energy in the laboratory frame. Since E_e =1 GeV, the electron mass can be disregarded. In the center-of-mass (c.m.) frame, the squared energy of the system is $s = (q_1 + p)^2$, while in the laboratory frame, where $p_p = 0$, we have $s = m^2 + 2m_p E_e$.

The amplitude for the process in (1) has the form

$$M=\frac{G_\beta}{\sqrt{2}}\bar{u}_n(k)\gamma_\alpha(1+\lambda\gamma_5)u_p(p)\bar{u}_\nu(q_2)\gamma_\alpha(1+\lambda\gamma_5)u_e(q_1).$$

$$M^*=\frac{G_\beta}{\sqrt{2}}\bar{u}_p(p)\gamma_\beta(1+\lambda\gamma_5)u_n(k)\bar{u}_e(q_1)\gamma_\beta(1+\lambda\gamma_5)u_\nu(q_2),$$

where $G_\beta=G_F\cdot\cos\theta_C$, $G_F = 1.1663787\cdot10^{-5}$ GeV^{-2} [8], $\lambda=1.2755$ [9], $\cos\theta_C= 0.9741$ [10]. Performing in the amplitude squared summation over spin states of the final particles and averaging over the electron and proton spins, we arrive at

$$|\bar{M}|^2 = \frac{G_\beta^2}{8}A_{\alpha\beta}B_{\alpha\beta}.$$

Here $A_{\alpha\beta} = Sp(\hat{k}+m_n)\gamma_\alpha(1+\lambda\gamma_5)(\hat{p}+m_p)\gamma_\beta(1+\lambda\gamma_5)$ and
$B_{\alpha\beta} = Sp\hat{q}_2\gamma_\alpha(1+\gamma_5)\hat{q}_1\gamma_\beta(1+\gamma_5)$.
Performing summation over α and β, we obtain

$$\begin{aligned}|\bar{M}|^2 &= 16G_\beta^2\{2(1+\lambda^2)(pq_1)(kq_2)+(\lambda-1)^2\big((kq_1)(pq_2)-(pq_1)(kq_2)\big)\\ &\quad + m_nm_p(\lambda^2-1)q_1q_2\},\\ |\bar{M}|^2 &= 16G_\beta^2\{(\lambda+1)^2\,(pq_1)(kq_2)\;+(\lambda-1)^2(kq_1)(pq_2)\\ &\quad + m_nm_p(\lambda^2-1)q_1q_2\}\end{aligned} \qquad (2)$$

In the c.m. frame, the differential cross section for the reaction in (1) can be represented in the form

$$d\sigma = \frac{1}{64\pi^2}|\bar{M}|^2\frac{|\boldsymbol{p}'_{\text{с.ц.и.}}|}{|\boldsymbol{p}_{\text{с.ц.и.}}|s}d\Omega'.$$

Here $\boldsymbol{p} = -\boldsymbol{q}_1 \equiv \boldsymbol{p}_{\text{c.m.}}$, $\boldsymbol{k} = -\boldsymbol{q}_2 \equiv \boldsymbol{p}'_{\text{c.m.}}$, $d^3\boldsymbol{p}'_{\text{с.ц.и.}} = \boldsymbol{p}'^2_{\text{c.m.}}d|\boldsymbol{p}'_{\text{c.m.}}|\,d\Omega'$.

At the high electron-energy values being considered, $E_e \geq 1$ GeV, we can set $kq_2 \cong pq_1$, $kq_1 \cong pq_2$, and $|\boldsymbol{p}'_{\text{c.m.}}| \cong |\boldsymbol{p}_{\text{c.m.}}|$.
For the total cross section, we have

$$\sigma^{tot} = \sigma^{(1)} + \sigma^{(2)} + \sigma^{(3)},$$

where $\sigma^{(i)}$ are determined by the respective terms in expression (2) for $|\bar{M}|^2$.

$$\sigma^{(1)} = \frac{G_\beta^2}{4\pi}(\lambda+1)^2\,\frac{(s-m_p^2)^2}{s}, \qquad (3)$$

$$\sigma^{(2)} = \frac{G_\beta^2}{12\pi}(\lambda-1)^2\frac{(s-m_n^2)^2}{s}\left(1+\frac{m_p^2}{s}+\frac{m_p^4}{s^2}\right), \qquad (4)$$

$$\sigma^{(3)} = \frac{G_\beta^2}{8\pi}(\lambda^2-1)\frac{m_nm_p(s-m_p^2)(s-m_n^2)}{s^2}. \qquad (5)$$

From expressions (3)–(5), it follows that a dominant contribution to the cross section at high electron energies comes from the term that is the first one in expression (2) and which corresponds to the isotropic distribution of directions of the vector $\boldsymbol{p}'_{\text{c.m.}}$ By way of example, we indicate that, at $E_e = 1$ GeV, we have

$$\frac{\sigma^{(2)}}{\sigma^{(1)}} \cong 0.007, \qquad \frac{\sigma^{(3)}}{\sigma^{(1)}} \cong 0.02\,.$$

Accordingly, we can assume that the distribution of secondary particles in reaction (1) is isotropic. The reaction cross section then has the form

$$\sigma(s) = \frac{G_\beta^2}{4\pi}(\lambda+1)^2\,\frac{(s-m_p^2)^2}{s}.$$

Going over to the laboratory frame, we obtain

$$\sigma(E_e) = \frac{G_\beta^2 m_p^2}{\pi}(\lambda+1)^2\,\frac{(\frac{E_e}{m_p})^2}{1+\frac{2E_e}{m_p}}. \tag{6}$$

In particular, $\sigma = 2.6\cdot10^{-38}\text{cm}^2$ at $E_e = 1$ GeV.

REACTION KINEMATICS

It is convenient to analyze the kinematics of the reaction in (1) by analogy with in-flight particle decay, 0→1+2 [11]. The method of analogies is useful in many fields of science [12]. By particles 1 and 2, we mean here the neutron and neutrino. It then follows that the c.m. frame of the process is the rest frame of particle 0 and that $\sqrt{s}$ plays the role of the rest mass m_0. The energies and momenta of particles 1 and 2 in the c.m. frame are determined by the values of $\sqrt{s}$, m_1, and m_2 and are independent of their emission direction. In the case of isotropy of the directions of motion of particles 1 and 2 in the c.m. frame − this is so under the condition $p_1 + p_2 = 0$ − their energy distributions in the laboratory frame are then rectangular and extend from E_i min to E_i max, i = 1, 2.

We have for neutron $E_{n,min}=m_n+\frac{\Delta^2}{2m_p}$, $E_{n,max} = E_e + \frac{m_p}{2} + \frac{m_n^2}{2(E_e+m_p)}$, and for neutrino $E_{\nu,min} = \frac{m_p}{2} - \frac{m_n^2}{2(E_e+m_p)}$, $E_{\nu,max} = E_e - \Delta - \frac{\Delta^2}{2m_p}$. Here, $\Delta = m_n - m_p = 1.29$ MeV. The minimum kinetic energy of the neutron in the laboratory frame is independent of the electron energy and $E_{nkin,min} = \frac{\Delta^2}{2m_p} = 0.9$ KeV.

In contrast to what we have in the c.m. frame, the momenta of the particles in the laboratory frame depend on their emission direction − that is, on the angle between pi and the electron momentum q1. The neutrino, which, in the problem being considered, may be viewed as a massless particle, can be emitted at any angle between 0 and π. At the same time, neutron emission angles are limited by the angle θ_{max}, and all neutrons are emitted into the right-hand hemisphere. This is so because the velocity of motion of the c.m. frame $v_{c.m.}$ in the laboratory frame is greater than the neutron velocity v_n^0 in the c.m. frame:

$$v_{c.m.} = \frac{E_e}{E_e + m_p}, \qquad v_n^0 = \frac{s-m_n^2}{s+m_n^2}, \qquad v_{c.m.} - v_n^0 \cong \frac{\Delta(2E_e+m_p)}{2(E_e+m_p)^2}.$$

The expression for the sine of the maximum emission angle of the neutron originating from the reaction in (1), $\sin\theta_{n,max}$, has the form [11]

$$\sin\theta_{n,max} = \frac{m_0 p_{n,с.ц.и.}}{m_n p_0},$$

where, for (1) $m_0 = \sqrt{s}$, $p_{n,с.ц.и.} = \frac{s-m_n^2}{2\sqrt{s}}$, $p_0 = E_e$. As a result, we obtain

$$\sin\theta_{n,max} = \frac{m_p}{m_n} - \frac{m_n^2 - m_p^2}{2m_n E_e}. \tag{7}$$

From expression (6), it follows that, in the limit of high electron energies E_e, the neutron emission angle does not exceed $\arcsin(m_p/m_n) = 87^0$. At E_e =1 GeV, we have $\theta_{n,max} \cong 85.8^0$. This fact facilitates the detection of neutrons produced in the reaction being considered, since all of them fly into the forward hemisphere. In turn, this simplifies substantially the design of the detector. In this report we consider the electron capture by proton without the influence of strong 'electromagnetic fields [13]. This influence we will consider in separate report.

CONCLUSIONS

To complete our analysis we will estimate the flux of neutrons produced in the capture of 1 GeV electrons by protons in water. We denote by i_e the current of high-energy electrons and by n_p the proton concentration which is equal to $3.33 \cdot 10^{23}$ cm^{-3} for water.

The neutron-production rate R is then given by

$$R = \frac{i_e n_p}{e} \int_0^{l_{max}} \sigma(E_e\,(l))dl\,,$$

where l is the distance traveled by the electron beam in the target. Under the assumption of an exponential dependence of the electron energy on l, $E_e(l) = E_e e^{-\frac{l}{\eta(E_e)}}$, $l_{max} >> \eta(E_e)$ and upon taking into account expression (6) for the capture cross section $\sigma(E_e)$, we obtain

$$R = \frac{i_e \sigma_0 \eta(E_e,) n}{e} \xi(E_e).$$

Here $\sigma_0 = \frac{G_\beta^2 m_p^2 (\lambda+1)^2}{\pi} = 7.29 \cdot 10^{-38}$ см^2, $\xi(E_e) = \frac{1}{4}\left(\frac{2E_e}{m_p} - \ln\left(1 + \frac{2E_e}{m_p}\right)\right)$.

At i_e = 100 mA, E_e = 1 GeV, and η (E_e) = 0.36 m, we have $R = 1.4 \cdot 10^5$ neutrons per second. As has been shown above, all neutrons are emitted into the forward hemisphere. This fact simplifies substantially the geometry of the detector to be used and permits the detection of all neutrons produced as the result of capture.

ACKNOWLEDGEMENTS

We are grateful to Yu.V. Kozlov, Yu. S. Lutostansky, S.V. Tolokonnikov, and V.D. Torokhov (National Research Center, Kurchatov Institute) for stimulating discussions.

REFERENCES

1. R.U. Khafizov, N. Severijns, O. Zimmer, H.-F. Wirth, D. Rich, S.V. Tolokonnikov, V.A. Solovei, and M.R. Kolhidashvili, JETP Lett. 83, 5 (2006). https://doi.org/10.1134/s0021364006010024
2. Yu.V. Gaponov and R.U. Khafizov, Phys. Lett. B 379, 7 (1996). https://doi.org/10.1016/0370-2693(96)00398-X
3. G.S. Vidyakin, V.I. Vyrodov, I.I. Gurevich, Yu.V. Kozlov, V.P. Martem'yanov, S.V. Sukhotin, V.G. Tarasenkov, and S.Kh. Khakimov, J. Exp. Theor. Phys. 66, 243 (1987).
4. G.S. Vidyakin, V.I. Vyrodov, Yu.V. Kozlov, V.P. Martem'yanov, S.V. Sukhotin, V.G. Tarasenkov, S.Kh. Khakimov, and A.S. Khrustal', Prib Tech. Eksp. 4, 70 (1989).

5. V.I. Vyrodov, M.I. Gurevich, Yu.V. Kozlov, S.V. Marin, A.V. Martem'yanov, V.P. Martem'yanov, N. Machulin, A.A. Sabel'nikov, S.V. Sukhotin, V.G. Tarasenkov, E.V. Turbin, and S.V. Khalturtsev, "Results of proton back beta decay measurements on the modernized Dayton detector," Preprint, RNTs KI (National Research Centre Kurchatov Institute, Moscow, 1997).
6. V.A. Kuz'min, Zh. Eksp. Teor. Fiz. 49, 1532 (1965).
7. J.N. Abdurashitov, V.N. Gavrin, S.V. Girin, V.V. Gorbachev, T.V. Ibragimova, A.V. Kalikhov, N.G. Khairnasov, T.V. Knodel, V.N. Kornoukhov, I.N. Mirmov, A.A. Shikhin, E.P. Veretenkin, V.M. Vermul , V.E. Yants, G.T. Zatsepin, Yu.S. Khomyakov, et al., Phys Rev. C 59, 2246 (1999). https://doi.org/10.1103/physrevc.59.2246
8. C. Patrignani (Particle Data Group), Chin. Phys. C40, 100001 (2016). https://doi.org/10.1088/1674-1137/40/10/100001
9. A. Czarnecki, W.J. Marciano, and A. Sirlin, Phys. Rev. Lett. 120, 202002 (2018). https://doi.org/10.1103/physrevlett.120.202002
10. J.C. Hardy and I. S. Towner, Phys Rev. C 91, 25501 (2015). https://doi.org/10.1103/physrevc.91.025501
11. G.I. Kopylov, Fundamentals of Resonance Kine- matics (Nauka, Moscow, 1970).
12. G.I. Kopylov, E. Stromynkin (Fizicheskii Fakul'tet, Moskovskii Gosudarstvennyi Universitet, Moscow, 2016).
13. С.В. Семенов, Р.У. Хафизов, ЯФ, т. 88, №4, (2025), с. 355 (in Russian).

Conversion of the Monte-Carlo Neutron Transport Program Code 'SHIELD' to Work Together with the 299-Group Cross Sections of Neutron-Nucleus Interactions 'ABBN-93'

Sobolevsky N.M., Djilkibaev R.M., Khliustin D.V.

Institute for Nuclear Research, Russian Academy of Sciences, Moscow, Russia
denhlustin@gmail.com

1. Introduction

In the Institute for Nuclear Research of the Russian Academy of Sciences continues work on conversion of the SHIELD Monte Carlo calculation code to work with the 299-group ABBN-93 system of neutron-nucleus interaction constants, the current standard of Rosatom.

In this paper we calculate neutron leakage spectra and absorption spectra for uranium-238 metallic spheres of various radiuses with a central 14 MeV neutron source. The average neutron energy and lifetime are given for each spectrum. A comparison of calculation results, performed using the 28-group ABBN-78 system and the modern 299-group ABBN-93 system, is discussed. The calculated spectra provide the opportunity to compare them with the experimental spectra, measured by the TOF method in corresponding integral experiments.

Correction of group constants based on the results of TOF spectrometry of integral experiments is a development of ideas, expressed in the 1980s by Yu.Ya. Stavissky [1] and is one of the main project tasks of the Moscow Meson Factory. The correction can be performed, first of all, inside the precision range declared by the authors of the constants, which for ABBN-93 is ±0.5%.

2. Description of the model

Sphere with radius R is taken as a model geometry, made of solid state nominal density p=18900 kg/m3 metal uranium-238. At the moment t=0 in the center of the sphere N=10.000.000 neutrons are injected which have energy 14.1 MeV.
Program calculates:

1) outgoing spectrum of neutrons, which after diffusion through uranium escape from the external surface of the sphere;
2) spectrum of captured neutrons;
3) average energy of neutrons and average diffusion/absorption time for each spectrum;
4) number of interactions in different chains of neutron reactions.

3. Calculated spectrums for ^{238}U spheres of various radiuses

In the pictures from №1 to №12 calculated spectra are shown. Number of injected neutrons is 10,000,000 for all calculations. On the horizontal axis there is number of energy group: big number corresponds to low neutron energy, while energy of neutrons in the 1st group is 20 MeV. Thus, as usually here low energies from left side, big energies from right side. On the vertical axis is shown a number of neutrons per one ABBN-93 energy group in logarithmic scale.

Blue curve is used on each picture for outgoing spectrum of neutrons, which escape from the external surface of ^{238}U sphere and can be registered experimentally, for example, using TOF method. Red color is used on each picture for spectrum of neutrons, which are captured inside ^{238}U during diffusion process.

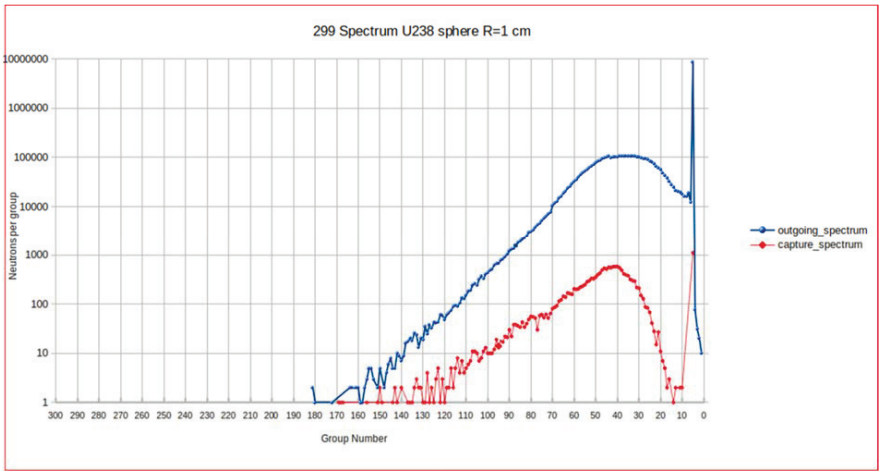

Fig.1. Spectrums for ^{238}U sphere with radius R=1 cm.

On the spectrums for R=1 cm we find that big share of initial 14 MeV neutrons escape from the uranium without interaction.

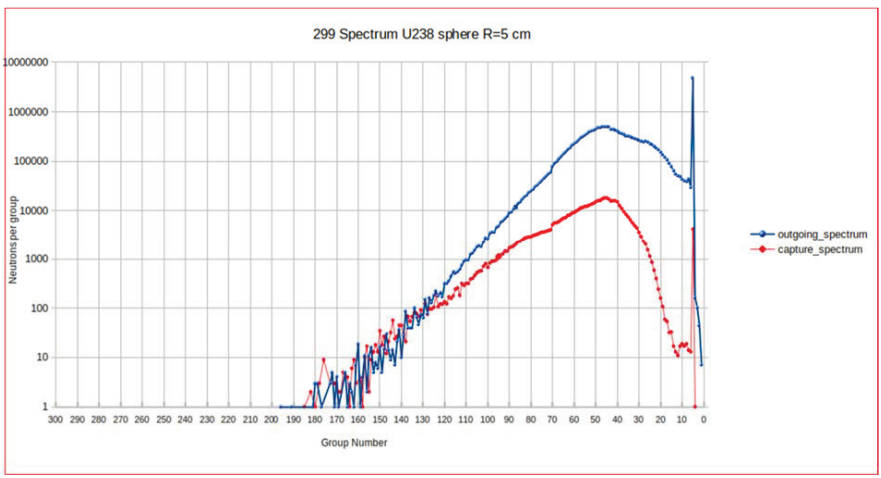

Fig.2. Spectrums for ^{238}U sphere with radius R=5 cm.

In each of 12 pictures, average energy of outgoing spectrum and average energy of capture spectrum differs one from another in one and the same assembly. In early nuclear era's literature was discussed only 'the spectra of the reactor', but in detailed calculations we see, that captured and outgoing neutrons are two strongly different spectrums. The task appears: to be able to recreate the capture spectrum by numerical modeling, following which we have experimentally measured outgoing spectrum. Breeding ratio of fast neutron reactor is defined by neutron capture spectrum, so as number of fissile secondary neutrons in fission reaction depends on initial neutron's energy, while only outgoing spectrum can be measured experimentally by TOF method.

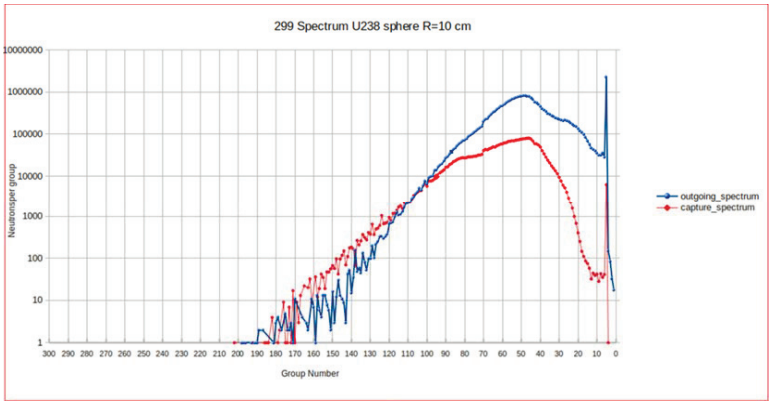

Fig.3. Spectrums for ^{238}U sphere with radius R=10 cm.

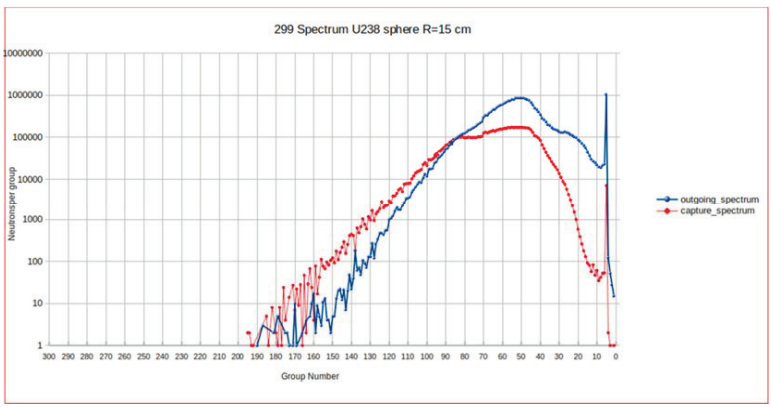

Fig.4. Spectrums for ^{238}U sphere with radius R=15 cm.

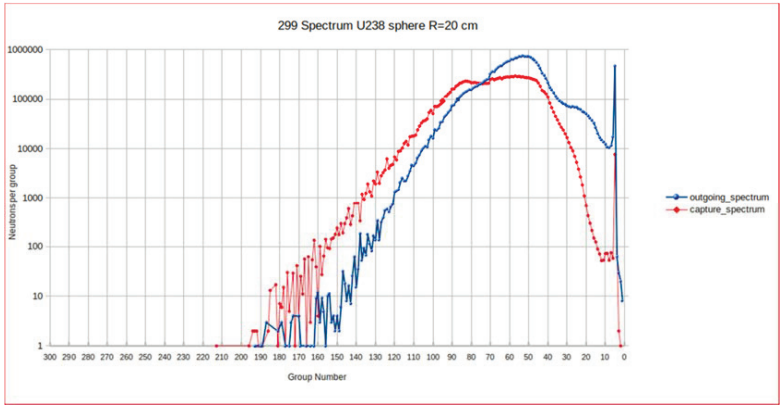

Fig.5. Spectrums for ^{238}U sphere with radius R=20 cm.

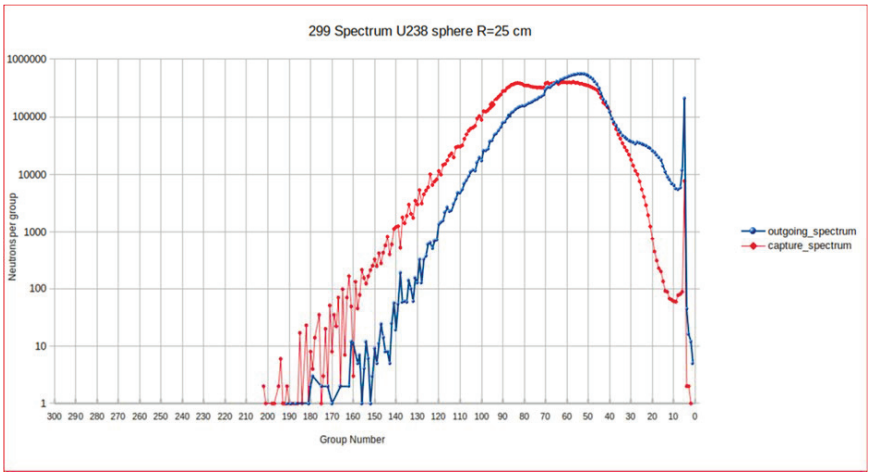

Fig.6. Spectrums for ^{238}U sphere with radius R=25 cm.

In figures 3−6 we note that capture spectrum and outgoing spectrum not only change non-linearly from picture to picture as a function of uranium assembly's radius. Even in one and the same figure, spectrums aren't copy of each other, and difference in high energy area of neutrons is especially significant. High energy region is very sensitive to uranium sphere's radius.

At big radiuses, share of initial 14 MeV neutrons becomes small. Majority of neutrons participate in inelastic scattering and in big amount of elastic scatterings, thus, even statistics

10,000,000 initial neutrons allows to follow the spectrums in more than a half of all energy groups on logarithmic energy axis.

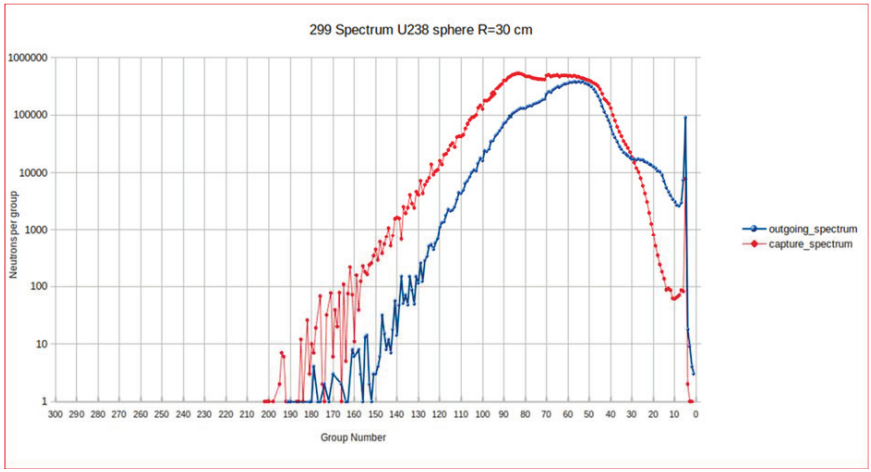

Fig.7. Spectrums for ^{238}U sphere with radius R=30 cm.

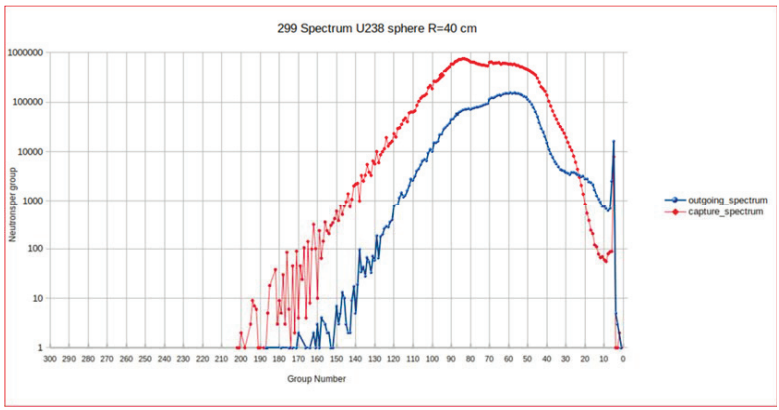

Fig.8. Spectrums for ^{238}U sphere with radius R=40 cm.

In figures from number 8 to number 11 we observe continuation of evolution of both spectra. After radius exceeded 30 cm, we increased the step between neighbor pictures because energies of majority of neutrons are already below threshold of inelastic scattering. Average neutron energies with increasing of assembly's radius continue to decrease only due

to elastic scattering of neutrons, and this process goes much less fast compared to inelastic scattering.

In figure 12 we have capture spectrum, when almost all initial and secondary neutrons are already captured. This curve can be called 'own capture spectrum of the substance', of ^{238}U in our case, because in the volume of the assembly there is no any other substance, which could influence on both spectrums. Necessary to note, that average neutron spectra's energies for big thicknesses were found around 140 keV. This value is 100 times less than initial neutron's energy, and it already can be measured by existing TOF spectrometers using long TOF bases.

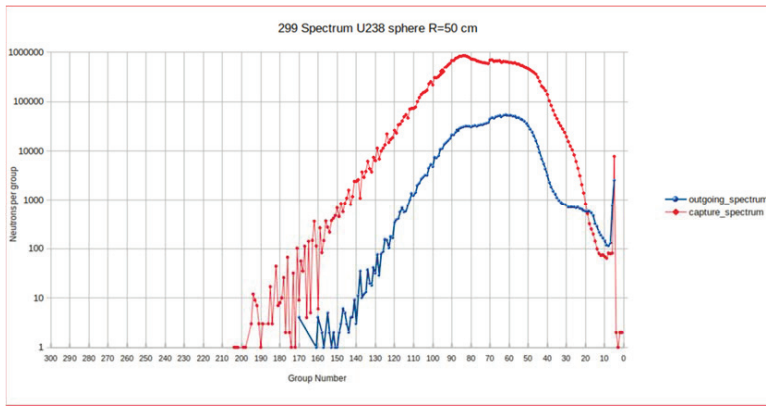

Fig.9. Spectrums for ^{238}U sphere with radius R=50 cm.

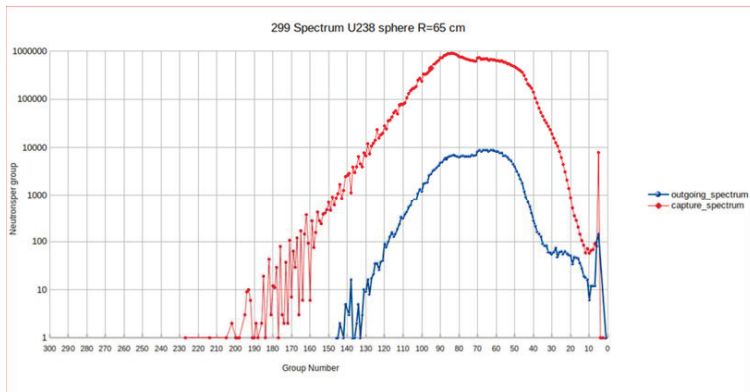

Fig.10. Spectrums for ^{238}U sphere with radius R=65 cm.

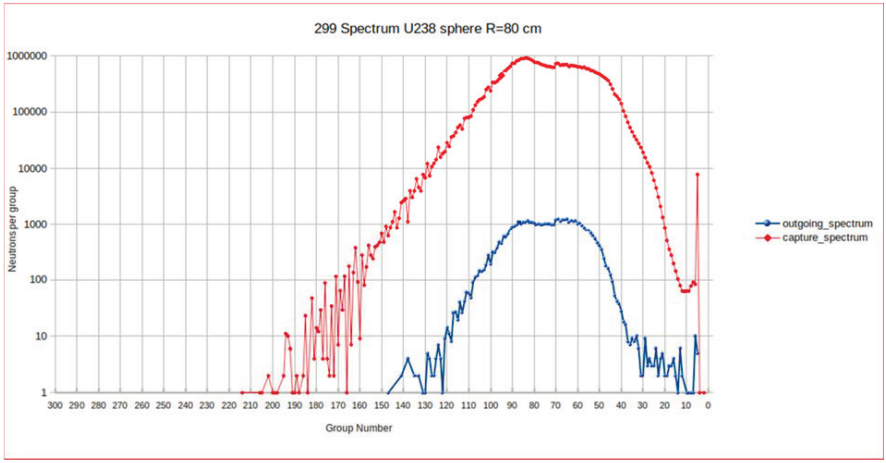

Fig.11. Spectrums for ^{238}U sphere with radius R=80 cm.

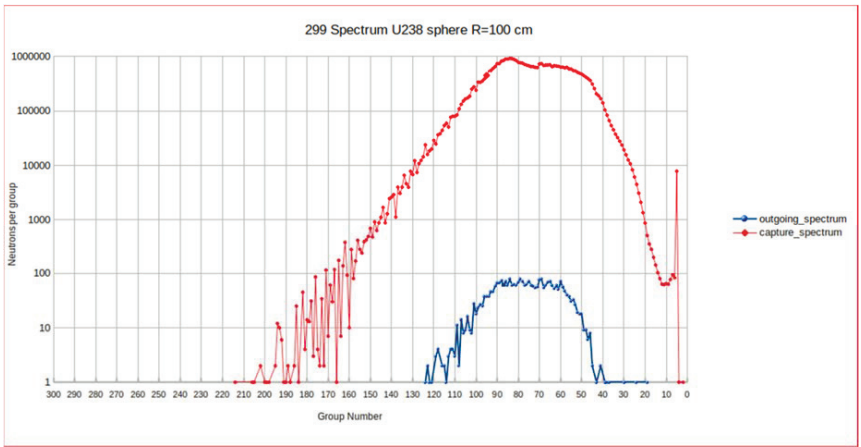

Fig.12. Spectrums for ^{238}U sphere with radius R=100 cm.

4. Conclusion

Integral experiments are integral check of all main types of nuclear constants, of cross sections for interaction of neutrons with nuclei, as suggested in [1]. Present work makes a supplement for the prepared stock of calculated spectrums, adding 299-grouped data on ^{238}U spheres. These data are basis for comparison with future experimental TOF spectra.

In addition for conclusions about integral experiments themselves, which were formulated in [2–6], is necessary to note advantages of 299-group calculations. Energy width of each group in 299-group approach corresponds to elastic scattering of neutrons on sodium ^{23}Na while previous multi-year Rosatom's standard ABBN-78, which had 28 energy groups, corresponds to moderation on deuterium. Due to availability of various light nuclides in the volume, for majority of reactor tasks and radiation shield tasks, 299 groups are enough. Small-stepped variant calculations, allows to reconstruct capture spectrum, in the case if experimentally measured outgoing leakage spectrum is available. More detailed curve, in the case of 299 groups, allows to reconstruct better the high energy part of spectrum, where difference between capture spectrum and outgoing spectrum turns out especially large, while high energy neutrons are especially significant for reactor's performance.

Comparing 299-group approach of the SHIELD program and MCNPX, which instead of energy groups uses continuous curves of cross sections, necessary to note that exist several practical advantages of 299-group approach:

1. Modern available in ENDF/B-VIII cross sections of plenty isotopes still have value of upper energy border of resolved resonances much less, than energy, where Doppler effect physically mixes neighbor resonances. Energy region of unresolved resonances in nuclear data for plenty isotopes still exists.
2. For total cross section of ^{238}U the best available curve consists of about 8000 points. Our task to compare calculated and experimental spectrums of ^{238}U spheres requires statistics, which allows to get precision around 0.2% in each energy group of main part of spectrum. In the case of 299 energy points, statistics 10,000,000 – 100,000,000 is enough for our task. This statistics, even for assemblies with big radiuses, can be done using several modern notebooks.
3. In the case of values such as 8,000 energy groups and more, for precision value 0.2% in each energy interval (so as it's compared with experimental curve to modify cross sections), calculation must be done using multi-processor computer (1000 processors and more). This requires both to have access to significant machine time of such computer, and that program code must be re-written for compatibility with multi-processor mode.

With statistics 100,000,000 neutrons for each variant, performance of the 299-group version of the program allows to calculate enough quantity of variants per year, using several modern personal computers. Available statistics provides discreteness calculation precision component better than value of delayed neutron's share, which is 0.2% in the case of nucleus ^{239}Pu i.e. actual for fast breeder reactors. High enough statistics define, that for majority of energy groups, their data difference between ABBN-93 and experiment - is not due to statistical scatter, but due to the difference in cross sections precision. In a precision setting, the results of integral experiments are the basis for [1] adjusting group neutron constants, intended for calculation of nuclear reactors and radiation shields.

References

1. Stavissky Yu.Ya. Neutron Research based on Moscow Meson Factory. In: 'Program of experimental research at Meson Factory INR RAS', volume 4, Moscow, 1986, p.7−21.

2. Sobolevsky N.M., Latisheva L.N., Djilkibaev R.M., Khliustin D.V. Evolution of the Neutron Spectrum During Propagation of the Neutron Flux in Solid Bodies. International Conference Nucleus-2024, Dubna, Russia, 2024.
3. Соболевский Н.М., Латышева Л.Н., Джилкибаев Р.М., Хлюстин Д.В. Эволюция Нейтронного Спектра при Распространении Потока Нейтронов в B10, Ti и U238. IV Всероссийская научно-практическая конференция с международным участием «Задачи и методы нейтронных исследований конденсированных сред», Дубна, 2024.
4. Sobolevsky N.M., Latisheva L.N., Djilkibaev R.M., Khliustin D.V., Simulation of Spectra's Evolution During Propagation of the Neutron Fluxes in Solid Bodies. Session-Conference 'Physics of Fundamental Interactions', Department of Physics, Russian Academy of Sciences. 17−21 February 2025, Presidium RAS, Moscow, Russia.
5. Sobolevsky N.M., Latisheva L.N., Djilkibaev R.M., Khliustin D.V., Evolution of Spectra During Propagation of Neutron Fluxes in Rhenium, Molybdenum and Aluminum. LXXV International Conference 'NUCLEUS-2025. Nuclear physics, elementary particle physics and nuclear technologies'. St. Petersburg State University, 01−06 June 2025, Saint Petersburg, Russia.
6. Sobolevsky N.M., Latisheva L.N., Djilkibaev R.M., Khliustin D.V., Evolution of the Neutron Spectrum During Propagation of the Neutron Flux in Eu, Cr and Si. V All-Russia Scientific-Practical Conference 'Tasks and Methods for Neutron Researches of Condensed Matter', 24−27 November 2025, 'Dubna' State University, Russia.

Literature

1. Dementyev A.V., Sobolevsky N.M. SHIELD – Universal Monte Carlo hadron transport code: scope and application. Radiation Measurement 30 (1999) p.554−557. https://www.inr.ru/shield
2. Абагян Л.П., Базянц Н.О., Николаев М.Н., Цибуля А.М. Групповые константы для расчёта реакторов и защиты. Справочник. Москва, Энергоатомиздат, 1981.
3. Manturov G.N., Nikolayev M.N.,Tsibulya A.M. System of group constants ABBN-93. Part 1. Nuclear constants for calculation of neutron and photon fields of emission. VANT, 'Nuclear Constants', №1, 1996, p.59−98. https://www.bnl.gov
4. Уолтер А., Рейнольдс А. «Реакторы-размножители на быстрых нейтронах», Энергоатомиздат, 1986, с.313.

Measurement of Holmium-165 Spectra at the INES TOF Spectrometer of the Spallation Neutron Source RADEX

Djilkibaev R.M., Khliustin D.V.

Institute for Nuclear Research, Russian Academy of Sciences, Moscow, Russia
denhlustin@gmail.com

Abstract. The work presents experimentally measured TOF spectra, obtained using samples-radiators of holmium-165, patterns 1.8 mm and 9 mm thickness as target materials at the INES TOF spectrometer. Data were measured using 8-sectional 40-liter liquid scintillator gamma-detector. Helium-3 counters SNM-18 were used as a neutron source intensity monitor. Obtained data are presented in the energy borders of the groups of the'ABBN-93' neutron constants, are compared with ENDF/B-VIII and other available literature sources. Resonance structure is discussed. Measurements were carried out with a channel duration 100 nanoseconds of the data acquisition system which covered 20 millisecond duration period of the 50 Hz by 200,000 histogram channels, and proton linear accelerator operating with parameters: proton beam duration 250 nanoseconds at half-maximum current amplitude, proton beam energy 364 MeV, flash frequency 50 Hz, pulse current 0.01 amperes. TOF spectrometer base 50 meters provided resolution factor: 6 nanoseconds per meter.

1. Introduction

Available literature Data for holmium-165 capture cross section [1] shows, that upper energy border of resolved resonances is currently at 1250 eV for this isotope.

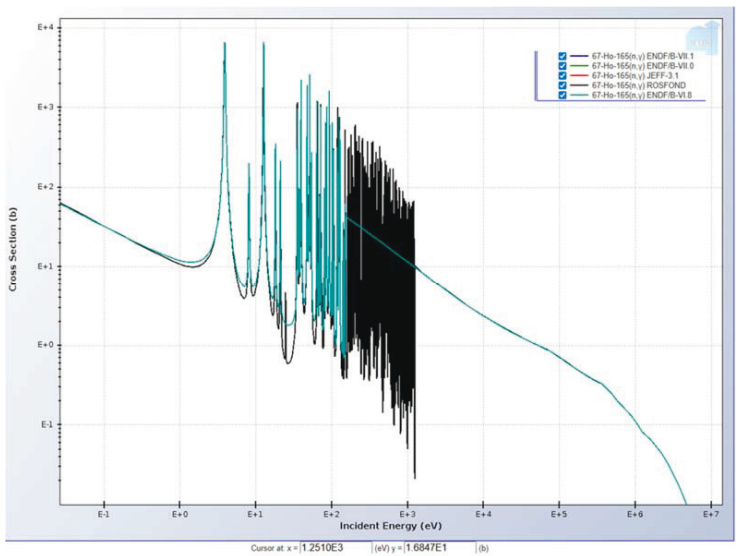

Fig. 1. Holmium-165 capture cross section in the energy region 0.0253 eV < E_n < 14 MeV.

Disputed resonances between databases are observable at energies: 24.7 eV, 64 eV and 65.2 eV, 75.1 eV; 120 and 120.6 eV.

During measurements, intensity of the proton accelerator's beam was measured by signals from six He-3 monitors SNM-18, which are used on the opened beam. Maxwell's spectrum thermal peak has energy 0.06 eV. This exactly matches with the reactor theory: although H_2O in the moderator has temperature 300 Kelvins, temperature of neutron spectrum is higher than 0.0253 eV, what must be in the case of both not-infinitive media of H_2O (3 cm thickness) and non-zero absorption of neutrons (Fig.2).

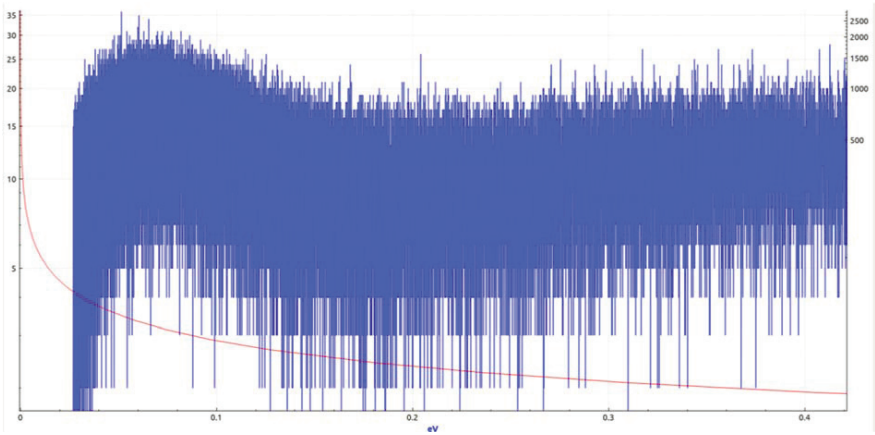

Fig.2. He-3 monitor, energy region below 0.4 eV, Maxwell's peak is observable.

2. Neutron energy region of resolved resonances

First capture holmium-165 resonance, at E_n=3.9 eV, is observed by 8-sectional liquid gamma-detector with big block-effect on metal plate pattern 1.8 mm thickness (Fig. 3).

Energy interval ABBN-78 group number 22 includes twelve ABBN-93 groups: numbers from 227 to 238.

Were exactly distinguished several resonances at lowest energies, which are admixtures of seven natural dysprosium isotopes. Especially strongly influences isotopes ^{163}Dy and ^{162}Dy, which have cross section up to 10,000 barns and 45,000 barns correspondingly. Necessary to note, that roentgen-stricture analysis didn't show presence of any admixtures in holmium pattern due to their trace amounts, appreciated around 0.01%. This means that usage of TOF method for purposes of structural analysis of solid bodies shows better sensitivity than any other method and additionally is able to distinguish isotopes.

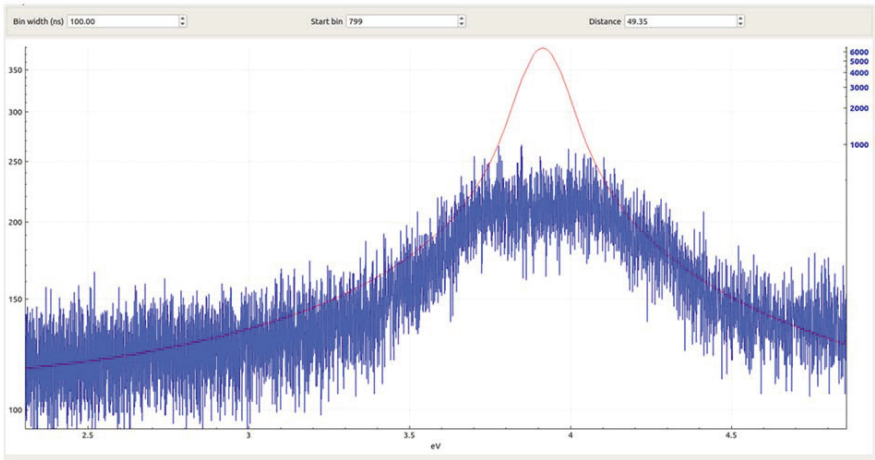

Fig.3. ^{165}Ho capture cross section, energy interval is ABBN-78 group number 22.

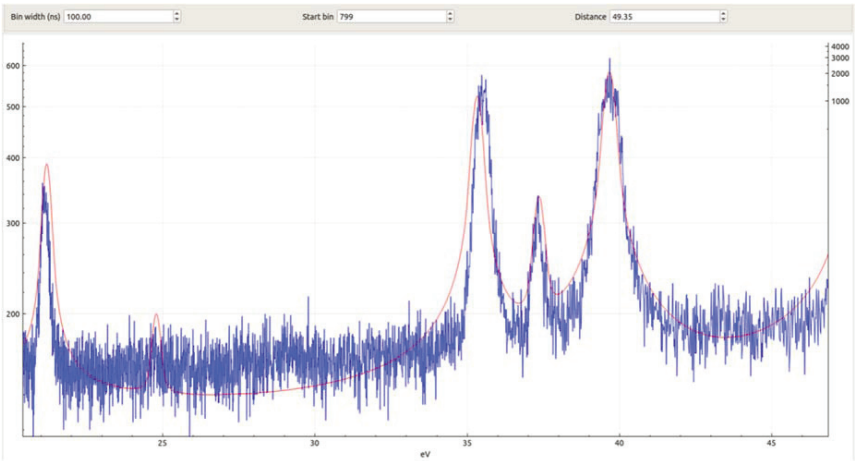

Fig.4. Energy interval is ABBN-78 group number 19.

In Fig.4 is shown neutron energy interval ABBN-78 group number 19, which includes twelve ABBN-93 groups: numbers from 191 to 202.

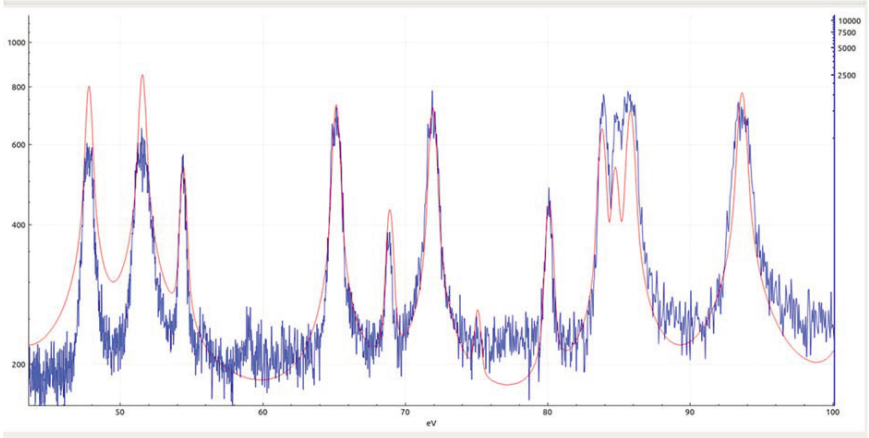

Fig.5. Energy interval is ABBN-78 group number 18.

ABBN-78 group number 18 includes twelve ABBN-93 groups: numbers from 179 to 190. Experimental resonance parameters of level at 85 eV differ from the reference data in Fig.5.

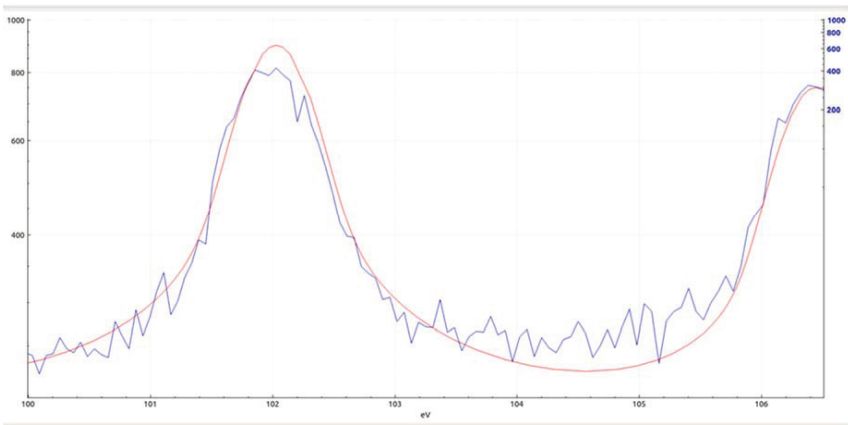

Fig.6. Energy interval is ABBN-93 group number 178.

ABBN-93 energy interval (see Fig.6) is one order of magnitude narrower, as compared to ABBN-78. Nevertheless, RADEX TOF spectrometer performance allows to measure ^{165}Ho capture cross section in all resolved resonances area, i.e. in the lowest 160 ABBN-93 groups

of 299. The same experimental data allows to measure group cross sections up to 100 keV: up to 71st group, i.e. 228 groups of 299.

Red curve on all pictures depicts data ENDF-B/VIII [1]. Left side axis – counts per SSD histogram channel. Right axis is in barns for data [1].

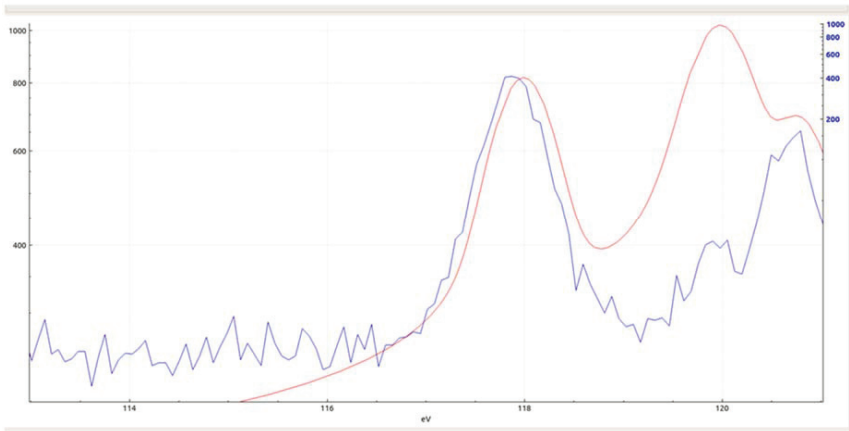

Fig.7. ABBN-93 energy group number 176.

In the energy group №176, shown in Fig.7, we found that experimental curve differs from the ENDF/B-VII.1 data: two close resonances near 120 eV, and bigger cross section has resonance with bigger energy. This is in good agreement with ROSFOND and earlier version of ENDF/B-VI.8, where first resonance was absent while second was available.

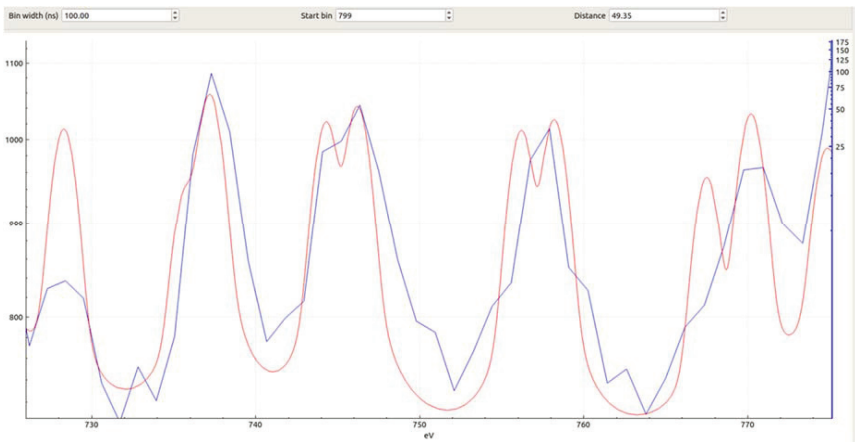

Fig.8. ABBN-93 group number 147.

Necessary to mention, that even at relatively big energies in Fig.8, where 726 eV < E_n < 774 eV, and experimental curve contain small amount of points per each resonance, we observe good coincidence between our experimental curve and best world data, if we speak about area under the curve which defines group cross section. While for definition of resonance parameters of separate resonances, better energy resolution is needed.

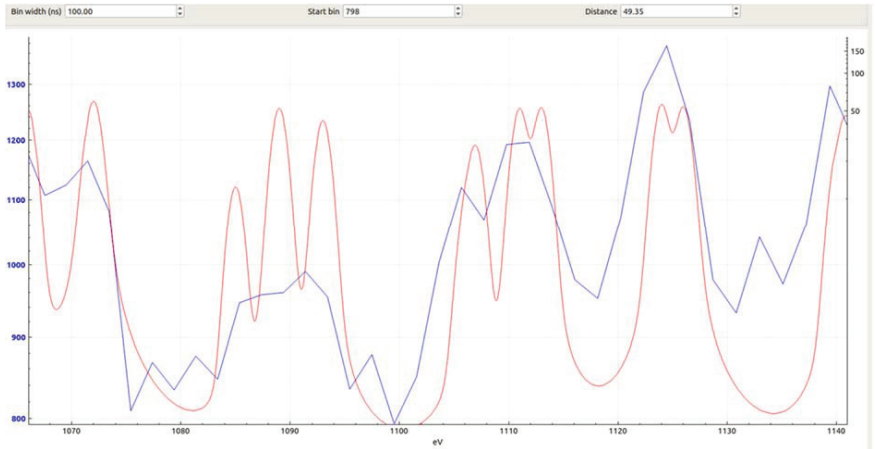

Fig. 9. ABBN-93 group number 141.

In the energy interval 1066 eV < E_n < 1136 eV, shown in Fig.9, energy resolution of the spectrometer still allows to distinguish groups of resonances and define area under them, needed to get group cross sections.

Were precisely defined start bin and TOF base, which resulted 49.35 meters. Exactness of these two values is especially important for high energy part of experimental histogram.

3. Capture cross section in the region of unresolved resonances

In the unresolved resonances area, spectrometer's energy resolution is not enough to extract resonance parameters. So as Doppler effect mixes all neighbor resonances into continuous curve at more high energies than 1250 eV for ^{165}Ho, due to energy resolution 6 nanoseconds per meter we observe peaks which are groups of resonances. However, group cross sections have good statistical precision, and can be extracted: if we can distinguish effect from the background curve.

In Fig.10 resolved resonance's curve becomes averaged curve above 1250 eV, while on experimental curve we exactly observe peaks which are groups of resonances. Their averaged area, considering good enough statistics on left axis (in counts per each point on energy axis), allows to extract group cross sections.

Energy intervals in Fig.11 is 1000 eV < E_n < 4700 eV. Vacuum neutron guide plugs, made from aluminum alloy, contain isotope manganese-55, which extract neutrons from the beam by action of total cross section. To decrease this effect, we replaced them by plastic

diaphragms thus deleted 3 millimeters of aluminum from the neutron beam. However, casing for tungsten proton beam 1 MW target of the spallation source RADEX is itself made from aluminum alloy.

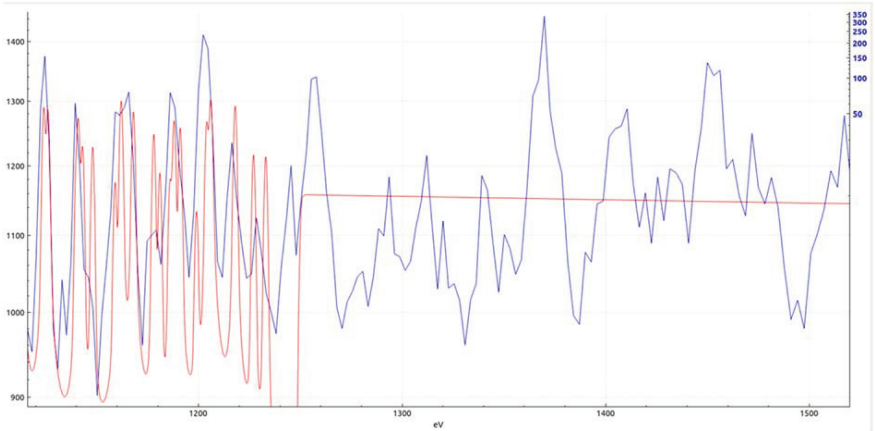

Fig.10. Energy interval in the picture – ABBN-93 groups 141, 140, 139, 138, 137 and 136.

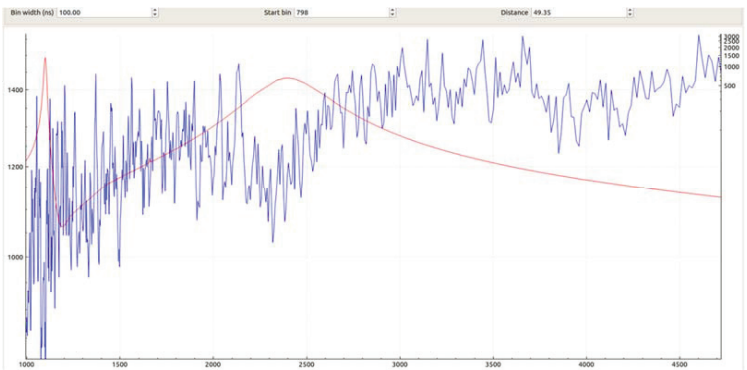

Fig.11. Energy interval – ABBN-93 groups number from 142 to 119.

In the picture, neutron consumption at energies 1100 eV and around 2400 eV is clearly observable in this wide interval on energy axis.

In Fig.12 experimental curve between 5000 eV and 10,000 eV is shown. Neutron consumption by aluminum-27 plugs of a vacuum neutron guide, at 5900 eV, can be used to appreciate the background layer in the area of unresolved resonances. However, it is better to have energy resolution higher than 6 nsec/meter.

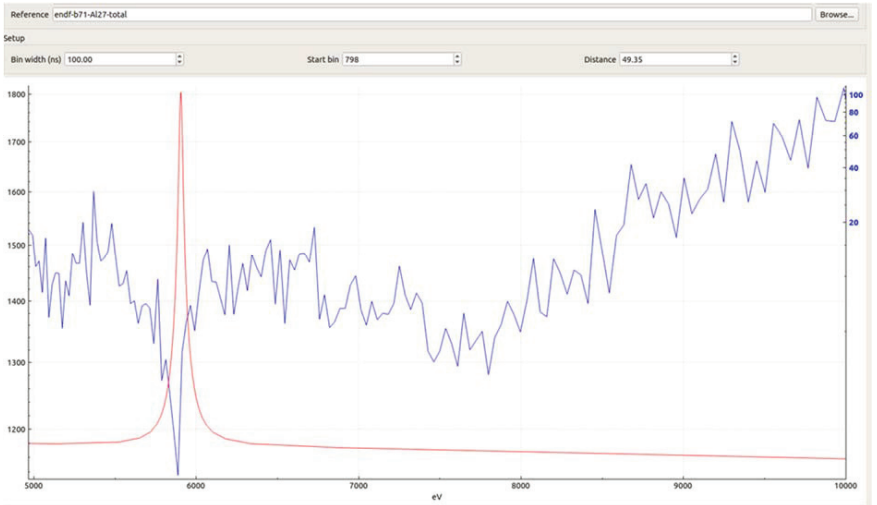

Fig.12. Energy interval – ABBN-93 groups number 117 to 107.

In Fig.13 energy interval is 22 keV < E_n < 46 keV. Total cross section of ^{56}Fe, which is used in the RADEX proton beam target, results into consumption of neutrons at the neutron energy 28 keV. So as resonance is wide enough and 'black', it can be used for background determination.

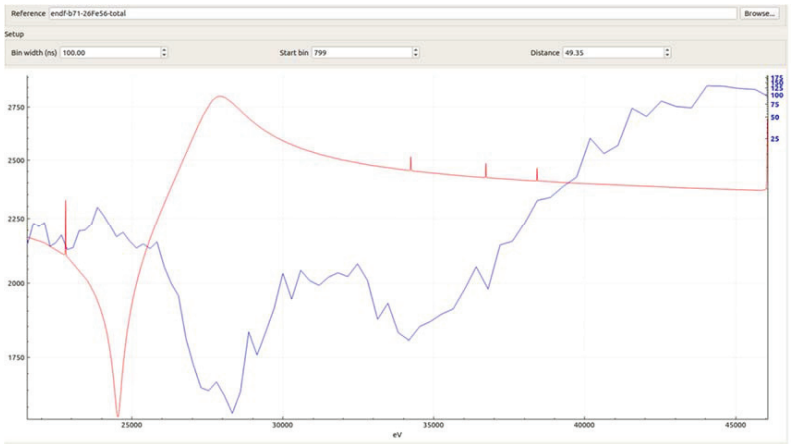

Fig.13. Energy intervals are ABBN-93 groups number from 93 to 83.

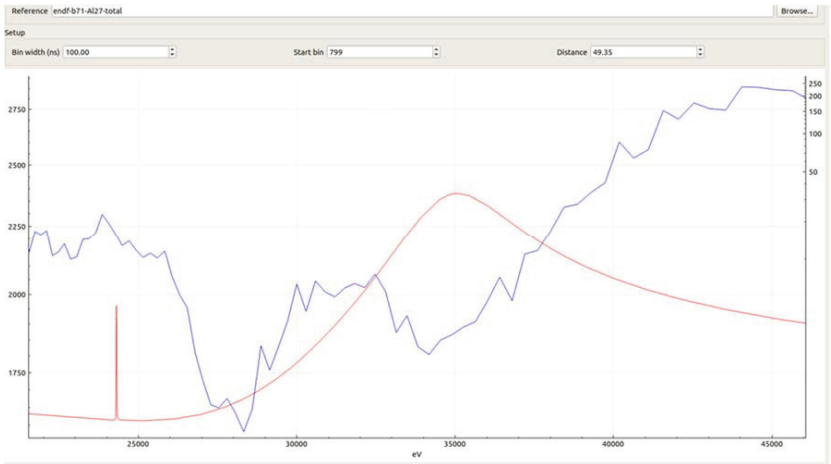

Fig.14. Energy intervals are ABBN-93 groups number from 93 to 83.

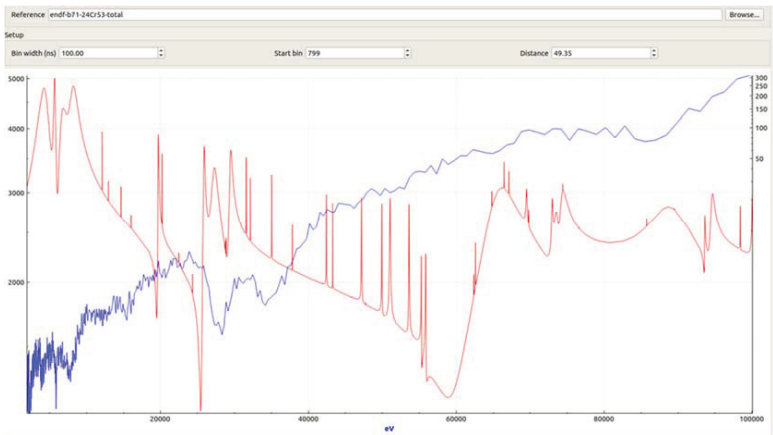

Fig 15. Energy intervals are ABBN-93 groups numbers from 130 (2296.74 eV) to 71 (100 keV).

Aluminum-27 total cross section resonance, shown in Fig.14, causes the neutron consumption at the energy 35 keV. Necessary to note, that on experimental curve of He-3 monitors, these two resonances, ^{56}Fe at 28 keV and ^{27}Al at 35 keV, are observed as one resonance due to very long pulse duration and time-scatter of He-3 counters, which is experimentally between 3 and 4 microseconds. Due to this value is ~20 times longer than accelerator's pulse duration, which is 240 nanoseconds, He-3 counters in modern experiment can serve only as monitors, instead of their usage during previous decades for total cross

section measurements. Cromium-53, which available in the stainless steel alloy of the RADEX proton beam target, defines in Fig.15 nonlinear behavior of the neutron flux between 2400 eV (manganese-55 resonance) and 10 keV. Powerful, designed for ~1 MW average power, proton beam targets contain big thickness of multi-isotope substance along the way of neutrons.

4. Holmium-165 capture cross section in the region of first 100 histogram channels

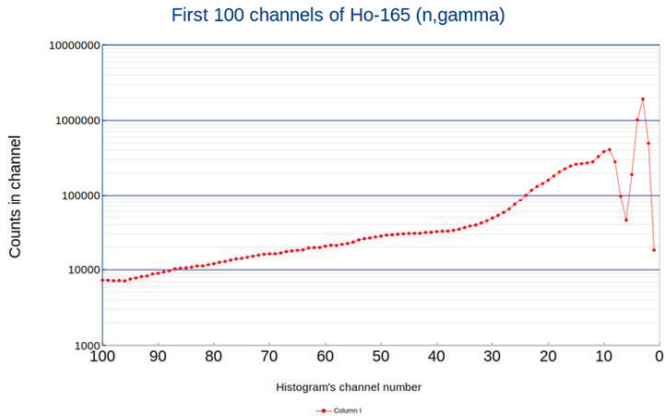

Fig.16. First 100 histogram channels in logarithmic scale.

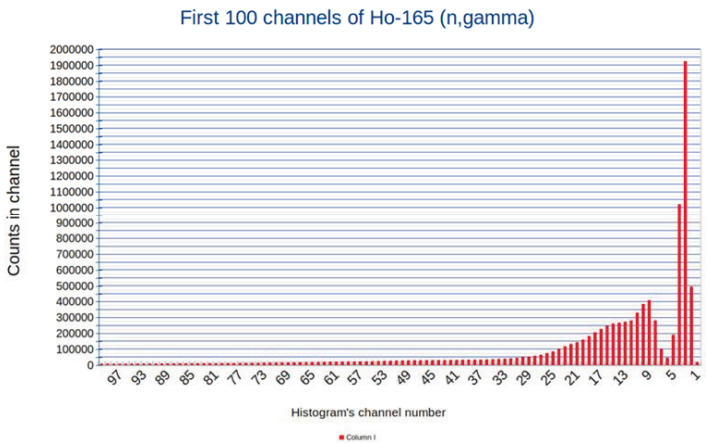

Fig.17. First 100 histogram channels in linear scale

Energy interval of Fig.16 is ABBN-93 groups numbers from 66 (~136 keV) to 1 (20 MeV) and above: up to initial proton's energy 364 MeV.

Share of cascade neutrons is appreciated around 8%. In Fig.17 we observe exact separation between tungsten target's gamma-flash in first five channels, and neutrons in channels after number 6. Form of the curve in channels from 6 to 12 shows, that 6 nsec/meter and 50 meters aren't enough to separation between cascade and spallation neutrons. It is observable that spallation neutrons are born mainly in energy region above 31st ABBN-93 energy group, i.e. above 2 MeV. This energy area is much higher, than the case of fissile neutrons, which are available above 136 keV i.e. above 67th ABBN-93 group.

On logarithmic curve of Fig.16 we can see traces of the resonance structure around 96th histogram channel (~150 keV) and above. Energy resolution 6 nsec/meter turns out enough to detect wide resonances even at this high energy. However, implemented gamma detector hasn't high 'effect divided to background' ratio around 100 keV, where main part of spectra of fast breeder reactors is situated. Currently new gamma-detector, designed for high energy region, is under construction.

A separate paper will be devoted to data processing. This includes extracting resonance parameters: in the form of Breit-Wigner approach and in the IAEA-used form of 'R-matrix'. Also includes calculating neutron group constants using experimental histogram. Preliminary results are close to the ABBN-93 data within the statistical range.

For calculation of measuring performance of the TOF spectrometer INES in each of 299 ABBN-93 energy groups, due to significant quantity of calculations, during work on this paper we wrote a computer program which calculates, in particular, number of experimental histogram's channels which fit into each of 299 groups. This performance is shown below in Table 1. Number of histogram channels per one ABBN-93 group, multiplied with number of experimental detector's counts per one histogram channel at any chosen neutron energy, results that statistics per one ABBN-93 energy group is found enough to extract group capture cross sections.

Measurements of group constants are sometimes called 'measurements in wide groups'. So as one energy group can contain several cross sections resonances. At the same time Table 1 shows, that 'wide groups' really aren't very wide: small number of the data acquisition channels per one ABBN-93 energy group in upper energy part. For measurements in high energy area, it's necessary to have perfect energy resolution of the TOF spectrometer: short nanosecond neutron pulses simultaneously with long TOF bases, which means large measurement time to accumulate enough statistics per ABBN-93 energy group, for each of 286 stable isotopes available in nature. Also necessary to note, that data processing requires to have measurements on several different pattern thicknesses for each isotope.

Table 1: Number of data acquisition channels per one ABBN-93 energy group

ABBN-93 Group №	Upper Energy border, eV	Low Energy border, eV	Channels per group	ABBN-93 Group №	Upper Energy border, eV	Low Energy border, eV	Channels per group
1	20000000	18618200	0.29133718	**8**	12116500	11279300	0.37433566
2	18618200	17331800	0.30197188	**9**	11279300	10500000	0.38795163
3	17331800	16134300	0.31297285	**10**	10500000	9693420	0.44983895
4	16134300	15019500	0.32439133	**11**	9693420	8948790	0.46818648
5	15019500	13981800	0.33618969	**12**	8948790	8261360	0.48727703
6	13981800	13015800	0.34844012	**13**	8261360	7626740	0.50714277
7	13015800	12116500	0.36115617	**14**	7626740	7040870	0.527821

Table 1: Number of data acquisition channels per one ABBN-93 energy group

ABBN-93 Group №	Upper Energy border, eV	Low Energy border, eV	Channels per group	ABBN-93 Group №	Upper Energy border, eV	Low Energy border, eV	Channels per group
15	7040870	6500000	0.54934791	**52**	432024	400000	2.1353311
16	6500000	5994750	0.57896217	**53**	400000	370350	2.21914665
17	5994750	5528770	0.60287153	**54**	370350	342898	2.306251
18	5528770	5099020	0.62774989	**55**	342898	317480	2.39687805
19	5099020	4702670	0.65367616	**56**	317480	293947	2.4908857
20	4702670	4337130	0.68066261	**57**	293947	272158	2.588721
21	4337130	4000000	0.70877398	**58**	272158	251984	2.69037
22	4000000	3698620	0.71400693	**59**	251984	233306	2.7959009
23	3698620	3419950	0.74252039	**60**	233306	216012	2.9057495
24	3419950	3162280	0.77216762	**61**	216012	200000	3.01981425
25	3162280	2924020	0.8030238	**62**	200000	185175	3.13834725
26	2924020	2703710	0.8351061	**63**	185175	171449	3.2615314
27	2703710	2500000	0.86846043	**64**	171449	158740	3.3896974
28	2500000	2325220	0.83437917	**65**	158740	146973	3.522803
29	2325220	2162650	0.86522179	**66**	146973	136079	3.66084575
30	2162650	2011460	0.89706643	**67**	136079	125992	3.8047578
31	2011460	1870830	0.93023666	**68**	125992	116653	3.954001
32	1870830	1740030	0.9645821	**69**	116653	108006	4.1093503
33	1740030	1618380	1.00013575	**70**	108006	100000	4.2706622
34	1618380	1505240	1.03699401	**71**	100000	93804,2	3.6738483
35	1505240	1400000	1.07536344	**72**	93804.2	87992,3	3.7932236
36	1400000	1305410	1.07552034	**73**	87992.3	82540,4	3.9165618
37	1305410	1217220	1.11368401	**74**	82540.4	77426,4	4.0437522
38	1217220	1134980	1.15343937	**75**	77426.4	72629,2	4.1752079
39	1134980	1058300	1.19443907	**76**	72629.2	68129,2	4.3109167
40	1058300	986800	1.23696449	**77**	68129.2	63908	4.4510255
41	986800	920131	1.2809863	**78**	63908	59948,4	4.5956
42	920131	857965	1.32660961	**79**	59948.4	56234,1	4.7449813
43	857965	800000	1.37380729	**80**	56234.1	52750	4.8990795
44	800000	740700	1.56917362	**81**	52750	49481,7	5.058388
45	740700	685795	1.6307972	**82**	49481.7	46415,9	5.2227688
46	685795	634960	1.69481723	**83**	46415.9	43540	5.3925964
47	634960	587894	1.76132216	**84**	43540	40842,4	5.5676038
48	587894	544316	1.83050219	**85**	40842.4	38311,9	5.7486143
49	544316	503968	1.9023789	**86**	38311.9	35938,1	5.9356468
50	503968	466612	1.9770005	**87**	35938.1	33711,5	6.1281988
51	466612	432024	2.05467515	**88**	33711.5	31622,8	6.3275094

Table 1: Number of data acquisition channels per one ABBN-93 energy group

ABBN-93 Group №	Upper Energy border, eV	Low Energy border, eV	Channels per group	ABBN-93 Group №	Upper Energy border, eV	Low Energy border, eV	Channels per group
89	31622.8	29663.5	6.5331771	**128**	2610.16	2448.44	22.739809
90	29663.5	27825.6	6.74547	**129**	2448.44	2296.74	23.478759
91	27825.6	26101.6	6.9645657	**130**	2296.74	2154.43	24.243358
92	26101.6	24484.4	7.1909591	**131**	2154.43	2020.95	25.0288425
93	24484.4	22967.4	7.4246354	**132**	2020.95	1895.74	25.842159
94	22967.4	21544.3	7.6664231	**133**	1895.74	1778.28	26.6837175
95	21544.3	20209.5	7.9148149	**134**	1778.28	1668.1	27.550319
96	20209.5	18957.4	8.1720082	**135**	1668.1	1564.75	28.444659
97	18957.4	17782.8	8.4381325	**136**	1564.75	1467.8	29.370035
98	17782.8	16681	8.7121757	**137**	1467.8	1376.86	30.3234065
99	16681	15647.5	8.9949911	**138**	1376.86	1291.55	31.3104785
100	15647.5	14678	9.2876205	**139**	1291.55	1211.53	32.326228
101	14678	13768.6	9.5891028	**140**	1211.53	1136.46	33.380336
102	13768.6	12915.5	9.901243	**141**	1136.46	1066.05	34.460857
103	12915.5	12115.3	10.2224509	**142**	1066.05	1000	35.581985
104	12115.3	11364.6	10.555789	**143**	1000	938.042	36.738483
105	11364.6	10660.5	10.8974801	**144**	938.042	879.923	37.932236
106	10660.5	10000	11.2520115	**145**	879.923	825.404	39.165618
107	10000	9380.42	11.6177283	**146**	825.404	774.264	40.437522
108	9380.42	8799.23	11.9952264	**147**	774.264	726.292	41.752079
109	8799.23	8254.04	12.3852558	**148**	726.292	681.292	43.109167
110	8254.04	7742.64	12.7874668	**149**	681.292	639.08	44.510254
111	7742.64	7262.92	13.2031671	**150**	639.08	599.484	45.956001
112	7262.92	6812.92	13.6323155	**151**	599.484	562.341	47.449813
113	6812.92	6390.8	14.0753781	**152**	562.341	527.5	48.990794
114	6390.8	5994.84	14.5325638	**153**	527.5	494.817	50.583881
115	5994.84	5623.41	15.0049481	**154**	494.817	464.159	52.227688
116	5623.41	5275	15.4922495	**155**	464.159	435.4	53.925963
117	5275	4948.17	15.9960276	**156**	435.4	408.424	55.676039
118	4948.17	4641.59	16.515845	**157**	408.424	383.119	57.486143
119	4641.59	4354	17.052887	**158**	383.119	359.381	59.356468
120	4354	4084.24	17.6063095	**159**	359.381	337.115	61.281988
121	4084.24	3831.19	18.178714	**160**	337.115	316.228	63.275094
122	3831.19	3593.81	18.7701635	**161**	316.228	296.635	65.331771
123	3593.81	3371.15	19.3790665	**162**	296.635	278.256	67.4547
124	3371.15	3162.28	20.0093415	**163**	278.256	261.016	69.645657
125	3162.28	2966.35	20.65972	**164**	261.016	244.844	71.909591
126	2966.35	2782.56	21.331049	**165**	244.844	229.674	74.246354
127	2782.56	2610.16	22.023891	**166**	229.674	215.443	76.664231

Table 1: Number of data acquisition channels per one ABBN-93 energy group

ABBN-93 Group №	Upper Energy border, eV	Low Energy border, eV	Channels per group	ABBN-93 Group №	Upper Energy border, eV	Low Energy border, eV	Channels per group
167	215.443	202.095	79.148149	**206**	17.7828	16.681	275.50319
168	202.095	189.574	81.720082	**207**	16.681	15.6475	284.44659
169	189.574	177.828	84.381325	**208**	15.6475	14.678	293.70035
170	177.828	166.81	87.121757	**209**	14.678	13.7686	303.234065
171	166.81	156.475	89.949911	**210**	13.7686	12.9155	313.104785
172	156.475	146.78	92.876204	**211**	12.9155	12.1153	323.26228
173	146.78	137.686	95.891029	**212**	12.1153	11.3646	333.80336
174	137.686	129.155	99.01243	**213**	11.3646	10.6605	344.60857
175	129.155	121.153	102.224509	**214**	10.6605	10	355.81985
176	121.153	113.646	105.55789	**215**	10	9.38042	367.38483
177	113.646	106.605	108.974801	**216**	9.38042	8.79923	379.32236
178	106.605	100	112.520115	**217**	8.79923	8.25404	391.65618
179	100	93.8042	116.177283	**218**	8.25404	7.74264	404.37522
180	93.8042	87.9923	119.952264	**219**	7.74264	7.26292	417.52079
181	87.9923	82.5404	123.852558	**220**	7.26292	6.81292	431.09167
182	82.5404	77.4264	127.874668	**221**	6.81292	6.3908	445.10254
183	77.4264	72.6292	132.031671	**222**	6.3908	5.99484	459.56001
184	72.6292	68.1292	136.323155	**223**	5.99484	5.62341	474.49813
185	68.1292	63.908	140.753781	**224**	5.62341	5.275	489.90794
186	63.908	59.9484	145.325638	**225**	5.275	4.94817	505.83881
187	59.9484	56.2341	150.049481	**226**	4.94817	4.64159	522.27688
188	56.2341	52.75	154.922497	**227**	4.64159	4.354	539.25963
189	52.75	49.4817	159.960274	**228**	4.354	4.08424	556.76039
190	49.4817	46.4159	165.15845	**229**	4.08424	3.83119	574.86143
191	46.4159	43.54	170.52887	**230**	3.83119	3.59381	593.56468
192	43.54	40.8424	176.063095	**231**	3.59381	3.37115	612.81988
193	40.8424	38.3119	181.78714	**232**	3.37115	3.16228	632.75094
194	38.3119	35.9381	187.701635	**233**	3.16228	2.96635	653.31771
195	35.9381	33.7115	193.790665	**234**	2.96635	2.78256	674.547
196	33.7115	31.6228	200.093415	**235**	2.78256	2.61016	696.45657
197	31.6228	29.6635	206.5972	**236**	2.61016	2.44844	719.09591
198	29.6635	27.8256	213.31049	**237**	2.44844	2.29674	742.46354
199	27.8256	26.1016	220.23891	**238**	2.29674	2.15443	766.64231
200	26.1016	24.4844	227.39809	**239**	2.15443	2.02095	791.48149
201	24.4844	22.9674	234.78759	**240**	2.02095	1.89574	817.20082
202	22.9674	21.5443	242.43358	**241**	1.89574	1.77828	843.81325
203	21.5443	20.2095	250.288425	**242**	1.77828	1.6681	871.21757
204	20,2095	18.9574	258.42159	**243**	1.6681	1.56475	928.76204
205	18,9574	17.7828	266.837175	**244**	1.56475	1.4678	958.91029

Table 1: Number of data acquisition channels per one ABBN-93 energy group

ABBN-93 Group №	Upper Energy border, eV	Low Energy border, eV	Channels per group	ABBN-93 Group №	Upper Energy border, eV	Low Energy border, eV	Channels per group
245	1.4678	1.37686	990.1243	**255**	0.774264	0.726292	1363.23155
246	1.37686	1.29155	1022.24509	**256**	0.726292	0.681292	1407.53781
247	1.29155	1.21153	1055.5789	**257**	0.681292	0.63908	1453.25638
248	1.21153	1.13646	1089.74801	**258**	0.63908	0.599484	1500.49481
249	1.13646	1.06605	1125.20115	**259**	0.599484	0.562341	1549.22497
250	1.06605	1	1161.77283	**260**	0.562341	0.5275	1599.60274
251	1	0.938042	1199.52264	**261**	0.5275	0.494817	1651.5845
252	0.938042	0.879923	1238.52558	**262**	0.494817	0.464159	1705.2887
253	0.879923	0.825404	1278.74668	**263**	0.464159	0.4354	1760.63095
254	0.825404	0.774264	1320.31671	**264**	0.4354	0.408424	1817.8714

Conclusion

For isotope holmium-165, world databases contain capture cross sections data with resolved resonances area below upper energy border 1250 eV. The same value has performance of the INES TOF spectrometer, based on the spallation neutron source RADEX of the Moscow linear proton accelerator of the Russian Academy of Sciences.

Necessary to note that advantages of 299-group calculations. Energy width of each group in 299-group approach corresponds to elastic scattering of neutrons on sodium ^{23}Na. While previous multi-year Rosatom's standard ABBN-78, which had 28 energy groups, corresponds to moderation on deuterium D2. Comparing of the 299-group approach of the SHIELD program, and MCNPX which instead of energy groups uses continuous curves of cross sections, shows that exist several practical advantages of 299-group approach:

1. Due to availability of various light nuclides in the volume, 299 groups are enough for majority of reactor tasks and radiation shield tasks.

2. Modern available in ENDF/B-VIII cross sections of plenty isotopes still have value of the upper energy border of resolved resonances much less, than energy, where Doppler effect physically mixes neighbor resonances. Energy region of unresolved resonances in nuclear data for plenty isotopes still exists.

3. For total cross section of freshly measured isotopes, such as ^{238}U, the best available curve consists of about 8000 points. In the case of values such as 8,000 energy groups and more, for precision value 0.2% in each energy interval, calculation must be done using multi-processor computer (1000 processors and more). This requires both to have access to significant machine time of such computer, and that program code must be re-written for compatibility with multi-processor mode.

4. At the same time: with statistics 100,000,000 neutrons for each variant calculation, performance of the 299-group version of the SHIELD program allows to calculate enough quantity of variants per year, using several modern personal computers. Available statistics provides discreteness calculation precision component better than value of delayed neutron's share, which is around 0.42% for fast breeder reactors such as BN-1200.

Literature

1. Brookhaven National Laboratory http://www.bnl.gov
2. Stavissky Yu.Ya. Neutron Research based on Moscow Meson Factory. In: 'Program of experimental research at Meson Factory INR RAS', volume 4, Moscow, 1986, p.7−21.
3. Djilkibaev R.M., Khliustin D.V. TOF Method Measurements of Neutron Cross Sections in 299 Energy Intervals of the ABBN-93 Group Constants. ISINN-29, Dubna, 2023.
4. Djilkibaev R.M., Khliustin D.V. Capture Neutron Cross Sections Measurements of Rare Earth Isotopes. ISINN-28, May 24-28, 2021.
5. http://isinn.jinr.ru/past-isinns/isinn-27/presentations/12/Khliustin.pdf
6. http://isinn.jinr.ru/past-isinns/isinn-26/0601PM_session%20A/A19.pdf
7. http://isinn.jinr.ru/past-isinns/isinn-25/24/Hliustin.pdf
8. http://isinn.jinr.ru/past-isinns/isinn-24/3_day/hlustin.pdf
9. http://isinn.jinr.ru/past-isinns/isinn-21/progr-23_05_2013/Hliustin.pdf
10. Л.П. Абагян, Н.О. Базянц, М.Н. Николаев, А.М. Цибуля, Групповые константы для расчёта реакторов и защиты. Справочник. Москва, Энергоатомиздат, 1981.
11. Manturov G.N., Nikolayev M.N., Tsibulya A.M. System of group constants ABBN-93. Part 1. Nuclear constants for calculation of neutron and photon fields of emission. VANT, 'Nuclear Constants', №1, 1996, p.59−98.

Investigation of Low-Energy p-Wave Resonance of ^{35}Cl Nucleus at the IREN Facility

V.L. Kuznetsov[1,2], E.A. Golubkov[1], Yu.N. Kopatch[1], L.V. Mitsyna[1], N.V. Rebrova[1], A.D. Rogov[1], P.V. Sedyshev[1], A. Yergashov[3]

[1]*Frank Laboratory of Neutron Physics, Joint Institute for Nuclear Research, Dubna, Russia*
[2]*Institute for Nuclear Research of the Russian Academy of Sciences, Moscow, 117312, Russia*
[3]*L.N. Gumilyov Eurasian National University, Astana, Republic of Kazakhstan*

The angular anisotropy of γ-quanta of a defined energy emitted in the ^{35}Cl(n,γ)^{36}Cl reaction near the 398 eV p-wave resonance of ^{35}Cl has been investigated. The partial neutron widths, $\Gamma^n_{p,j=1/2}$ and $\Gamma^n_{p,j=3/2}$, have been determined for the total angular momenta of the incident neutron $j = 1/2$ and $j = 3/2$ within the Flambaum–Sushkov formalism. The measurements were carried out at the IREN facility [1, 2], the resonance-neutron source in Dubna.

I. INTRODUCTION

The experimental determination of partial neutron widths of low-lying p-wave resonances in (n,γ) reactions started at the Frank Laboratory of Neutron Physics of the Joint Institute for Nuclear Research (FLNP JINR) in 1981 [3] at the IBR-30 reactor and ended in 1991 [4]. These investigations are of current importance for studying the violation of time invariance and parity violation in neutron–nucleus interactions. An additional significance is the experimental measurement of the $\Gamma^n_{p,j=1/2}$ and $\Gamma^n_{p,j=3/2}$ neutron widths of the p-wave resonance that can be excited with two entry channels (the total angular momentum of the incident neutron can be $j = 1/2$ or $j = 3/2$). Recently, several papers have been published by Japanese scientists [5–8], in which p-wave resonances of (n,γ) reactions were studied using the ^{139}La, ^{81}Br, and ^{117}Sn nuclei in order to determine the partial neutron widths.

Currently, partial neutron widths of p-wave resonance are evaluated on the basis of the theoretical expressions by V.V. Flambaum and O.P. Sushkov from [9] in which the $\Gamma^n_{p,j=1/2}$ and $\Gamma^n_{p,j=3/2}$ values are included in the reaction amplitudes as the ratios $x = \sqrt{\Gamma_{p,j=1/2}/(\Gamma_{p,j=1/2} + \Gamma_{p,j=3/2})}$ and $y = \sqrt{\Gamma_{p,j=3/2}/(\Gamma_{p,j=1/2} + \Gamma_{p,j=3/2})}$, $x^2 + y^2 = 1$. Strictly speaking, to obtain the parameters of the neutron–nucleus interaction potential, it is necessary to perform numerous experiments with polarized neutrons and to analyze the polarization of reaction products, as well as to conduct a phase analysis. However, measuring angular distribution of reaction products promotes the determination of neutron p-wave resonance partial widths.

In studies of neutron resonance at low energies, the number of neutron orbital moments can be limited ($l \leq 2$). So, in the Legendre $P_l(cos\theta)$ polynomial expansion of a differential cross-section of the reaction, among the amplitudes of neutron–nucleus interactions defined in [9], in the case of the radiative capture of the unpolarized neutron by the unpolarized nucleus, a_0, a_1 with $P_1(cos\theta) = cos\theta$, and a_3 with $P_2(cos\theta) = (3cos^2\theta - 1)/2)$ are only significant:

$$\frac{d\,\sigma(\mathbf{n}_\gamma)}{d\,\Omega} = \frac{1}{2}\left[a_0 + a_1(\mathbf{n}_n\mathbf{n}_\gamma) + a_3\left((\mathbf{n}_n\mathbf{n}_\gamma)^2 - \frac{1}{3}\right)\right] =$$

$$= \frac{1}{2}\left[a_0 + a_1\cos\theta_\gamma + a_3\left(\cos^2\theta_\gamma - \frac{1}{3}\right)\right]. \quad (1)$$

Here, a_1 is the coefficient of forward-backward asymmetry of γ-emission, a_3 is the cross-section anisotropy coefficient, θ is the angle between the unit vectors of momenta of the neutron and γ-quantum, $\mathbf{n}_n$ and $\mathbf{n}_\gamma$, correspondingly.

Applying the interpretation of Japanese scientists from [5] within the Flambaum–Sushkov formalism, the required amplitudes can be expressed in terms of known resonance parameters of the reaction with the investigated nucleus.

For the incident neutron energy, E_n, in the ^{35}Cl(n,γ)^{36}Cl reaction , the coefficients a_0, a_1, and a_3 in the two-level approximation are:

$$a_0 = \lambda_s^2\sqrt{\frac{|E_s|}{E_n}}\frac{\Gamma_s^2/4}{(\mathrm{E}_n - \mathrm{E}_s)^2 + \Gamma_s^2/4} + \lambda_p^2\sqrt{\frac{E_n}{E_p}}\frac{\Gamma_p^2/4}{\left(\mathrm{E}_n - \mathrm{E}_p\right)^2 + \Gamma_p^2/4}, \quad (2)$$

for spin $J_f = 1$ of the final state of γ-transition in the ^{36}Cl nucleus:

$$a_1 = \lambda_s\lambda_p\left(\frac{|E_s|}{E_p}\right)^{\frac{1}{4}}\frac{\Gamma_s\Gamma_p\left((E_n - E_s)(E_n - E_p) + \Gamma_s\Gamma_p/4\right)}{[(\mathrm{E}_n - \mathrm{E}_s)^2 + \Gamma_s^2/4]\left[\left(\mathrm{E}_n - \mathrm{E}_p\right)^2 + \Gamma_p^2/4\right]}(-0.75x + 0.75y), \quad (3)$$

$$a_3 = \lambda_p^2\sqrt{\frac{E_n}{E_p}}\frac{\Gamma_p^2/4}{\left(\mathrm{E}_n - \mathrm{E}_p\right)^2 + \Gamma_p^2/4}3\sqrt{10}(-0.11xy), \quad (4)$$

for $J_f = 2$ of the final state of γ-transition:

$$a_1 = \lambda_s\lambda_p\left(\frac{|E_s|}{E_p}\right)^{\frac{1}{4}}\frac{\Gamma_s\Gamma_p\left((E_n - E_s)(E_n - E_p) + \Gamma_s\Gamma_p/4\right)}{[(\mathrm{E}_n - \mathrm{E}_s)^2 + \Gamma_s^2/4]\left[\left(\mathrm{E}_n - \mathrm{E}_p\right)^2 + \Gamma_p^2/4\right]}(-0.25x + 0.25y), \quad (5)$$

$$a_3 = \lambda_p^2\sqrt{\frac{E_n}{E_p}}\frac{\Gamma_p^2/4}{\left(\mathrm{E}_n - \mathrm{E}_p\right)^2 + \Gamma_p^2/4}3\sqrt{10}(0.11xy), \quad (6)$$

and for $J_f = 3$ of the final state:

$$a_1 = \lambda_s\lambda_p\left(\frac{|E_s|}{E_p}\right)^{\frac{1}{4}}\frac{\Gamma_s\Gamma_p\left((E_n - E_s)(E_n - E_p) + \Gamma_s\Gamma_p/4\right)}{[(\mathrm{E}_n - \mathrm{E}_s)^2 + \Gamma_s^2/4]\left[\left(\mathrm{E}_n - \mathrm{E}_p\right)^2 + \Gamma_p^2/4\right]}(0.5x - 0.5y), \quad (7)$$

$$a_3 = \lambda_p^2\sqrt{\frac{E_n}{E_p}}\frac{\Gamma_p^2/4}{\left(\mathrm{E}_n - \mathrm{E}_p\right)^2 + \Gamma_p^2/4}3\sqrt{10}(-0.032xy), \quad (8)$$

where E_s, E_p (or $E_{s,p}$) are the energies of the nearest s-wave resonance and p-wave resonance under study; $\lambda_{s,p} = \hbar/2\sqrt{\left(2g\Gamma_{s,p}^n\,\Gamma_{s,p}^\gamma\right)/\left(m_n|E_{s,p}|\Gamma_{s,p}^2\right)}$, $g = \frac{(2J_{s,p}+1)}{2(2I+1)}$; Γ_s, Γ_p (or $\Gamma_{s,p}$) are the

total widths of these resonances; the $\Gamma^{\gamma}_{s,p}$ values are their total radiative widths; I is the spin of the target nucleus; $J_{s,p}$ are the angular momenta of the compound resonances.

As the p-wave resonance of the ^{35}Cl nucleus at the $E_p = 398$ eV was investigated and the negative s-wave resonance at $E_s = -181$ eV is the nearest to the resonance under study, $I = 3/2$ and $J_{s,p} = 2$. Figure 1 demonstrates the behaviour of the correlation coefficients a_1 and a_3 in the reaction ^{35}Cl(n,γ)^{36}Cl as a function of the energy of the captured neutron. The calculations are performed using formulas (7) and (8). The reaction amplitudes x and y are assumed to be 0.71 and −0.71, respectively, and the spin of the final state of γ-transition 3 is considered.

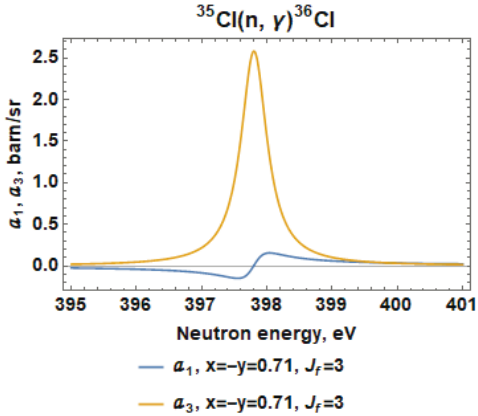

Fig. 1. The correlation coefficients a_1 and a_3 dependence on the energy of captured neutrons near the 398 eV chlorine resonance.

The violation of spatial parity was already observed in chlorine upon capture of polarized slow neutrons in the (n,γ) reaction [10−13] and in the (n,p) reaction [14, 15].

In the work [16] the angular correlations in γ-quanta emission near the 398 eV p-wave resonance were studied, and it was found that in the channel spin representation the predominant channel spin component in ^{35}Cl(n,γ)^{36}Cl is 2. In the representation of the total angular momentum of the neutron, this corresponds to the dominance of $j = 3/2$. Later in [17], the forward-backward correlation in the ^{35}Cl(n,p)^{35}S reaction was measured using unpolarized resonance neutrons. With the experimental results of [18], the possible values of neutron and proton amplitudes were analyzed for the channels with the total momenta $j = 1/2$ and $j = 3/2$. However, the experimental precision of [17] was insufficient for a definitive selection of the solution related to reaction amplitudes.

II. EXPERIMENT AND DATA ANALYSIS

To extract partial neutron widths from angular distributions of γ-quanta, the 398 eV p-wave resonance in the ^{35}Cl(n,γ)^{36}Cl reaction was studied using a $CaCl_2$ target at the 11-meter flight path of the IREN facility. Calcium–chloride powder was poured into the disk-shaped 3-cm-thick aluminum container measuring 8 cm in diameter, which approximately corresponds to the mean free path of the neutron at the energies near the investigated

resonance of ^{35}Cl. The γ-quanta emitted from the target were recorded by BGO detectors whose sensitive element is the bismuth germinate crystal ($Bi_4Ge_3O_{12}$). The detectors had a resolution of ~200 keV at 6.6 MeV. The detectors were located 20 cm from the sample.

During several series of measurements, γ-quanta emission was recorded at the angles $\theta = 55°, 90°, 125°, 235°, 270°$, and $305°$ relative to the neutron beam direction. Figure 2 shows the γ-quanta yield spectrum as a function of the captured neutron energy recorded by the detector positioned at 55 degrees (the measuring time was 27 hours).

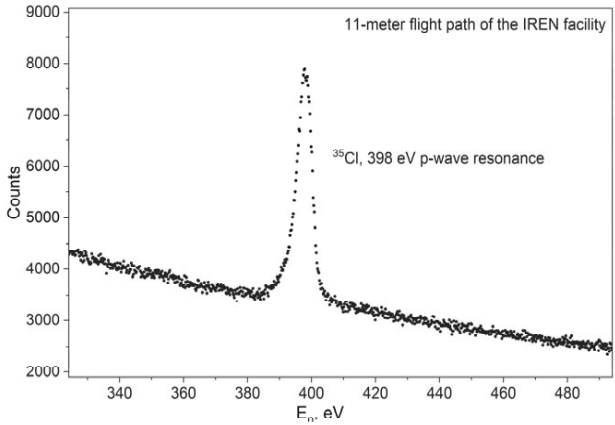

Fig. 2. Yield of γ-quanta from the ^{35}Cl(n,γ)^{36}Cl reaction near the 398 eV neutron p-wave resonance of ^{35}Cl depending on neutron energy. The $CaCl_2$ sample was measured during 27 hours by the detector positioned at 55 degrees.

For the analysis of angular distributions of γ-emission of the compound-nucleus decay in the amplitude spectra of each of the series, three noticeable peaks were chosen which corresponded to the primary γ-transitions with the energies of 5715, 6111, 6620 and 6628 keV. Figures 3 and 4 exhibit the integral spectrum of γ-quanta amplitudes registered in the full range of neutron detection and the spectrum of amplitudes of γ-quanta emitted during neutron capture in chlorine resonance (393 – 402 eV). The background spectrum, which is shown in Fig. 4, was derived from the interval (380 – 389 eV) lying to the left of the resonance.

In February 2025, three series of measurements were carried out with the $CaCl_2$ sample. Their measuring times were 27, 28 and 53 hours. In each series of measurements, the correlation coefficients a_1 and a_3 were determined, and a weighted average was found. Due to insufficient statistics and complicated background conditions, we did not succeed in obtaining the coefficient a_1 of forward-backward asymmetry of γ-quanta emission at the 11-meter flight path of the IREN facility. However, we determined a sign of a_1 near the 398 eV chlorine resonance. And the measurements suggested that the a_3 coefficient could be obtained.

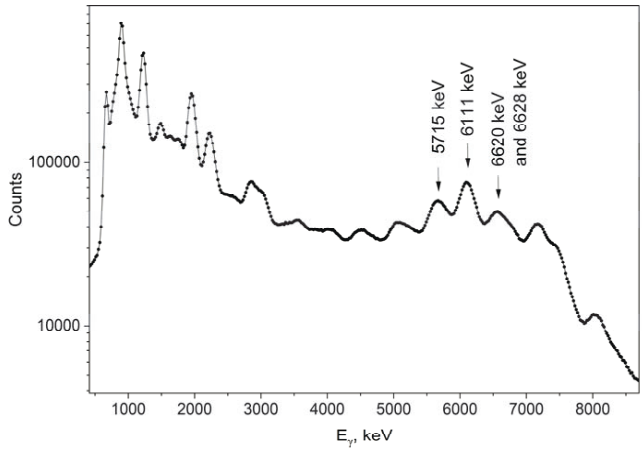

Fig. 3. Integral spectrum of γ-quanta amplitudes from the $^{35}Cl(n,\gamma)^{36}Cl$ reaction measured by the detector positioned at 55 degrees during 27 hours.

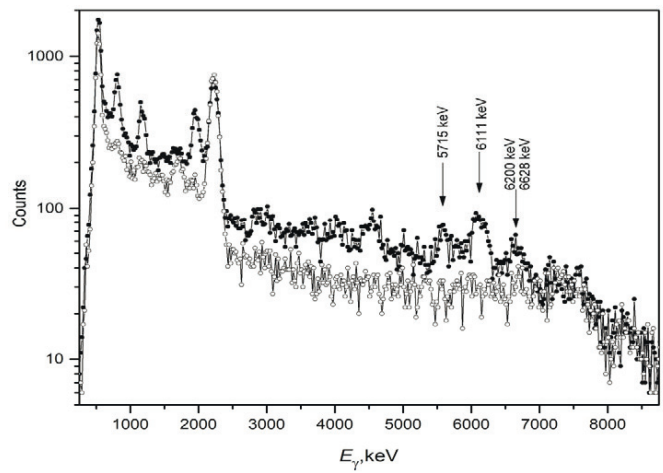

Fig. 4. Spectrum of γ-quanta amplitudes from the $^{35}Cl(n,\gamma)^{36}Cl$ reaction in the resonance (line with black points) and the background spectrum out of the resonance(line with open points) measured by the detector positioned at 55 degrees during 27 hours.

As the nearest negative s-wave resonance of the ^{35}Cl nucleus (at –181 eV) located too far from the investigated p-wave resonance, so the equations (2), (4), (6), (8) can be simplified. For the considered transitions with $J_f = 3$ (or 2) [19], we can present these coefficients and a_3/a_0 ratios near the 398 eV resonance as written below:

$$a_0 \approx \lambda_p^2 \sqrt{\frac{E_n}{E_p}} \frac{\Gamma_p^2/4}{\left(\mathrm{E}_n - \mathrm{E}_p\right)^2 + \frac{\Gamma_p^2}{4}} \quad (9),$$

for 5715 keV $\left(J_f = 2\right)$: $$a_3 = \lambda_p^2 \sqrt{\frac{E_n}{E_p}} \frac{\Gamma_p^2/4}{\left(\mathrm{E}_n - \mathrm{E}_p\right)^2 + \frac{\Gamma_p^2}{4}} 3\sqrt{10}(0.11xy)$$

$$\frac{a_3}{a_0} \approx 3\sqrt{10}(0.11xy), \quad (10)$$

for 5715 keV $\left(J_f = 3\right)$: $$a_3 = \lambda_p^2 \sqrt{\frac{E_n}{E_p}} \frac{\Gamma_p^2/4}{\left(\mathrm{E}_n - \mathrm{E}_p\right)^2 + \frac{\Gamma_p^2}{4}} 3\sqrt{10}(-0.032xy),$$

$$\frac{a_3}{a_0} \approx 3\sqrt{10}(-0.032xy), \quad (11)$$

for 6111 keV $\left(J_f = 3\right)$: $$a_3 = \lambda_p^2 \sqrt{\frac{E_n}{E_p}} \frac{\Gamma_p^2/4}{\left(\mathrm{E}_n - \mathrm{E}_p\right)^2 + \frac{\Gamma_p^2}{4}} 3\sqrt{10}(-0.032xy),$$

$$\frac{a_3}{a_0} \approx 3\sqrt{10}(-0.032xy), \quad (12)$$

for 6620 $\left(J_f = 2\right)$ keV: $$a_3 = \lambda_p^2 \sqrt{\frac{E_n}{E_p}} \frac{\Gamma_p^2/4}{\left(\mathrm{E}_n - \mathrm{E}_p\right)^2 + \Gamma_p^2/4} 3\sqrt{10}(0.11xy),$$

$$\frac{a_3}{a_0} \approx 3\sqrt{10}(0.11xy), \quad (13)$$

for 6628 $\left(J_f = 2\right)$ keV: $$a_3 = \lambda_p^2 \sqrt{\frac{E_n}{E_p}} \frac{\Gamma_p^2/4}{\left(\mathrm{E}_n - \mathrm{E}_p\right)^2 + \Gamma_p^2/4} 3\sqrt{10}(0.11xy),$$

$$\frac{a_3}{a_0} \approx 3\sqrt{10}(0.11xy). \quad (14)$$

The peaks corresponding to the 6620 and 6628 keV γ-transitions are not resolved in the amplitude spectrum. However, since these transitions occur in final states with the same spin ($J_f = 2$), they can be analyzed jointly.

For each of the analyzed γ-transitions, the energy interval was defined and fixed for summation. In each interval for each detector, the sums of counts, $\sum N_{55°}$, $\sum N_{90°}$, $\sum N_{125°}$,

$\sum N_{235°}$, $\sum N_{270°}$, and $\sum N_{305°}$, were calculated. And in the same fixed intervals of the amplitude spectra corresponded to neutron energies out of range of the investigated resonance, the sums of counts, $\sum N_{\theta}^{bg}$, were also calculated to consider the background. The accuracy of the background determination was confirmed by the absence of the hydrogen peak (area near 2223 keV in Fig. 4) after the background subtraction.

There is false anisotropy caused by an inaccurate geometric arrangement of detectors, their varying efficiency, and background influences; this anisotropy needs to be eliminated. As the existence of the anisotropy of γ-emission in the investigated p-wave resonance is expected assuming its absence at thermal neutron energies, the analogues summations, $\sum N_{\theta}^{th}$ and $\sum N_{\theta}^{bg,th}$, were done in the amplitude spectra for thermal neutrons in the intervals corresponded to the investigated γ-transitions.

Then, for each of the transitions under study, the sums of counts were calculated for two orthogonal detectors $S_{orth}^{res} = \sum N_{90°} - \sum N_{90°}^{bg} + \sum N_{270°} - \sum N_{270°}^{bg}$ and for the other four detectors $S_{ang4}^{res} = \sum N_{55°} - \sum N_{55°}^{bg} + \sum N_{125°} - \sum N_{125°}^{bg} + \sum N_{235°} - \sum N_{235°}^{bg} + \sum N_{305°} - \sum N_{305°}^{bg}$ in the energy region of the neutron resonance. And in the same way S_{orth}^{th} and S_{ang4}^{th} at the thermal neutron energies were also obtained. The required anisotropy effect of γ-emission for each of the investigated γ-transitions was determined as $a_3/a_0 = 3(1 - R_{res}/R_{th})$, where $R_{res} = 2 \cdot S_{orth}^{res}/S_{ang4}^{res}$ and $R_{th} = 2 \cdot S_{orth}^{th}/S_{ang4}^{th}$. These ratios calculated for the γ-transitions under study, their errors, as well as their weighted averages are presented in Table 1.

Table 1. Ratios R_{res}/R_{th}

№	E_{γ}, keV	R_{res}/R_{th}	σ
Measurement of 05.02.2025 (27 hours)			
1	5715	1.04	0.15
2	6111	1.03	0.13
3	6620 and 6628	1.03	0.25
Measurement of 06.02.2025 (28 hours)			
1	5715	1.04	0.14
2	6111	1.05	0.12
3	6620 and 6628	1.09	0.21
Measurement of 19.02.2025 (53 hours)			
1	5715	0.97	0.06
2	6111	0.98	0.05
3	6620 and 6628	1.04	0.10
Weighted average			
1	5715	0.99	0.03
2	6111	1.00	0.03
3	6620 and 6628	1.05	0.02

The experimental x and y values are obtained using expressions (10)–(14) in accordance with final spins of the considered transitions:

$$\text{for } 5715 \text{ keV } (J_f = 2): \quad 1 - R_{res}/R_{th} = \sqrt{10}(0.11xy), \tag{15}$$

$$\text{for } 5715 \text{ keV } (J_f = 3): \quad 1 - R_{res}/R_{th} = \sqrt{10}(-0.032xy), \tag{16}$$

for 6111 keV $(J_f = 3)$: $1 - R_{res}/R_{th} = \sqrt{10}(-0.032xy)$, (17)

for 6620 keV $(J_f = 2)$: $1 - R_{res}/R_{th} = \sqrt{10}(0.11xy)$, (18)

for 6628 keV $(J_f = 2)$: $1 - R_{res}/R_{th} = \sqrt{10}(0.11xy)$. (19)

Values of x and y were determined solving a system of two equations, one of which is (15), (16), (17), (18) or (19), and the other is $x^2 + y^2 = 1$. The results are shown in Fig. 5. Due to the uncertainty of the spin of the final state during the γ-transitions of 5715 keV in the ^{36}Cl nucleus, both solutions for spins 2 and 3 were considered. Although the statistical error in determination of the weighted average of R_{res}/R_{th} is small, the values of x and y are obtained with a considerable uncertainty for the γ-transitions with the energies 5715 and 6111 keV. This is due to the proximity of the anisotropy effect, $1 - R_{res}/R_{th}$, to zero.

The systems have four solutions due to nonlinearity of the equations included in the systems for finding x and y, and the presence of sign-indefinite quantities. To obtain one solution, it is required to analyze the a_1 correlation coefficient. In [18] the sign of a_1 near the 398 eV resonance for 6111 keV γ-transitions was determined. To the left of the resonance, the sign is positive; and to the right of it, it is negative, which corresponds to the positive value of the amplitude y and the negative value of the x amplitude. The electromagnetic amplitude of γ-transitions is assumed to be positive. Therefore, x and y values are in the second quadrant on the xy plane. Unfortunately, the coefficients of x and y in (3), (5) and (7) equations differ only by a sign, so it is impossible to choose one from the two remaining solutions. Table 2 shows the values of x and y that satisfy the condition to find the a_3 curves in the second quadrant of the xy plane. The a_3 error values are bounded by the second quadrant where they extend beyond its boundaries.

Table 2. Values of x and y with their standard deviations

E_γ, keV	J_f	Solution of equation	$x_{-\sigma_1}^{+\sigma_2}$	$y_{-\sigma_1}^{+\sigma_2}$
5715	3	1	$-0.992^{+0.128}_{-0.008}$	$0.129^{+0.375}_{-0.129}$
		2	$-0.129^{+0.129}_{-0.375}$	$0.992^{+0.008}_{-0.128}$
6111	3	1	$-0.99995^{+0.03902}_{-0.00005}$	$0.0096^{+0.2649}_{-0.0096}$
		2	$-0.0096^{+0.0096}_{-0.2649}$	$0.99995^{+0.00005}_{-0.03902}$
6620 и 6628	2	1	$-0.990^{+0.009}_{-0.006}$	$0.139^{+0.054}_{-0.053}$
		2	$-0.139^{+0.053}_{-0.054}$	$0.990^{+0.006}_{-0.009}$

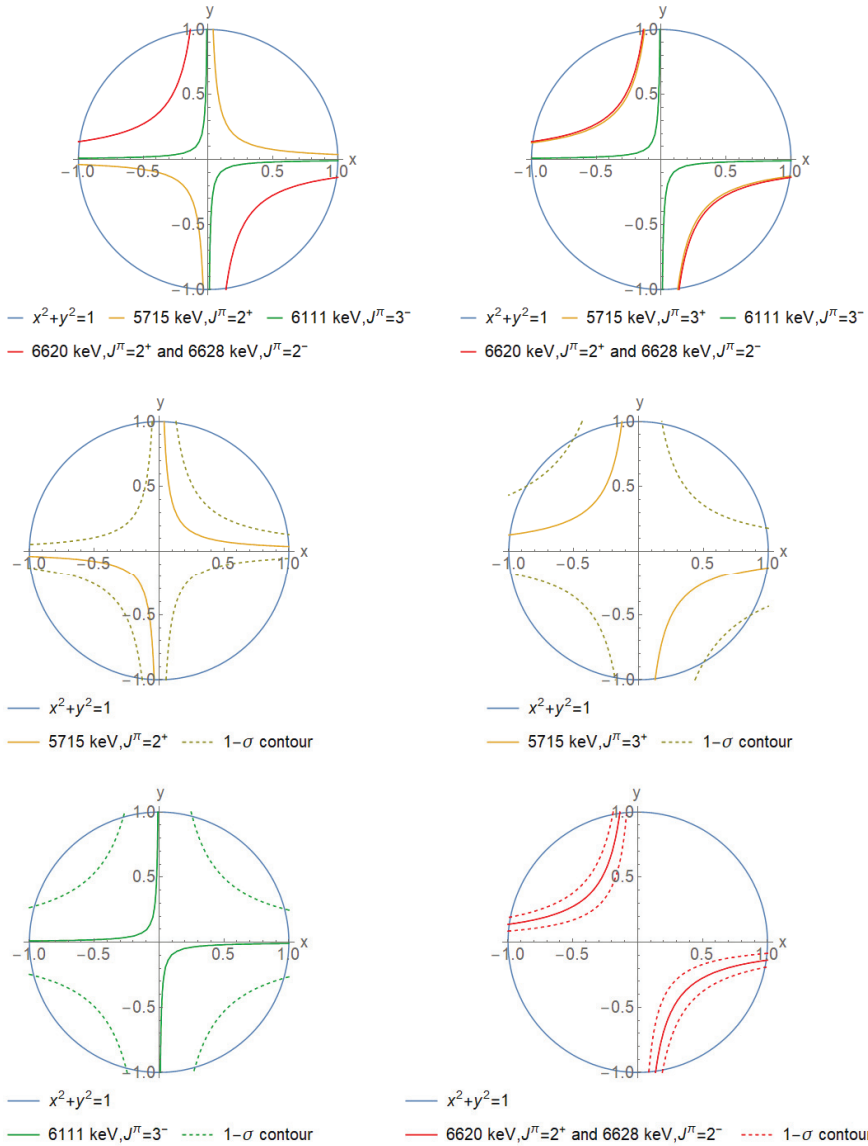

Fig. 5. Anisotropy a_3/a_0 (solid line) on the xy plane for the analyzed γ-transitions, the dashed line shows $1-\sigma$ area.

III. RESULTS

We have interpreted the experimentally obtained angular distributions of γ-quanta near the 398 eV resonance of ^{35}Cl and those from [20] as follows. The x amplitude, corresponding to the angular momentum $j = 1/2$ of the incident neutron is negative, while the y amplitude, corresponding to $j = 3/2$, is positive. One of these amplitudes is significantly stronger than another, and analyzing the coefficients a_1 and a_3 near the 398 keV chlorine resonance does not allow us to determine which is dominant. This is due to the hands-on combination of spins of the target nucleus, the compound resonance, and the spins of the final states in the ^{36}Cl during γ-emission. Our conclusion of the dominance of one of the amplitudes does not contradict those in [16] and [17].

Since all curves of a_3/a_0 describing the anisotropy of emission of primary γ-quanta upon excitation of the same state of the compound nucleus must be located, at least, in the same quadrant in the xy plane, we assume that the double-valued spin of the final state of the transition with the energy of 5715 keV in the ^{36}Cl is 3 (see the upper picture from the right in Fig.5).

ACKNOWLEDGEMENTS

We sincerely thank the staff of the IREN facility for their support, and particularly P.G. Filonchik and A.V. Andreev for our useful discussions.

References

1. A. Sumbaev, V. Kobets, V. Shvetsov, N. Dikansky, P. Logatchov. Journal of Instrumentation 15 (11) (2020).
2. Belikov O.V., et al., J. Phys. Conf. Ser. 2010. V. 205. P. 012053.
3. P. Alphimenkov et al., Pis'ma v ZhETF, 34: 308 (1981) (in Russian).
4. R. Skoy, E.I. Sharapov, PEPAN, 22(6): 1400 (1991) (in Russian).
5. T. Okudaira, S. Takada, K. Hirota et al., Phys. Rev. C, 97: 034622 (2018).
6. T. Okudaira, H.M. Shimizu, M. Kitaguchi et al., EPJ Web Conf., 219: 09001 (2019).
7. S. Endo, H.M. Shimizu, M. Kitaguchi et al., EPJ Web Conf., 219: 09003 (2019).
8. J. Koga, S. Takada, T. Yoshioka et al., EPJ Web Conf., 219: 09004 (2019).
9. V.V. Flambaum, O. P. Sushkov, Nucl. Phys. A, 435: 352 (1985).
10. V.A. Vesna et al., JETP Lett., 36: 209 (1982).
11. M. Avenier et al., Nucl. Phys. A, 436: 83 (1985).
12. G.S. Mitchell et al., Nucl. Instrum. Meth. A, 521: 468 (2004).
13. arXiv:2207.11295, retrieved 31th July 2026.
14. A. Antonov et al., JETP Lett., 40: 209 (1982).
15. Yu.M. Gledenov et al., Proceedings of the VII International Seminar on Interaction of Neutron with Nuclei (Dubna, 1999), p. 295.
16. C.M. McCullagh, M.J. Kenny and R.E. Chrien, Phys. Rev. C, 19(2): 539 (1979).
17. A. Vesna et al., Preprint of the Joint Institute for Nuclear Research, Dubna, 2002, P3-2002-175 (in Russian).
18. A. Antonov, V.A. Vesna, Yu.M. Gledenov et al., Nucl. Phys. 48(2): 305 (1988).
19. R.E. Chrien and J. Kopecky, Phys. Rev. Lett. 39(15): 911 (1977).
20. V.L. Kuznetsov et al., the Proceedings of the XXXI International Seminar on Interaction of Neutron with Nuclei (Dongguan, 2025), p. 37.

About a Possibility to Obtain the Forward-Backward Asymmetry of Gamma Emission Studying the ^{81}Br(n, γ) Reaction

V.L. Kuznetsov[1,2], L.V. Mitsyna[1], A.I. Oprea[3], C. Oprea[4], N.V. Rebrova[1], P.V. Sedyshev[1]

[1]*Frank Laboratory of Neutron Physics, Joint Institute for Nuclear Research, Dubna*
[2]*Institute for Nuclear Research of the Russian Academy of Sciences, Moscow, Russian Federation*
[3]*Technical College "Alexandru Roman", Alesd, Bihor County, Romania*
[4]*Theoretical College "Lucian Blaga", Oradea, Bihor County, Romania*

The P-even angular asymmetry measurements of emitted gammas from (n,γ) reaction at the neutron energies near low-energy p-wave resonances are continued in FLNP, JINR in order to discover $(\vec{k}_n\vec{k}_\gamma)$ and $(\vec{s}_n[\vec{k}_n\vec{k}_\gamma])$ correlations. The experimental study of the spatial asymmetry of emitted γ-quanta of radiative capture of unpolarized neutrons near two-component p-wave resonance promotes to determine its partial widths, $\Gamma^n_{p,\,j=1/2}$ and $\Gamma^n_{p,\,j=3/2}$, which is needed for theoretical interpretation of the parity violation effect.

Our decision to study the ^{81}Br(n,γ) reaction was inspired by the work of Japanese physicists [1], as they reported the result of a first measurement of the angular dependence of γ-rays emission in the reaction ^{81}Br(n,γ) near the p-wave resonance at the 0.88 eV neutron energy, using $MgBr_2$ powder with natural isotopic abundance as a target. The authors of [1] could observe γ-transitions of investigated two-component resonance and obtained an asymmetry dependence of γ-quanta on their emitted angle for 7302 keV γ-transition between the levels with I=3/2$^-$ and J=2$^-$ of ^{82}Br. In spite of its small intensity (~ 4.6%), this γ-transition was chosen in the amplitude spectrum, as "the corresponding nuclear transition is well isolated, while the majority of other transitions is suffering from background contamination due to other γ-rays".

Our experimental study of the ^{81}Br(n,γ) reaction was carried out at 11-meter flight path of the IREN facility with a liquid Br_2 target (51% ^{79}Br and 49% ^{81}Br) in a glass cylinder bottle with 1 cm in diameter and 10 cm of length and BGO scintillator detectors, sensitive element of which is bismuth germinate crystal ($Bi_4Ge_3O_{12}$).

As even at isotropic γ-emission the asymmetry of γ-detection in real geometry of the experiment inevitably exists, which is caused by a difference of solid angles of the detectors from the points of capture of neutrons and theirs energy losses with a change of the directions after scattering before capture in the target, this distorting effect had to be evaluated in order to determine a lower limit ("zero" asymmetry effect) for the required asymmetry. Thus, at the design of the experiment, "zero" effect caused by kinematics and geometry of the experiment was calculated for our Br_2 target at the energies of incident neutrons near investigated p-wave resonance of ^{81}Br. Monte Carlo calculations were done under the assumption that each captured neutron gives birth to one γ-quantum only. Capture and scattering cross sections of ^{79}Br and ^{81}Br isotopes were taken from the tables of ENDF/B data-library, where Doppler broadening was already taken into account. 10^8 neutrons were played per each incident-neutron energy point. Multiple scattering of neutrons in the target of given sizes and composition was taken into account.

As is shown in (*x*-*z*) plane view of scheme for calculation (Fig.1), four detectors were placed around the bromine sample angularly forward and backward relative to the neutron beam. The cylinder bottle with bromine was placed into the neutron beam vertically. All detectors were situated at a distance *R*=15 cm from the center of the target, entry window of each detector was a profile of BGO crystal (of width and height 6.5 cm and 7.6 cm, correspondingly).

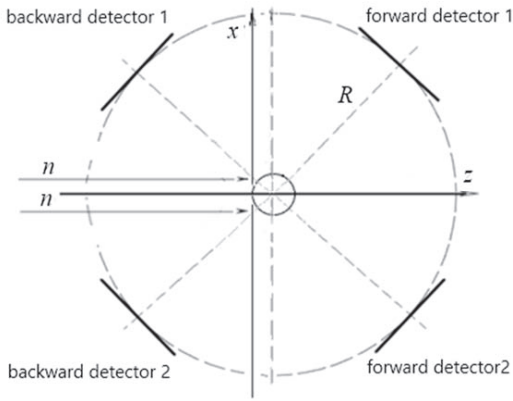

Fig.1. X-Z plane of the scheme for Monte Carlo calculations.

A comparison of the sum of experimental counts of four γ-detectors after subtraction of backgrounds with normalized total neutron capture in the bromine sample calculated at the neutron energies near of 0.88 eV p-wave resonance of ^{81}Br is presented in Fig.2.

The calculated forward-backward asymmetry of γ-quanta detection was obtained as the ratio $A(E)$ at a given energy E of incident neutron:

$$A(E) = \frac{N_{1f}(E) + N_{2f}(E) - N_{1b}(E) - N_{2b}(E)}{N_{1f}(E) + N_{2f}(E) + N_{1b}(E) + N_{2b}(E)},$$

where $N_{1f}(E)$ and $N_{2f}(E)$ are counts of "forward" detectors, $N_{1b}(E)$ and $N_{2b}(E)$ – counts of "backward" detectors. An absolute error of each $A(E)$ ratio taking into account statistic uncertainties of counts were determined by formulae:

$$\Delta A(E) = A(E)\sqrt{\frac{1}{N_{1f}(E) + N_{2f}(E) + N_{1b}(E) + N_{2b}(E)} + \frac{N_{1f}(E) + N_{2f}(E) + N_{1b}(E) + N_{2b}(E)}{\left(N_{1f}(E) + N_{2f}(E) - N_{1b}(E) - N_{2b}(E)\right)^2}}.$$

Fig.3 presents $A(E)$ ratios obtained under condition of isotropy emission of γ-quanta from the points of capture of neutrons in the bromine target, where open points are ratios calculated with γ-quanta from neutrons captured without scattering in the target, and ratios calculated with gammas from all captured neutrons (including multiple scattered ones before capture) are shown by close points. On condition that γ-quanta emission is isotropic in the center-of-mass system, the calculations show a small (less than 1%) "zero" asymmetry effect.

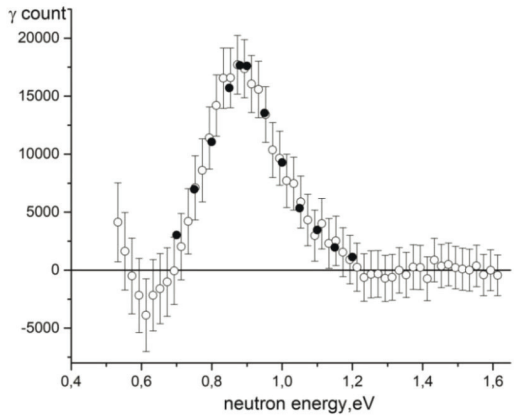

Fig.2. Sum of experimental counts of all γ-detectors without backgrounds (open points with statistical errors) and normalized total neutron capture (close points) calculated for cylindrical bromine sample at the incident neutron energies near of 0.88 eV p-wave resonance of ^{81}Br.

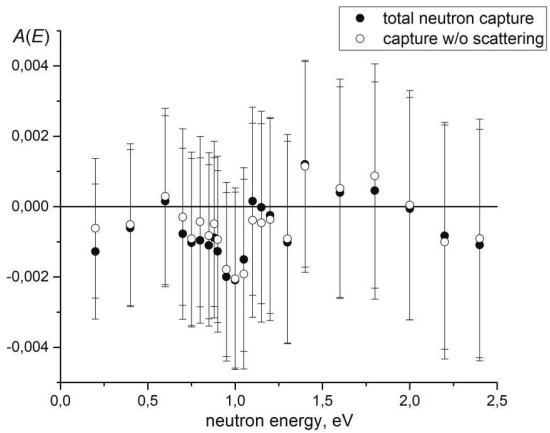

Fig.3. Ratios, $A(E)$, of the "forward" and "backward" detection of γ-quanta under condition of their isotropic emission from ^{81}Br(n,γ) reaction: opened points – $A(E)$ for γ-quanta emitted from points of neutron capture without scattering in the target; closed points – $A(E)$ for γ-quanta emitted from points of total neutron capture.

Unfortunately, our wish to observe the peak of aforesaid 7302 keV γ-transition, in which the forward-backward γ-asymmetry was obtained in [1], in the experimental spectra of amplitudes (Fig. 4) has not been realized because of insufficient resolution of our detectors (position of this γ-transition is marked in Fig. 4 by an arrow).

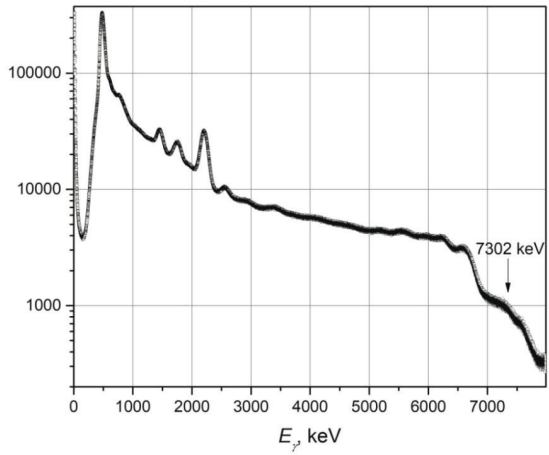

Fig.4. Experimental amplitude spectrum measured by one of the BGO detectors at 11-meter flight path of the IREN facility. Measuring time is 91 hours.

In order to predict an exceedance probability of the forward-backward asymmetry of emitted gammas above "zero" effect level of the unavoidable asymmetry of isotropic gammas detection, for evaluation of a possibility to discover experimentally the forward-backward asymmetry effect of γ-emission in integral γ-spectrum of ^{81}Br(n,γ) reaction, we put a probable asymmetry of gammas into Monte Carlo calculations.

Studying the resonances of low neutron energies, a number of the neutron orbital moments can be limited by a condition $l \leq 2$, and in the conventional Legendre polynomial expansion $\sigma(\theta, E) = \frac{\sigma(E)}{4\pi}(1 + \sum_{i=1}^{\infty} \omega_i(E)\, P_i(cos\theta))$ of a differential cross section of the reaction, the terms with $P_1(cos\theta) = cos\theta$ and with $P_2(cos\theta) = (3cos^2\theta - 1)/2$) are only significant ($\sigma(E)$ is a total cross section), where the coefficient $\omega_1(E)$ just characterizes the required forward-backward asymmetry of the reaction products. So the direction cosine, $cos\theta$, of emitted γ-quantum had to be randomly played using the equation:

$$\int_{-1}^{\xi}(1 + \omega_1(E)x)dx = \gamma \int_{-1}^{1}(1 + \omega_1(E)x)dx,$$

where γ is a random value from interval [-1;1], ξ is required γ-emission direction cosine, and therefore:

$$cos\theta = \frac{-1 + \sqrt{1 - 2\omega_1(E)(1 - \frac{\omega_1(E)}{2} - 2\gamma)}}{\omega_1(E)}. \qquad (1)$$

In the Monte Carlo evaluations there is a need to know the incident-neutron energy dependence of the ω_1 coefficient, and $\omega_1(E)$ was calculated theoretically. These calculations, which result is shown in Fig.5, were done in a frame of Flambaum-Sushkov

formalism for 7302 keV primary γ-transition between the levels with I=3/2$^-$ and J=2$^-$ of the ^{82}Br compound-nucleus in the approximation of two resonances (as in ref. [2]). Parameters of 0.88 eV p-wave resonance ($J^p = 2^-$) and of the nearest s-resonance at 101.1 eV ($J^S = 2^+$) were taken from [3].

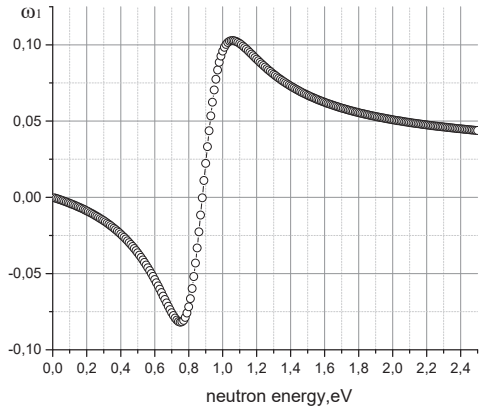

Fig.5. Energy dependence of the coefficient $\omega_1(E)$ for the γ-transition between the levels with I=3/2$^-$ and J=2$^-$ of ^{82}Br nucleus.

To begin, our evaluation were made by assuming that the calculated angular asymmetry is a characteristic property of only 7302 keV γ-transition of the ^{82}Br decay (Fig.6). It is obvious from the comparison of Figs. 6 and 3 that detection of the forward-backward asymmetry of γ-emission from the integral spectra of gammas from ^{81}Br(n,γ) reaction looks impossible in the case of a presence of the required forward-backward asymmetry effect in a chosen 4.6 %-intensity γ-transition line. Moreover, there are circumstances, which also make difficulties for a search forward-backward γ-asymmetry effect in integral spectrum of bromine.

Note once more that natural bromine consists of almost equal parts of ^{79}Br and ^{81}Br isotopes, while their capture cross sections in the region of investigated p-resonance of ^{81}Br are ~6 b and ~1 b, correspondingly. And at these neutron energies, scattering cross section of ^{81}Br is ~6 b, which leads to a considerable multiple scattering (^{79}Br nuclei scatter neutrons two times less than ^{81}Br isotopes). Thus, the bromine target composition essentially distorts the required γ-symmetry effect.

In order to verify this pessimistic fact, Monte-Carlo calculations in the geometry of our experiment were also done for two hypothetical cases:

1) all primary γ-quanta of radiative capture of neutrons by ^{79}Br nucleus are emitted isotropicly, and the direction cosines of emission of all γ-quanta from ^{81}Br(n,γ) reaction were played according to (1) using $\omega_1(E)$ coefficient (as in Fig.5);
2) the target is a sample of pure ^{81}Br isotope (in a cylinder container with diameter 1 cm and high of 10 cm), and the direction cosines of emission of all γ-quanta were played according to (1) using $\omega_1(E)$ coefficient (Fig.5).

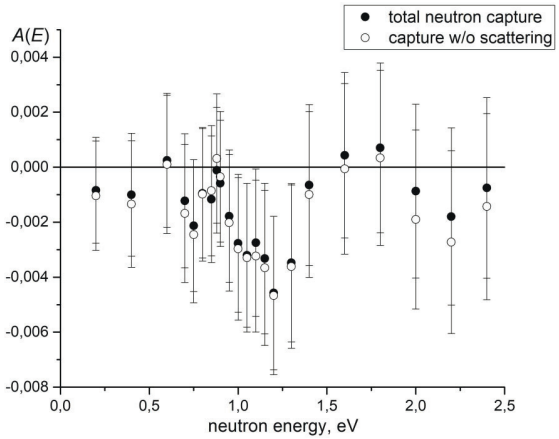

Fig.6. Ratios $A(E)$ if there is 4.6 % asymmetry of γ-emission from ^{81}Br(n,γ) reaction in the bromine target: opened points – $A(E)$ for γ-quanta emitted at neutron capture without scattering; closed points – $A(E)$ for γ-quanta emitted at total capture.

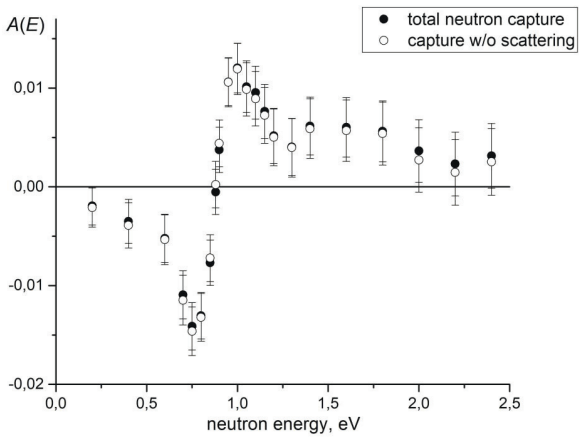

Fig.7. Ratios $A(E)$ on the condition that the asymmetry of γ-emission from ^{81}Br(n,γ) reaction is 100% in the bromine target: opened points – $A(E)$ for γ-quanta emitted at neutron capture without scattering; closed points – $A(E)$ for γ-quanta emitted at total neutron capture.

In the first case, the calculated forward-backward asymmetry of γ-quanta is no more than 3% (see Fig.7), in the second case, the calculations give us reason to think that the asymmetry of γ-emission would be ~13% (Fig.8).

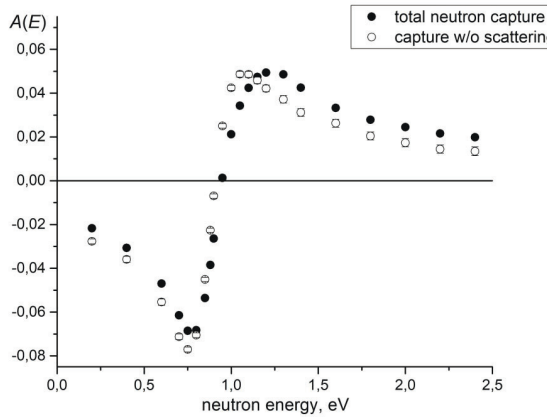

Fig. 8. Ratios $A(E)$ for the target of pure ^{81}Br isotope on the condition that the asymmetry of γ-emission from ^{81}Br (n,γ) reaction is 100%: opened points – $A(E)$ for γ-quanta emitted at neutron capture without scattering; closed points – $A(E)$ for γ-quanta emitted at total capture.

Summary

Our experimental study of the weak 0.88 eV p-wave resonance of the ^{81}Br(n,γ) reaction in order to obtain the forward-backward asymmetry of γ-quanta emission was of no effect.

As a lower limit for the required γ-emission asymmetry in the bromine target, Monte Carlo calculations were performed on the assumption of isotropic γ-emission in real geometry.

The results of Monte Carlo calculations, which were also done with a purpose to clear up a possibility of obtaining of the forward-backward γ-emission asymmetry in the weak low-energy p-wave neutron resonances studying the integral γ-spectra of the ^{81}Br(n,γ) reaction, were quite expected: there may be prospect of obtaining of the required effect in the integral γ-spectrum in the presence of prevailing intense γ-transition of the decay of the resonance under study in mono-isotope target.

References

1. Endo S., Shimizu H.M., Kitaguchi M., Katsuya H., Yamamoto T. et al., Measurement of the angular distribution of γ-rays emitted from the compound state after neutron capture by ^{81}Br for a search of T-violation, EPJ Web Conf., 2019, v. 219, 09003.
2. Oprea A.I., Oprea C., Sedyshev P.V., Gledenov Yu.M., Search of parity violation effects in neutron reaction on natural lead, Romanian Reports in Physics, v. 66, №4 (2014), p.952–962. https://doi.org/10.48550/arXiv.1406.0539
3. Sukhoruchkin S.I., Soroko Z.N., Deriglazov V.V. Tables of Neutron Resonance Parameters. V. 16B. Berlin: Springer-Verlag, 1998. https://doi.org/10.1007/b60147

System of Thermal Stabilization of BGO Scintillation Detectors

A.N. Lihachev[1], R.D. Akmaletdinov[2], Yu.N. Kopatch[1], V.L. Kuznetsov[1,3], L.V. Mitsyna[1], N.V. Rebrova[1], P.V. Sedyshev[1], A. Yergashov[4]

[1]*Frank Laboratory of Neutron Physics, Joint Institute for Nuclear Research, Dubna*
[2]*Institute of Physics and Technology, Ural Federal University, Yekaterinburg, Russia*
[3]*Institute for Nuclear Research of the Russian Academy of Sciences, Moscow, Russia*
[4]*L.N. Gumilyov Eurasian National University, Astana, Republic of Kazakhstan*

Experiments on investigation of angular distributions of γ-quanta emitted in (n,γ) reactions near p-wave neutron resonances with an accuracy better than 10^{-2} are being conducted on the IREN facility, FLNP.

It was found that the scintillation parameters of the BGO crystal are highly temperature-dependent [1]. As temperature increases, the scintillator's light output decreases, and the detector's signal amplitude diminishes. The gain coefficient of PMT also changes with temperature [2]. Therefore, it is necessary to minimize the uncertainties associated with temperature changes during measurement.

The signal amplitude and resolution of a BGO-detector were studied depending on temperature. BGO-detector with the thermal stabilization system is presented in Fig.1.

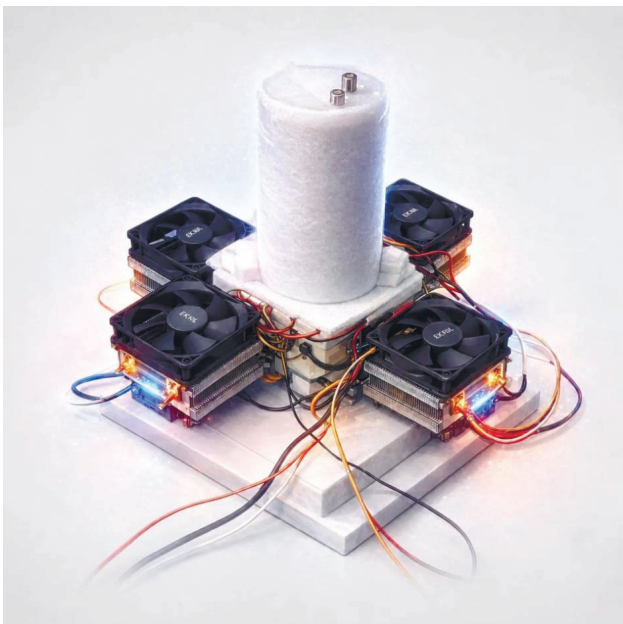

Fig.1. BGO-detector with the thermal stabilization system.

The signal amplitude and resolution of a BGO-detector were studied depending on temperature. A setup consisting of the following components was assembled for this study:

1) scintillation detector is based on bismuth germanate (Bi4Ge3O12). Crystal dimensions are 77.5×65 mm with photomultiplier tube PMT R1307;
2) high-voltage power was supplied by DT803x source. The high voltage on the detector was 1200 V.
3) analog signals from the detector were sent to the CRS-32 digitizer operating at a clock rate of 200 MHz;
4) cooling system

- for thermal insulation – passive (foam),
- for active cooling – 4× TEC1-12706 Peltier elements (parallel), radiators and fans,
- for temperature control – HT-1 sensor with accuracy ±1°C.

Laboratory power supply was used to set the temperature regime of voltage for Peltier elements and fans.

Gamma-quanta spectra were measured with standard calibration sources: Cs-137 (662 keV), Na-22 (511 keV), Co-60 (1173 keV, 1333 keV), and Th-226 (2614 keV).

Gamma-quanta amplitude spectra obtained with cesium, cobalt, and thorium calibration sources at temperatures of 24.4 and -4.4 Celsius degrees are shown in Fig.2. The shift in signal amplitude clearly demonstrates the dependence of the signal amplitude (detector light output) on temperature.

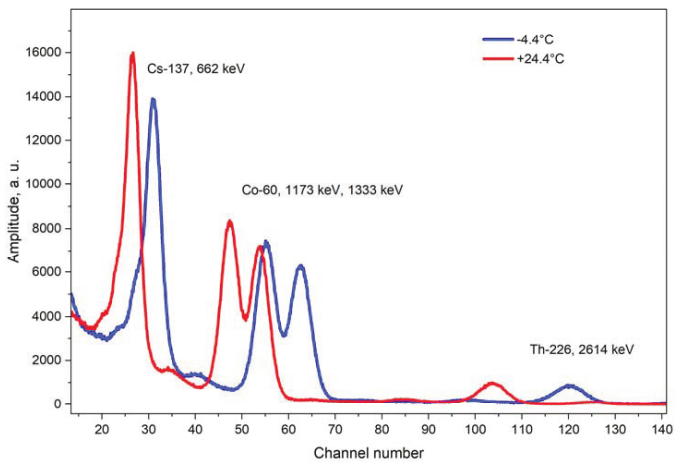

Fig.2. Gamma-quanta amplitude spectra obtained with cesium, cobalt, and thorium calibration sources at temperatures of 24.4^0 and -4.4^0.

The temperature dependence of the BGO-detector (with PMT R1307) amplitude and resolution was studied. The temperature coefficient is $0.6\%/^0C$, which is consistent with known data [3]. Based on the obtained data, a thermal stabilization system was developed that maintains an optimal temperature regime.

Dependence of the signal amplitude and resolution of the BGO detector on temperature for different γ-quanta energies are shown in Figs. 3a and 3b.

It should be noted that in spite of thermal stabilization does not optimize each of components of a combined system (BGO-crystal and PMT) individually, but it rather fixes the total response of the system, as the gain of the PMT during cooling decreases at an increase in the light output of the crystal.

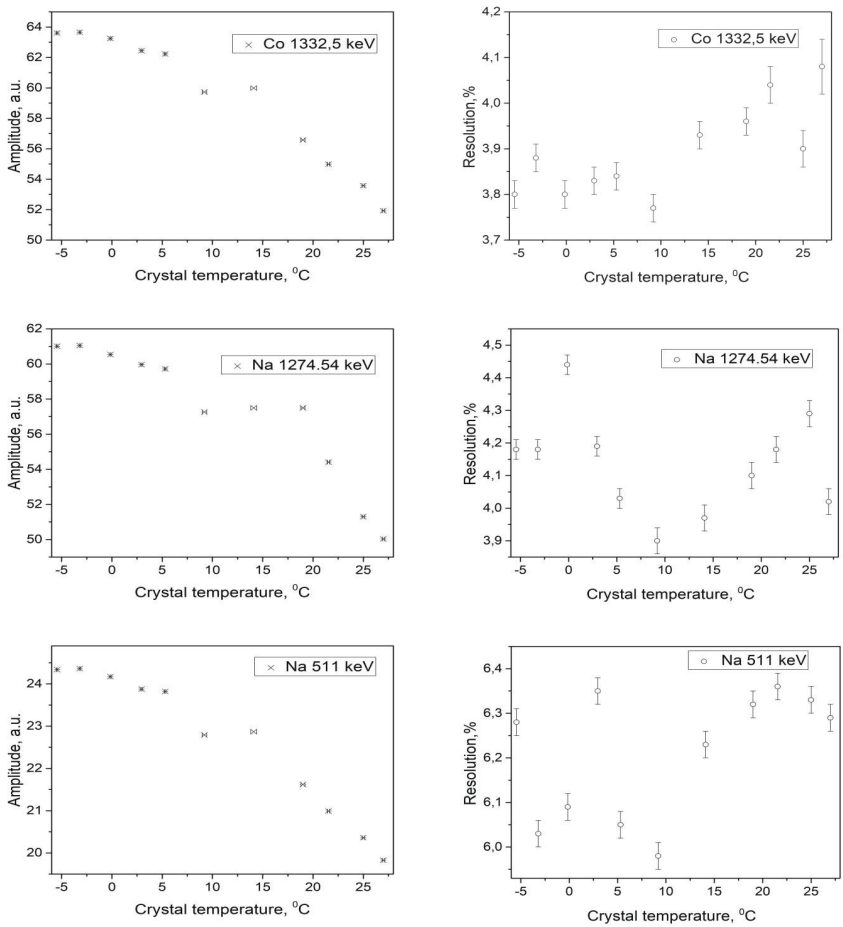

Fig.3a. Temperature dependences of the signal amplitude and resolution of the BGO detector for 1332.5, 1274.54 and 511 keV γ-quanta energies.

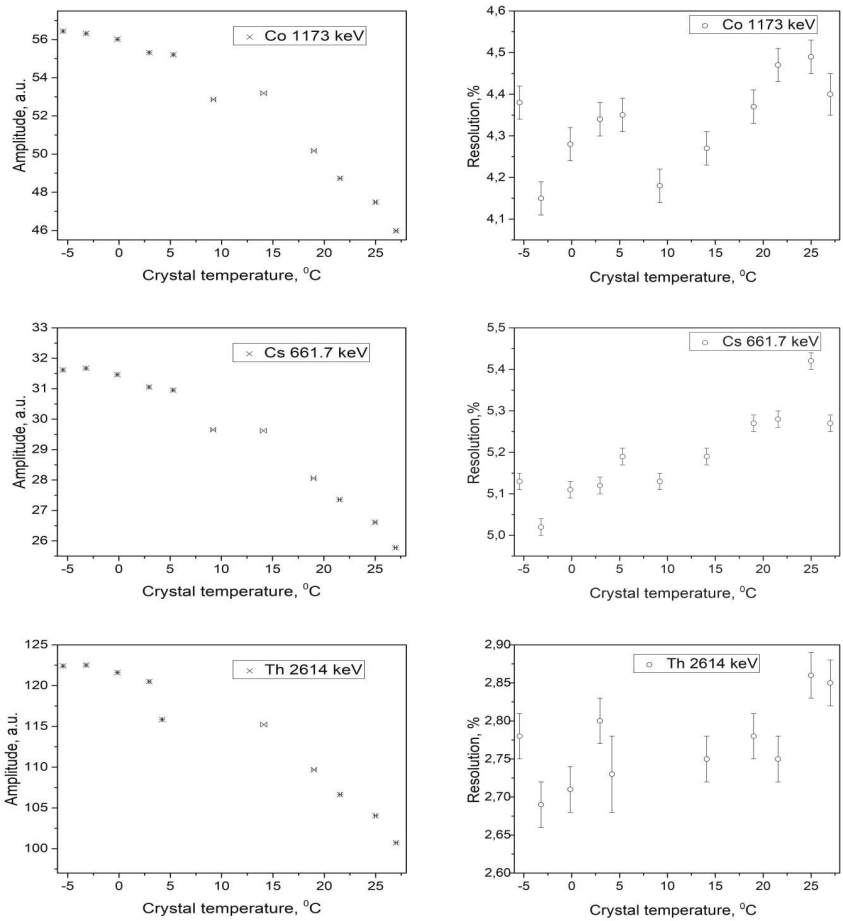

Fig.3b. Temperature dependences of the signal amplitude and resolution of the BGO detector for 1173, 661.7 and 2614 keV γ-quanta energies.

References

1. M.J. Weber, R.R. Monchamp. Luminescence and scintillation of $Bi_4Ge_3O_{12}$. Journal of Applied Physics, 1973.
2. Y. Wang et al, 2006, J. Phys. D: Appl. Phys., 39, 4341.
3. B.V. Grinev, V.D. Ryzhykov, V.P. Seminozhenko. Scintillacionnye detector i sistemy kontrolja radiacii na ih osnove, Kiev, 2007 (in Russian).

From Fermi Total Reflection & Tunneling of Cold Neutrons to Their Trapping in Fabry-Perot Nano-Resonators within the Picosecond Time Regime Precision

M. Maaza

UNESCO-UNISA Africa Chair in Nanosciences and Nanotechnology, College of Graduates Studies, University of South Africa, Muckleneuk Ridge, Pretoria 392, South Africa,
iThemba Laboratory for Accelerator-Based Sciences, National Research Foundation, PO Box 722, Somerset West 7129, South Africa,
African Centre of Competencies in Enhanced Nanosciences and Nanotechnology for SDGs, College of Graduates Studies, University of South Africa, Muckleneuk Ridge, Pretoria 392, South Africa

The precision on the neutron lifetime $\langle\tau_n\rangle$ is of a pivotal importance as it regulates the precision of the 1st element of the Cabibbo-Kobayashi-Maskawa matrix, central to the standard model. The two major methods used to measure $\langle\tau_n\rangle$ while trapping free neutrons, namely, the beam and the bottle methods give different neutron lifetime values; $\langle\tau_n\rangle_{Beam} \sim 888.0 \pm 2.0$ s, that obtained by the bottle technique is smaller; of about $\langle\tau_n\rangle_{Bottle} \sim 879.4 \pm 0.6$ s, besides of the persistent difference of ~10 s within the years, even if the two methods have been modified to enhance the experimental accuracy. This latter was shown to be enhanced if one could trap cold neutrons in Fabry-Perot nano-resonators.

This contribution reports on the neutron tunneling coupled to Fermi total reflection phenomenon & trapping of cold neutrons in a Fabry-Perot nano-resonator. This quantum mechanics trapping allows trapping times of cold neutrons with a precision governed by Heisenberg uncertainty of about 10^{-12} s.

Introduction

Unlike its atomic counterparts, the neutron unique properties facilitate investigations into the four fundamental interactions: the strong, weak, electromagnetic, and gravitational forces. This multi-modal sensitivity renders neutron wave-matter optics a versatile framework for evaluating the postulates of quantum mechanics and broader theoretical physics in general. Although the neutron's existence was theorized in 1920 by Rutherford [1] and confirmed by Chadwick in 1932 [2], its mean lifetime $\langle\tau_n\rangle$ remains a decisive parameter in modern cosmology and a pivotal component of the Standard Model. Specifically, the decay of a free neutron into a proton, an electron, and an antineutrino (Fig.1.a) via a W relaxation dictates the primordial neutron-to-proton ratio n/p during the early universe estimated as n/p ~ $e^{-\Delta m/k_{BTfreeze}} \sim 1/6$ [3−4]. Hence, the accuracy of $\langle\tau_n\rangle$ is essential for predicting primordial nucleosynthesis and for probing physics beyond the Standard Model.

Within the Standard Model, the Cabibbo-Kobayashi-Maskawa matrix involves $\langle\tau_n\rangle$. The unitary tests of the matrix first row, where the sum of squares $|V_{ud}|^2+|V_{us}|^2+|V_{ub}|^2$ [7−8] should equal unity, currently yield to 0.9994±0.0005. Given that the most precise determination of the $|V_{ud}|$ element is derived from neutron lifetime $\langle\tau_n\rangle$ via the relation $|V_{ud}|^2= (4908.7\pm1.9)/(\langle\tau_n\rangle(1+3\varsigma^2)\varsigma)$. The precision on $|V_{ud}|$ is then of a prime importance while governed by the accuracy of the neutron lifetime $\langle\tau_n\rangle$.

In this context, 2 techniques are employed to measure $\langle\tau_n\rangle$ using free neutrons; the beam and the bottle methods [9–10]. Within the years, a significant discrepancy persisted between the results yielded by these 2 approaches (Fig.1.b). The 2 methods denote an average lifetime of $\langle\tau_n\rangle_{Beam}$~ 888.0±2.0 sec [8], and $\langle\tau_n\rangle_{Bottle}$~ 879.4±0.6 sec, respectively [9–11]. The highest precision achieved for the neutron lifetime is 877.75±0.34 s, representing a precision of 0.039%. This recent record-breaking measurement was performed by the UCN collaboration using a magneto-gravitational trap for ultra-cold neutrons. The divergence of ~10 sec has remained unresolved despite enhancements to experimental precision in both methodologies, including the advanced setups such as magneto-gravitational traps [13–14]. The precision achieved via the bottle approach (± 0.34 sec) is superior to the beam method (±2.0 sec). As evidenced in Fig.1.b, the experimental uncertainty associated with the bottle method has progressively decreased over time [10].

A third pathway of trapping neutrons with far higher precision is via an optical trap involving quantum tunneling of neutron wave-packets (Fig.1.c). This latter tunneling being governed by the Heisenberg uncertainly principle [15−23], would allow the highest precision on trapping time so far [24–25].

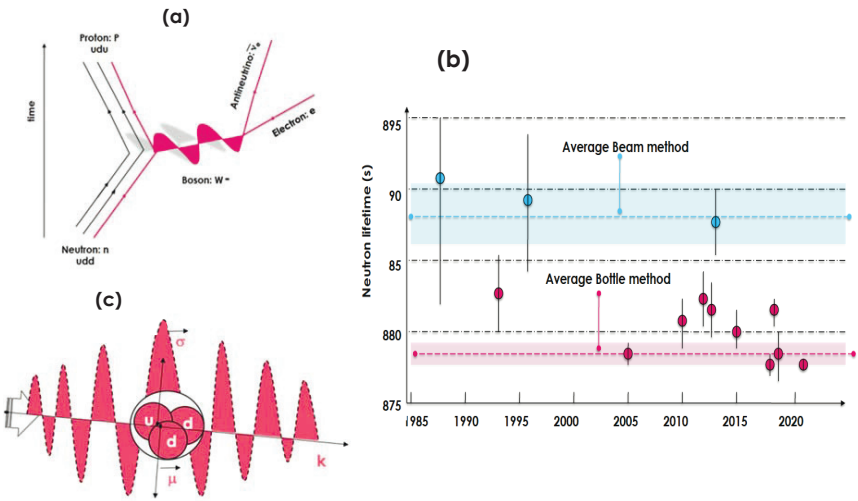

Fig.1: (a) Decay of neutron to a Proton, electron & anti-neutrino, (b) time evolution of the experimental values of $\langle\tau_n\rangle_{Beam}$ & $\langle\tau_n\rangle_{Bottle}$, (c) quantum wave-packet neutron duality.

For such, Fermi total reflection of cold neutrons [26−27] in a Fabry-Perot nano-resonator would be a viable approach [24−25]. Indeed low energy neutrons exhibit a noteworthy wave behavior in line with quantum mechanics De Broglie wave-particle duality (Fig.1.c) [28−33]. Total reflection, interference & interferometry phenomena [26] with specific configurations were validated for trapping neutron wave-packets [16−23]. In fact and, since the observation of the Fermi total reflection of neutrons [26−27], this latter was used to guide neutron beams in modern neutrons guide halls and to evidence the tunneling phenomenon [23].

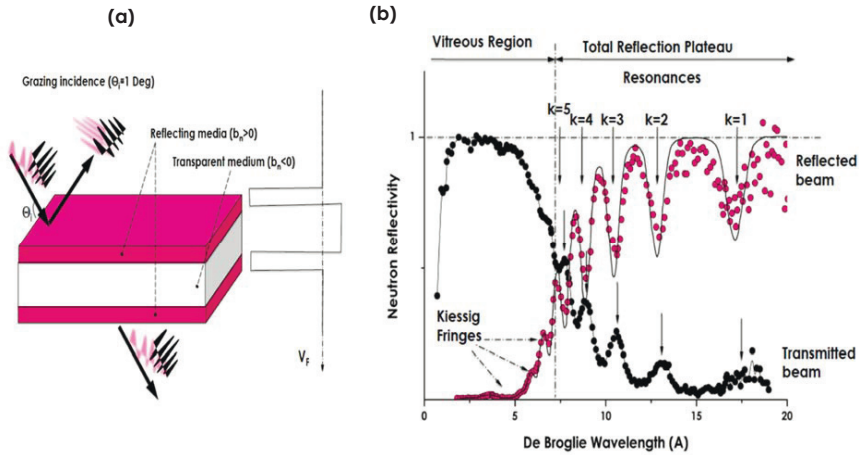

Fig.2: (a) Typical Fabry-Perot nanostructure used to trap cold neutrons consisting of 20 nm nickel/200 nm vanadium/20 nm nickel/10 μm silicon-substrate, (b) its corresponding reflectivity (pink circles) & transmission (black circles).

Table 1: Spectral parameters of the various minima in the total reflection plateau due to the frustrated total reflection in the 200Å Ni/ 2000Å V/ 200Å Ni /Silicon substrate Fabry-Perot nano-resonator, corresponding to the cavity quasi-bound states (ν = 1, 2, 3, 4 and 5). The derived trapping time $\langle\tau_n\rangle_{Trapping} \sim m/(\hbar k \Delta k)$

Resonance order $\boldsymbol{\nu}$	Resonance wavelength $\boldsymbol{\lambda_{res}}$, (Å)	$\boldsymbol{\Delta\lambda_{res}}$ (Å)	$\boldsymbol{k}$ (Å^{-1})	$\boldsymbol{\Delta k}$ (10^{-2} Å^{-1})	Trapping time $\boldsymbol{\tau}$ (ps)
1	17.38	1.09	3.561	2.267	19.35
2	12.99	0.85	4.837	3.165	10.36
3	10.56	0.73	5.950	4.113	6.48
4	9.02	0.61	6.966	4.711	4.83
5	7.87	0.61	7.984	6.188	3.21

Fig. 2.a displays the typical Fabry-Perot nano-resonator for the observation of the neutrons wave-packet tunneling to be trapped. It consists of 2 identical Nickel layers (High neutron reflectors of 200 Å in thickness each/positive nuclear scattering length amplitude) separated by 2000 Å vanadium (transparent neutron medium/negative nuclear scattering length amplitude). The resonator is deposited onto 1μm thickness silicon substrate (Si being a low neutron reflector, low positive nuclear scattering length amplitude) [23].

Fig.2.b reports its corresponding neutron reflectivity & transmission spectra over the neutron associated de Broglie wavelength range of 2−20Å. The polychromatic neutron beam (λ= 2−20 Å) was impinging the nano-resonator under a grazing incidence $\Theta_i \sim 0.8°$ (1.4×10^{-2} rad) with a relative angular resolution $\Delta\Theta_i/\Theta_i \cong 5\times10^{-2}$. More precisely, the experimental neutron reflectivity R and transmission T are reported in a linear scale versus the neutron

wavelength with the simulated curve (for reflectivity profile only). As one can notice, two main regions separated by the critical wavelength of Nickel λ_{CNi} ~ 7.7 Å are observed: the total reflection plateau (above λ_{CNi}) and the so-called vitreous region (below λ_{CNi}). In this latter one, a set of Kiessig fringes occur due mainly to the interference between the partial wave-packets reflected at air-Ni, Ni-V, and Ni-Si interfaces. Their simulation allows one to determine the films' thickness and their interfacial roughness. The derived thicknesses are 20 nm and 205 nm for the Ni and V layers, respectively, while the interfacial roughness is constant of 7 Å.

The second region, which is the main focus of this contribution, is the total reflection plateau (beyond λ_{CNi}), where one crystal-clearly distinguish 5 resolved resonances instead of the constant standard total reflection plateau (R=100%). These resonances assert on the tunneling of specific distinguishable neutron wave-packets within the considered Fabry-Perot nano-resonator. They correspond to neutron wave-packets which tunneled initially through the 1st reflecting Ni layer. Therefore, these are the quasi-bound states (ν = 1, 2, 3, 4, and 5). The characteristics of these resonances, which are correlated to the multiple internal reflections of the trapped neutrons wave-packets within the Vanadium layer before their second tunneling through the second Ni layer deposited onto the Si substrate (Fig.3.a). Their main characteristics are summarized in Table 1. Each resonance coincides to a tunneled peak in the transmission spectrum. The width of these resonances is different; the lower is the order, the larger is the width at half minimum ($\Delta\lambda_{1/2}$). As established, this is correlated to the tunnelled neutron wave-packet trapping time in the resonant cavity $\langle\tau_n\rangle_{Trapping}$. Via the Heisenberg uncertainty, the average associated value is of the order of $\langle\tau_n\rangle_{Trapping} \sim m/(\hbar k\Delta k)$. Accordingly Table 1, this neutron trapping time in the resonant cavity $\langle\tau_n\rangle_{Trapping}$ is derived from the fitting of the experimental data. It is varying approximately from 3.21×10^{-12} s to 19.35×10^{-12} s. During such a trapping time, the neutron wave-packets are trapped inside the high refractive index medium (200 nm vanadium), while totally reflected back and forth at the Ni-V interfaces as schematically represented in the inset of Fig.3.a.

Fig.3.b displays the evolution of the trapping time versus the neutron wavelength. Its evolution might be reasonably described as a quadratic type in form of $\langle\tau_n\rangle_{Trapping} \approx -0.084\lambda + 0.7\lambda^2$. Hence, by extrapolation for ultra-cold neutrons with wavelength of 100 or 1000 nm, $\langle\tau_n\rangle_{Trapping}$ is 7μs and 700.084 μs, respectively. Yet these values are far from the neutron lifetime, however the precision allowed with such an approach is superior as it is within the micron-sec regime in precision.

Consequently, high flux Ultra-cold neutron beams available at ESS (Fig.3.c) would be ideal for neutron trapping in such nano-resonators.

(i) A set of cold neutrons wave-packets have experienced tunneling through both high reflecting barriers of Ni layers (positive nuclear scattering length amplitude).
(ii) The tunneled neutron wave-packets with wavelength higher than λ_{CNi} ~7.7 Å have been trapped within the considered 20 nm Ni/200 nm V/20nm Ni nano-resonator.
(iii) Such neutron wave-packets are trapped inside the high refractive index medium (200 nm vanadium, negative nuclear scattering length amplitude), while totally reflected back and forth at the Ni-V interfaces as schematically represented in the inset of Fig.3.a.
(iv) The larger the wavelength, the longer is the trapping time in the resonant cavity.
(v) The precision of the neutron wave-packets is within the picosecond regime (10^{-12} second).

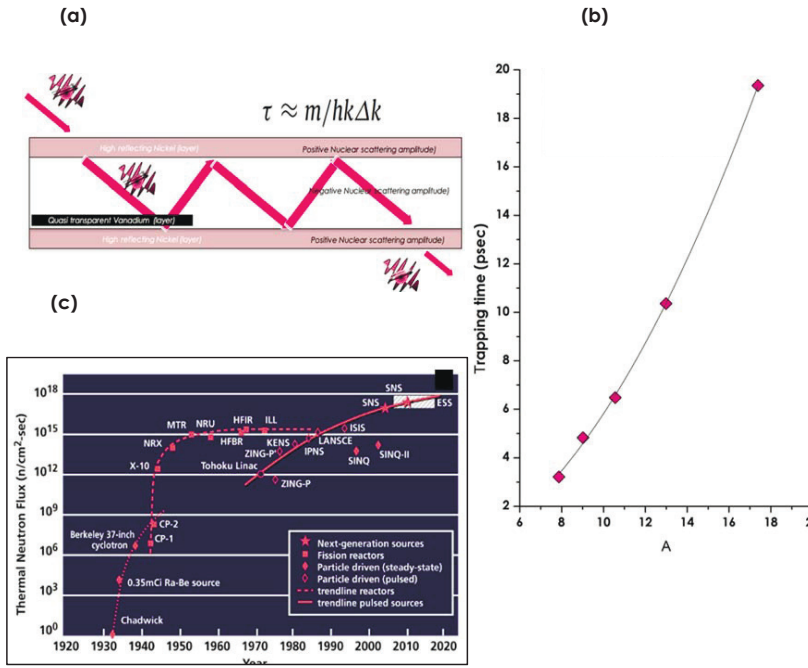

Fig.3: (a) Schematic representation of the tunneling of resonant wave-packets & their trapping within the Fabry-Perot nanostructures, (b): quadratic like variation of the trapping time versus the de Broglie associated wavelength, (c) neutron flux evolution of standard reactor neutron sources & spallation sources within the years.

The above mentioned possibilities necessitate intense cold/ultra-cold neutrons sources such as ESS (Fig3.c) and the support of the neutron scattering community by and large in view of ushering the frontier of cold /ultra-cold neutron physics in general [34−50].

Conclusion

Within this contribution, the possibility of trapping cold neutrons (de Broglie associated wavelength within the range of 7−20 Å) in specific Fabry-Perot nano-resonators was validated. In such single Fabry-Perot nano-resonators, the trapped neutrons manifest themselves through dips in the plateau of total reflection known as frustrated total reflection. In fact such dips correspond to neutron wave-packets which suffered tunneling through the 1st Ni reflecting layer & the 2nd Ni reflecting layer after being trapped within the vanadium layer during a period of $\tau_{nTrapping}$. Such neutron trapping $\tau_{nTrapping}$ is within the range of 3 to 19 picoseconds in the considered Single Fabry-Perot nano-resonators. While the main intention of this contribution is to validate the possibility of trapping cold neutrons in nano-structured Fabry-Perot resonators with a picosecond precision significantly superior to that offered by

the beam method (±2.0 s) or by the bottle method (±0.6 s). It is hoped that these preliminary results would attract the interest of the neutron lifetime community. It might be a possibility to explore the potential of the integration of such trapping in the bottle or beam methods which would assist in elucidating the origin of the neutron lifetime difference between the two approaches.

Acknowledgments

This research project was supported by the CNRS-France, the JINR-Dubna/Russia & the UNESCO -UNISA-ITLABS/NRF Africa Char in Nanosciences & Nanotechnologies (U2ACN2)-South Africa. This contribution is dedicated to Late Dr.D. Korneev (FLNP-JINR), Prof. B. Pardo (IOTA-Orsay), Prof. H. Rauch (ATI-Wien) & Prof. J. Rossat-Mignod (LLB-CEA Saclay).

References

1. E. Rutherford, Proc. Roy.Soc., 97(686): 374–400, (1920).
2. J. Chadwick, Nature, 129:312, (1932).
3. D. Dubbers & M.G. Schmidt, Reviews of Modern Physics, Vol. 83(2011).
4. H. Abele, G. Helm, U. Kania, C. Schmidt, J. Last, and D. Dubbers, Phys. Lett. B 316, 26, (1993).
5. H. Abele & D. Mund, Eds., 2002, Workshop on Quark Mixing, CKM Unitarity, Heidelberg (Mattes-Verlag, Heidelberg). H. Abele, S. Baeßler, and A.Westphal, Lect. Notes Phys. 631, 355, (2003).
6. H. Abele, E. Barberio, D. Dubbers, F. Gluck, J.C. Hardy, W.J. Marciano, A. Serebrov, and N. Severijns, Eur. Phys. J. C 33, 1, (2004).
7. Particle Data Group, M. Tanabashi et al, Phys. Rev. D 98, 030001, (2018).
8. A. Anirban, Nature Rev. Phys 4, 9 (2022).
9. W. Pattie et al., Science, (2018).
10. F.M, Gonzalez, et al. (UCNτ Collaboration), Phys. Rev. Lett. 127, 162501, 2021.
11. Norman F. Ramsey, Physics Reports, 409−421, Vol. 43, Issue 10 (1978).
12. A. Abragam & L.C. Hebel, American. Journal of Physics. 29, 860–861 (1961).
13. V.F. Ezhov et al., Nucl. Instr. and Methods Phys. Res. A 611, 167, (2009).
14. P. Geltenbort, V.F. Ezhov and V.L. Ryabov, Tech. Phys. Lett. 35, 700, (2009).
15. A. Steyerl, K.A. Steinhauser, H. Sheckenhofer, S.S. Malik, Phys. Rev. Lett. 44, 1306, (1980).
16. A. Steyerl, T. Ebisawa, K.A. Steinhauser, M. Utsuro, Z. Phys. B41, 283–290 (1981).
17. A. Steyerl, W. Drexel, S.S. Malik, E. Gutsmeidl, Physica, B 151, 36–43 (1988).
18. Maaza, M., Hamidi, D., Physics Reports, 514(5), 177–198, (2012).
19. M. Maaza, B. Pardo, J.P.Chauvineau, A. Menelle, F. Bridou, Physics Letters, 223(3),145–148, (1996).
20. M. Maaza, B. Pardo, J.P.Chauvineau, F. Bridou, J. Corno, Physics Letters, 235(1), pp.19–23,(1997).
21. M. Maaza, B. Pardo, S. Malik, C. Sella, L.P. Chernenko, D.A. Korneev, Phys. Lett. A 195, 1–8 (1994).
22. M. Maaza, A. Matiwane, J. Sackey, M. Lekala, A. Gibaud, MRS Advances, 10.1557/adv.2018.228, (2018).
23. M. Maaza, L.P. Chernenko, D.A. Korneev, B. Pardo, C. Sella, F. Bridou, Phys. Lett. A 218, 312–318, (1996).

24. M. Maaza, B. Pardo, D. Hamidi, M. Akbari, R. Morad, M. Henini and A. Gibaud, Journal of Neutron Research, 1 (2023) 1–16.
25. Maaza, M., Hamidi, D., Physics Reports 2012, 514(5), pp. 177–198, 10.1016/j.physrep.2012.01.005.
26. E. Fermi, W.H. Zinn, Phys. Rev. 103, 70 (1946).
27. E. Fermi, L. Marshall, Phys. Rev. 71, 666 (1947).
28. V.F. Sears, Oxford University Press, (1989). DOI: https://doi.org/10.1016/0370-1573(82)90151-X.
29. C.G. Shull, Phys. Rev. 179, 752, (1969), doi.org/10.1103/PhysRev.179.752.
30. H. Maier-Leibnitz, T. Springer, Z. Phys. 167, 386, (1962).
31. F.J. Landkammer, Z. Phys. 189,113(1966). DOI: https://doi.org/10.1016/0375-9601(74)90132-7.
32. H. Kurz, H. Rauch, Z. Phys. 220, 419 (1969). DOI: https://doi.org/10.1016/0921-4526(91)90634-Q.
33. H. Rauch, W. Treimer, U. Bonse, Phys. Lett. A 47, 369, (1974)., DOI: https://doi.org/10.1016/0375-9601(74)90132-7.
34. V.I. Luschikov, A.I. Frank, JETP Lett. (USSR)(Engl. Transl.); (United States) 28 (9)(1978).
35. A.I. Frank, P. Geltenbort, M. Jentschel, D.V. Kustov, G.V. Kulin, V.G. Nosov, A.N. Strepetov. Physics of Atomic Nuclei 71 (10), 1656−1674 (2008).
36. A.I. Frank, P. Geltenbort, G.V. Kulin, A.N. Strepetov, Journal of Experimental and Theoretical Physics Letters 78 (4), 188−192 (2003).
37. A.I. Frank, I.V. Bondarenko, A.V. Kozlov, P. Høghøj, G. Ehlers, Physica B: Condensed Matter 297 (1−4), 307−310 (2001).
38. A.I. Frank, Soviet Physics Uspekhi 30 (2), 110−133 (1987).
39. B.G. Erozolimsky, L.N. Bondarenko, Y.A. Mostovoy, B.A. Obinyakov, V.A. Titov, A.I. Frank, Physics Letters B 33 (5), 351−352(1970).
40. A.I. Frank, I.V. Bondarenko, V.V. Vasil'ev, I. Anderson, G. Ehlers, P. Hoghoj, JETP Letters 75 (12)(2002).
41. A.I. Frank, V.G. Nosov, Annals of the New York Academy of Sciences 755 (1), 293−302 (1995).
42. A.I. Frank, V.A. Naumov, Physics of Atomic Nuclei 76 (12), 1423−1433 (2013).
43. M.A. Zakharov, G.V. Kulin, A.I. Frank, The European Physical Journal, D 75 (2), 47 (2021).
44. A.I. Frank, G.V. Kulin, Nuclear Instruments and Methods in Physics Research Section A: Accelerators (2023).
45. M. Spegel, C. Sella, B. Pardo, A. Menelle, J. Corno, R. Gaziel, M. Maaza, Solid state communications, 112 (3), 177−181 (1999).
46. A. Menelle, J.P. Chauvineau, B. Pardo, A. Raynal, F. Bridou, M. Maaza,…, Physica B: Condensed Matter 198 (1−3), 231−234 (1994).
47. L.P. Chernenko, D. Korneev, B. Pardo, C. Sella, F. Bridou, M. Maaza, Physics Letters A 218 (3−6), 312−318 (1999).
48. J.P. Chauvineau, B. Pardo, A. Raynal, A. Menelle, F. Bridou, M. Maaza,…, Solid state communications 111 (1), 23−28 (1999).
49. B. Pardo, S.S. Mallick, F. Bridou, D.A. Korneev, L.P. Chernenko, M. Maaza,…, Physics Letters A 195 (1), 1−8 (1994).
50. C.N.R. Rao, M. Maaza, Journal of the Optical Society of America A, 37 (11), (2020).

Monte Carlo Simulation of the Multi-Detector System of the FISCO Facility

Olkhovich N.M., Tiagelskaia A.M., Vorobyev A.S.

NRC "Kurchatov Institute", B.P. Konstantinov Petersburg Nuclear Physics Institute, 188300, Gatchina, Leningrad district, Russia

Introduction

The use of software packages for modeling experimental installations is a generally accepted standard for justifying the possibility of conducting an experiment. In this regard, for the FISCO installation, it was decided to create a digital twin capable of reproducing the results of previous experiments with acceptable accuracy. The first part of this work will be discussed further.

General description

The FISCO (FISsion COrrelation) facility is designed for multiparametric correlation studies of nuclear fission by neutrons. The general view of the facility is shown in Figure 1. The installation has three main detector systems: a charged particle detector, a multi-section neutron and gamma quantum detector, and a neutron multiplicity detector. In this paper, only a multi-section neutron and gamma-ray detector will be considered.

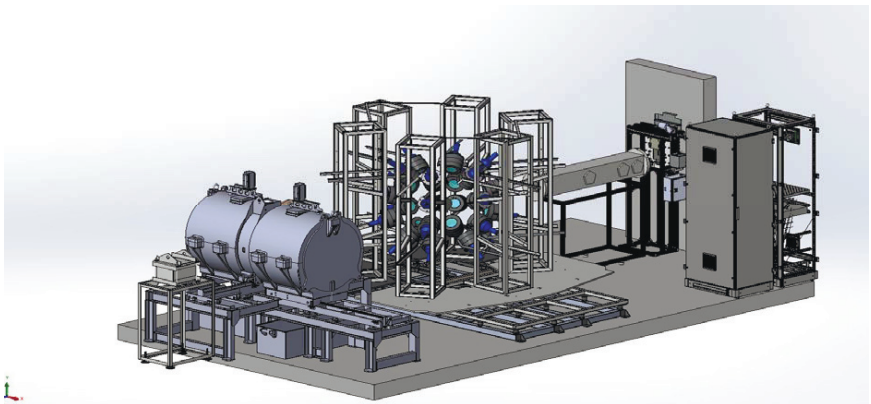

Figure 1. General view of the FISCO facility.

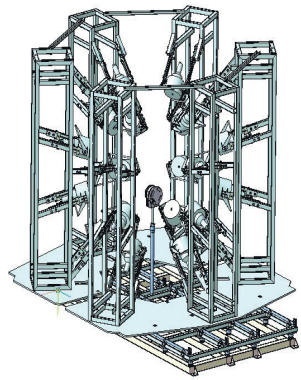

Figure 2. Multi-section neutron and gamma quantum detector.

The multi-section neutron and gamma quantum detector consists of frames with sections with the possibility of their different positioning and detectors in protection inserted into these sections. A general view of a multi-section detector is shown in Figure 2. The types of detectors currently available are shown in Table 1. 24 different detectors can be located simultaneously in a multi-section detector.

The Monte Carlo simulation was performed in the GEANT4 software package. To optimize the calculations, it was decided to abandon ready-made CAD models and create duplicates using the geometric tools built into GEANT4.

Table 1: Characteristics of detectors used in a multi-section detector

	Photomultiplier	Scintillator	Size, mm	Quantity
Type 1	ET9390	EJ-309	D155×H155	12
Type 2	ET9390	NaI(Tl)	D125×H125	12
Type 3	R6233	$LaBr_3$(Ce)	D76.2×H76.2	2

Preparatory work

To confirm the correctness of the detectors simulation, it was decided to simulate the response function from all types of detectors from the Cs-137 calibration source and compare it with experimentally observed amplitude spectra.

The amplitude spectra from the detectors listed in the manufacturer's Data sheets were used as experimental data. The Cs-137 source was located directly on the detector. Calibration was performed to correlate the simulated spectra with the experimental spectra. Figures 3 to 8 show the amplitude spectra taken from the Manufacturer's Data Sheet and the response functions obtained by modeling in GEANT4.

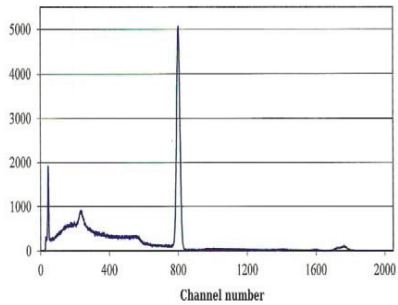

Figure 3. Output from $LaBr_3$ (Passport data).

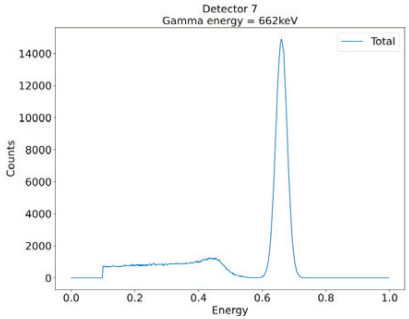

Figure 4. Output from $LaBr_3$ (Calculated data).

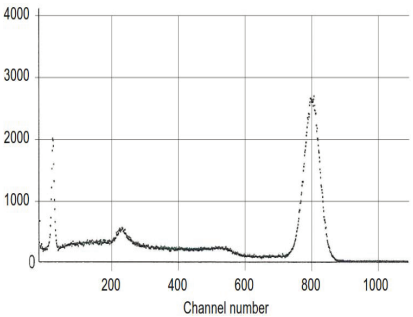

Figure 5. Output from NaI (Passport data).

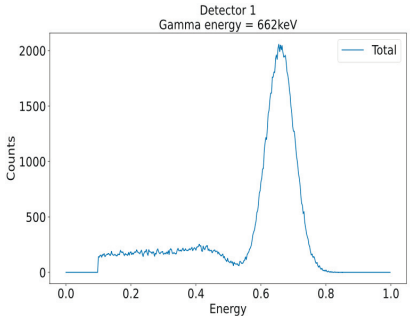

Figure 6. Output from NaI (Calculated data).

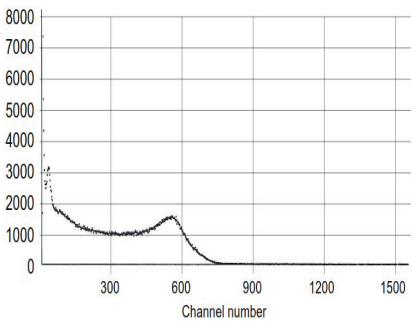

Figure 7. Output from EJ-309 (Passport data).

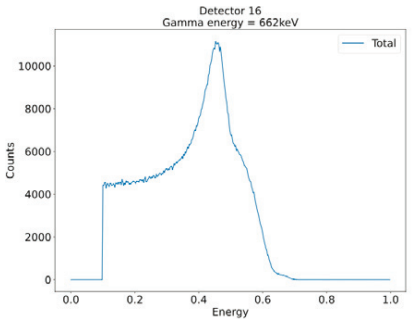

Figure 8. Output from EJ-309 (Calculated data).

A comparative analysis revealed a good consistency of the data obtained during the simulation of the detectors with the data indicated in the passports.

Modeling of a multi-section detector

Moving on to the direct modeling of a multi-section detector, it was decided to use the following layout: detectors with three types of scintillators ($LaBr_3$, NaI, EJ-309) are arranged in a sphere relative to the source at a distance of 90 cm from the center of the detector face. A more detailed arrangement is shown in Table 2. The simulation was performed in the energy range of an isotropic source from 1 MeV to 20 MeV in increments of 1 MeV. A source emitting only one type of particles, either neutrons or gamma quanta, was used in the simulation. The resulting detector responses and calculated efficiencies can be observed in Figures 9−20.

Table 2: Layout diagram of a multi-detector system

OY\OZ	0°	60°	120°	180°	240°	300°
45°	NaI	EJ-309	NaI	EJ-309	NaI	EJ-309
15°	$LaBr_3$	NaI	EJ-309	NaI	EJ-309	NaI
-15°	NaI	EJ-309	NaI	NaI	NaI	$LaBr_3$
-45°	EJ-309	NaI	EJ-309	NaI	EJ-309	EJ309

OY is the axis perpendicular to the floor on which the detector system stands.

OZ is an axis running in a direction perpendicular to OY and dividing the detecting sphere into two equal parts.

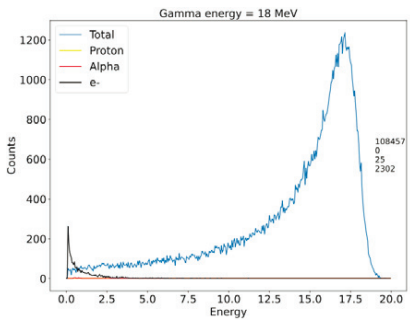

Figure 9. Light output to NaI from gamma quanta with an energy of 18 MeV.

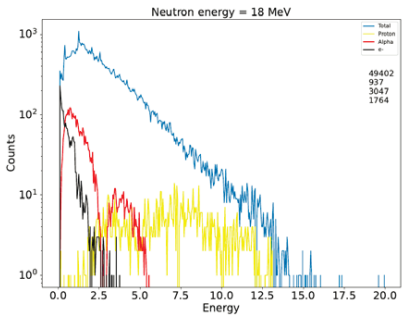

Figure 10. Light output to NaI from neutron with an energy of 18 MeV.

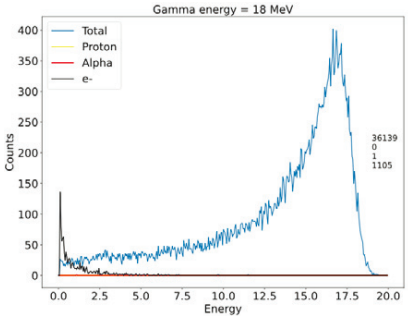

Figure 11. Light output to $LaBr_3$ from gamma quanta with an energy of 18 MeV.

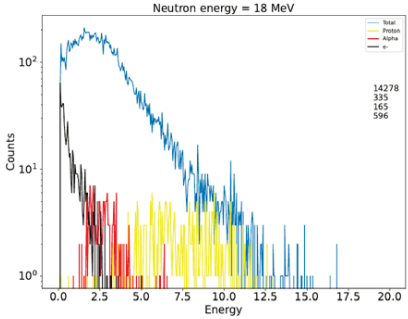

Figure 12. Light output to $LaBr_3$ from neutron with an energy of 18 MeV.

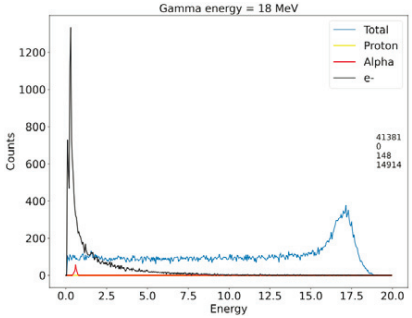

Figure 13. Light output to EJ-309 from gamma quanta with an energy of 18 MeV.

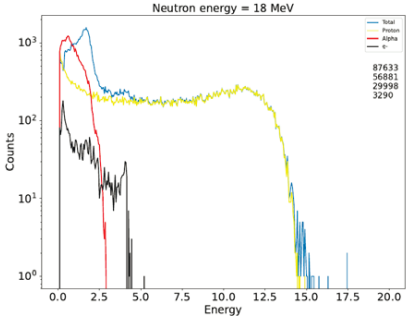

Figure 14. Light output to EJ-309 from neutron with an energy of 18 MeV.

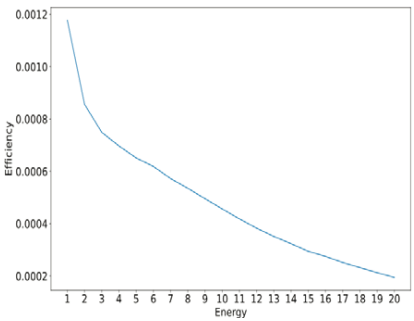

Figure 15. The efficiency of gamma quanta detection on NaI.

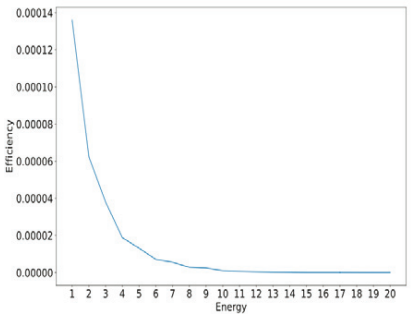

Figure 16. The efficiency of neutron detection on NaI.

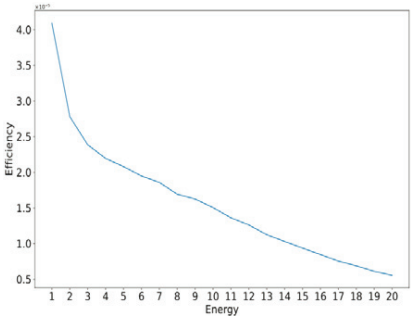

Figure 17. The efficiency of gamma quanta detection on $LaBr_3$.

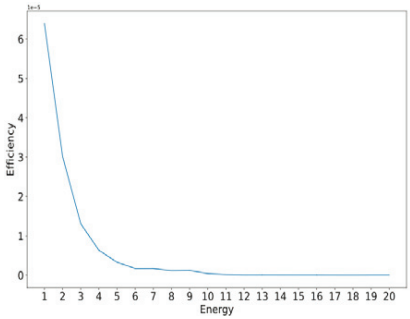

Figure 18. The efficiency of neutron detection on $LaBr_3$.

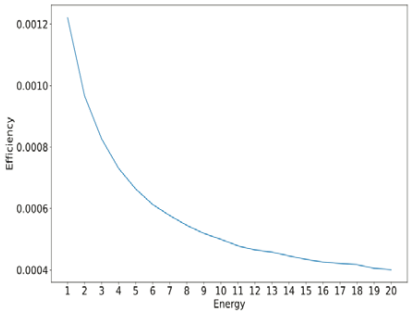

Figure 19. The efficiency of gamma quanta detection on EJ-309.

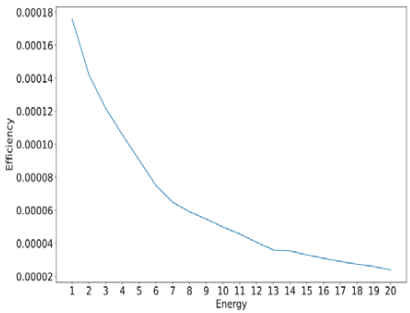

Figure 20. The efficiency of neutron detection on EJ-309.

Conclusion

The response functions from the detectors of a multi-section detector system were modeled for the FISCO facility. Verification of the models of the constructed detectors was carried out separately by comparing the simulated data with the experimental data provided in the manufacturer's Passports. In the future, it is planned to evaluate the contribution to the observed spectra due to crosstalk effects, as well as add other detector systems of the FISCO facility to the digital model for calculation.

References

1. Recent Developments in Geant4, J. Allison et al., Nucl. Instrum. Meth. A 835 (2016) 186−225.
2. Geant4 Developments and Applications, J. Allison et al., IEEE Trans. Nucl. Sci. 53 (2006) 270−278.
3. Geant4 - A Simulation Toolkit, S. Agostinelli et al., Nucl. Instrum. Meth. A 506 (2003) 250−303.

Phytoremediation Potential of *Eichhornia crassipes* for Heavy Metal Removal from Industrial Wastewater Assessed by TXRF

Pham Thi Ngoc Ha[1], Nguyen Thi Nguyet Ha[1], Nguyen An Son[1], Le Hong Khiem[2,3], Inga Zinicovscaia[3], Vu Duc Cong[2,3], Nguyen Thi Minh Sang[1,3*]

[1]*Dalat University, Lam Dong, Viet Nam*
[2]*Institute of Physics, Hanoi, Vietnam*
[3]*Joint Institute for Nuclear Research, Dubna, Russia*

[*]*Corresponding author: sangntm@dlu.edu.vn*

Industrial wastewater often contains toxic elements that pose significant environmental and ecological risks. This study evaluates the phytoremediation potential of *Eichhornia Crassipes* (*E. Crassipes)* for the accumulation of harmful elements from industrial wastewater collected at the Tam Thang Industrial Park, Viet Nam. A static laboratory-scale experiment was carried out for 15 days, during which variations in physicochemical parameters (pH, TDS, temperature, and electrical conductivity), metal concentrations in water, and metal accumulation in plant tissues (roots, stems, and leaves) were monitored. Total reflection X-ray fluorescence (TXRF) technique was employed for multielements analysis. The results showed that the wastewater from the Tam Thang Industrial Park contained twelve elements (Si, S, Cl, K, Ca, Mn, Fe, Cu, Zn, As, Br, and Sr), with iron exhibiting the highest removal efficiency (82.5–87.2%). Elemental analysis of *E. crassipes* tissues revealed elements-specific and timedependent, indicating active uptake and internal allocation processes. Bioconcentration factors (BF) for all analyzed elements exceeded unity, indicating effective uptake from the aqueous phase, while translocation factors (TF) revealed element-specific internal distribution strategies. These findings confirm that *E. crassipes* is a promising phytoremediation species for treating industrial wastewater.

Introduction

Clean water is a fundamental resource for life, playing a key role in protecting public health, ensuring food security, and supporting sustainable social development. According to reports from the United Nations, sustainable management of water resources and sanitation services is essential for long-term development and social stability [1]. However, global water are compromising quality across as a result of rapid industrialization, urban expansion, and climate change. Consequently, the protection and treatment of water resources have become urgent challenges closely linked to the achievement of the Sustainable Development Goals [1, 2].

Water pollution arises from a wide range of sources, among which industrial and municipal wastewater are the most significant contributors to the degradation of surface and groundwater quality. Global assessments related to SDG 6 indicate that the proportion of wastewater receiving adequate treatment remains insufficient, highlighting the need for accelerated action to reduce environmental and public health risks [3].

A variety of wastewater treatment technologies have been developed to address these challenges, including physicochemical methods such as adsorption, precipitation, and ion

exchange, as well as biological. Despite their effectiveness, many of these technologies are associated with high operational costs, substantial energy demand, long treatment times, and the generation of secondary waste in the form of sludge [4−6]. As a result, there is growing interest in alternative treatment approaches that are cost-effective, sustainable, and environmentally friendly.

Phytoremediation using aquatic plants has gained increasing attention as a nature based on solution for wastewater treatment. This approach offers several advantages, including low investment and operating costs, operational simplicity, and minimal secondary pollution. It can be applied either as a supplementary step in conventional treatment systems or as a standalone natural treatment process [6, 7]. By exploiting the natural ability of plants to absorb, accumulate, and detoxify pollutants, phytoremediation has become an increasingly attractive option for wastewater treatment and environmental restoration [6, 8]

Among aquatic plant species, *E. crassipes* has been studied and applied due to its high phytoremediation potential. The species has characterized by rapid growth, high biomass production, and a dense root system, which enable effective pollutant removal even under contaminated water conditions [9−11]

Numerous studies have demonstrated the high capacity of *E. crassipes* to remove heavy metals from aquatic environments, and the specie has been extensively investigated for wastewater treatment applications [10−13]. Review studies have reported that, under certain experimental conditions, removal efficiencies can exceed 70% for metals such as Cu, Al, Pb, Hg, Cd, and As. Nevertheless, these efficiencies vary considerably depending on wastewater characteristics and experimental conditions [11]. Experimental investigations conducted using different water matrices, including industrial wastewater, municipal wastewater, and freshwater, further indicate that phytoremediation performance is strongly influenced by initial pollutant loads and water chemistry. These variations underline the importance of evaluating treatment performance under real wastewater conditions rather than relying solely on artificial solutions.

In Vietnam, rapid urbanization and industrial development have degraded on surface water quality, particularly in coastal cities. Da Nang is a representative example, where several studies have reported the presence of heavy metals in urban rivers and sediments, suggesting potential risks of accumulation and dispersion within aquatic ecosystems [14−17]. In this case, the application of aquatic plant-based treatment solutions, especially those involving locally abundant and highly adaptable species, such as *E. crassipes*, is of practical relevance. Assessing the feasibility of using *E. crassipes* to treat contaminated water in urban environments like Da Nang not only contributes to reducing heavy metal loads but also provides scientific evidence to support environmentally appropriate water management strategies.

Tam Thang Industrial Park is located in the Chu Lai Open Economic Zone, one of the newly developed and large-scale industrial parks in Da Nang, generating industrial wastewater with complex composition. However, there have been no comprehensive studies in Vietnam that evaluate the phytoremediation performance of *E. crassipes* using real industrial wastewater from this area, particularly with respect to temporal variations and metal distribution within plant tissues. Therefore, this study selected wastewater from Tam Thang Industrial Park to assess the practical applicability of *E. crassipes* for treating multi-element industrial contamination.

Driven by the need for sustainable water management, this study aims to evaluate the potential of *E. crassipes* for wastewater treatment at Tam Thang Industrial Park by monitoring environmental parameters, analyzing elemental concentrations in both the water

and plant tissues by using total reflection X-ray fluorescence (TXRF), and examining the mechanisms of metal accumulation and translocation within the plant.

Materials and Methods

The subject used in this study is *E. crassipes*, a common floating aquatic plant with a strong root system noted for its potential to treat heavy metals in water [18, 19]. Plants were collected from areas not directly affected by industrial waste to limit baseline metal content bias. Plants of healthy grow, similar size and morphology were selected (Fig. 1).

After collection, plants were then recovered in well water for 7 days to stabilize. After the recovering stage, a representative sample was analyzed after acclimatization to determine baseline elemental concentrations before the experiment to serve as a comparison point.



Fig. 1. *E. crassipes* recovering in well water.

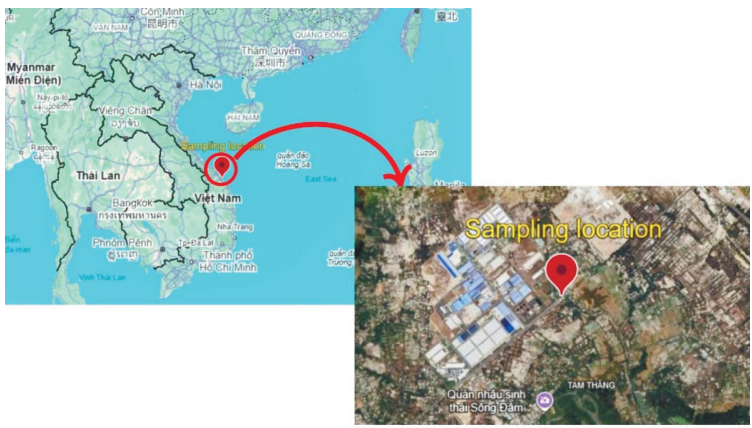

Fig. 2. Sampling area of wastewater.

The wastewater was taken directly from the discharge point of the Tam Thang Industrial Park, Da Nang, Viet Nam (15.626991° N, 108.477920° E). Samples were collected

in pre-cleaned containers rinsed with the wastewater prior to sampling. Initial wastewater samples were analyzed for elemental composition and physicochemical parameters before the experiment. The sampling points are shown in Fig. 2.

The experiment followed a time-series format to assess metal concentration changes in wastewater and accumulation in plant tissues. After the recovering stage, the *E. crassipes* were moved into glass tanks containing wastewater. The experiment was conducted in 100 mL glass tanks under static conditions with no additional chemicals, without aeration or wastewater added throughout the rearing period. Acclimatized plants were transferred into tanks containing industrial wastewater and maintained under natural light and temperature (Fig. 3). Sampling was performed every five days (5, 10, 15, and 20 January 2026). At each sampling time, both wastewater and plant tissues were collected for analysis.



Fig. 3. *E. crassipes* cultivated in a reinforced glass tank containing wastewater.

Water samples were taken at the same intervals as the plant samples. Environmental parameters were measured directly during sampling. The samples were filtered and prepared according to standard TXRF procedures. Multi-element analysis in water and *E. crassipes* sample was performed using a Bruker S2 Picofox TXRF spectrometer (Fig. 4). This method allows for the simultaneous determination of multiple elements with high sensitivity, suitable for the analysis of heavy metals and trace elements in environmental samples, with small sample volumes and short analysis times. The procedure for preparing *E. crassipes* samples for analysis using the TXRF method is shown in Fig. 5.

Water samples were analyzed directly by TXRF using the internal standard method. For plant analysis, *E. crassipe*s samples were rinsed twice with distilled water to remove surface impurities and separated into roots, stems, and leaves to assess organ-specific elemental distribution. The samples were dried to constant weight and finely ground to obtain a homogeneous powder. A representative portion (0.5 g) of the dried material was subjected to microwave-assisted acid digestion (Multiwave GO Plus, Anton Paar) using a mixture of 8 mL HNO_3 (Merck), 0.5 mL HCl (Merck), and 0.5 mL H_2O_2 (Merck). The digestion program consisted of heating to 180 °C for 20 min, holding for 20 min, followed by natural cooling to

room temperature. After the microwave digestion process is complete, the *E. crassipes* sample is completely liquefied. The digested solutions were then spiked with Ga as an internal standard, and an aliquot (10 µg) was deposited onto a pre-cleaned quartz carrier, dried to form a thin layer, and analyzed using an Picofox S2 TXRF spectrometer.

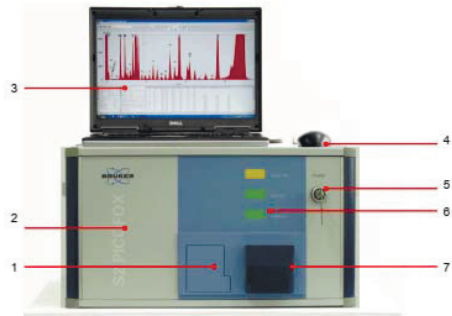

Fig. 4. Picofox S2 TXRF spectrometer system.
1- Adjustment interface, 2 - spectrometer, 3 - controlling computer, 4 - mouse, 5 - key switch, 6 - display for X-ray; power and sample, 7 - sample port.

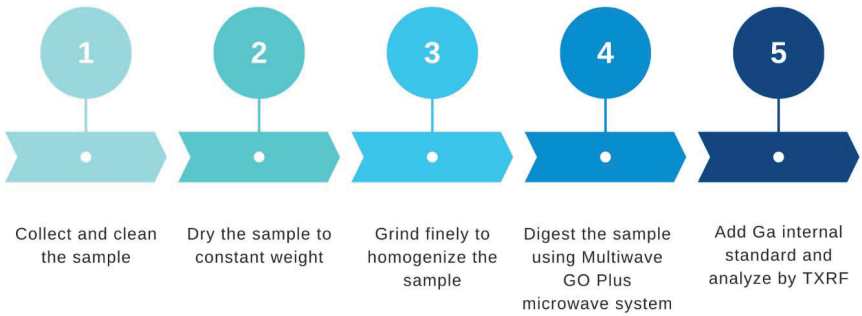

Fig. 5. Procedure for preparing samples for TXRF analysis.

Physicochemical parameters of the wastewater, including pH, electrical conductivity (EC), total dissolved solids (TDS), temperature, and oxidation-reduction potential (ORP), were measured in situ using a portable water quality meter [20].

To evaluate the phytoremediation performance of *E. crassipes*, removal efficiency (RE), bioconcentration factor (BF), and translocation factor (TF) were used as indicators. RE reflects the capacity of the system to reduce metal concentrations in wastewater. BF indicates the accumulation capacity of the plant relative to the metal concentration in water, whereas TF represents the efficiency of metal translocation from roots to aerial parts. These parameters were calculated according to Equations (1), (2) and (3) [21−23]

$$\mathrm{RF}(\%) = \frac{\text{Initial concentration} - \text{Final concentration}}{\text{Initial concentration}} \times 100 \quad (1)$$

$$\mathrm{BF} = \frac{\text{Heavy metal concentration in plant tissue}}{\text{Heavy metal concentration in water}} \quad (2)$$

$$\mathrm{TF} = \frac{\text{Heavy metal accumulation in plant stem/leaf}}{\text{Heavy metal accumulation in plant roof}} \quad (3)$$

Results and discussion

The physicochemical parameters of the wastewater in the *E. crassipes* cultivation tank during the experiment period are presented in Table 1. Throughout the experiment, pH ranged from neutral to slightly alkaline (7.55 to 8.34), temperature remained high (31.3 ºC to 33.5 °C), and EC and TDS values were relatively low, indicating favorable conditions for E. crassipes growth. ORP values were consistently negative, suggesting mildly reducing conditions typical of static biological treatment systems. Neutral-alkaline pH and negative ORP are factors that can affect the form and mobility of metals in the water environment, especially for transition metals such as Fe, Mn, and As. However, these parameters did not fluctuate abruptly, allowing for a relatively reliable assessment of the role of *E. crassipes* in wastewater treatment.

Table 1. Variation of physicochemical parameters of wastewater during the experimental period

	05/01/2026	10/01/2026	15/01/2026	20/01/2026
pH	7.55	7.89	7.96	8,34
EC [µs]	1007	1066	1089	1149
TDS [ppm]	500	533	545	575
T[^{0}C]	32.2	31.3	33.0	33.5
ORP [mV]	-26	-45	-48	-61

In the experiment, the pH ranged from 7.55 to 8.34, falling within the neutral to slightly alkaline range; however, *E. crassipes* has been shown to tolerate a wide pH range from 4 to 10 [24]. The slight upward trend of pH over time indicates that the water environment did not experience sudden fluctuations and remained within the pH range favorable for *E. crassipes* growth. The pH change does not cause any significant stress on the plant. The increase in pH levels in this experiment was caused mainly from the photosynthesis process of the *E. crassipes*. Photosynthesis leads to the consumption of dissolved CO_2 in the water. The reduction of CO_2 reduces carbonic acid and H^+ ion concentrations, therefore causing an increase in pH [25]. This experiment was conducted with a relatively high water temperatures (≈33°C) and favorable lighting conditions, which boosted the photosynthetic intensity of *E. crassipes*. When photosynthesis predominates over respiration, the tendency to alkalize the water environment is an inevitable consequence.

The temperature of the wastewater solution in the experiment was maintained at a high level from 31.3°C to 33.5°C. This is considered a favorable temperature range for the metabolic and photosynthetic processes of tropical aquatic plants such as *E. crassipes*. The optimal temperature range for *E. crassipes* is 25°C to 30°C, but the plant can still grow in the

range of 10°C - 40°C [26]. The high temperature in this study, below 33.5°C, is considered suitable for the growth conditions of *E. crassipes* in a tropical environment. No unusual temperature fluctuations that could negatively affect the plant's physiology were observed.

EC (1007 to 1149 µS/cm) and TDS (500 to 575 mg/L) are considered to be relatively low. *E. crassipes* growth was reduced when EC increased to approximately 4040 µS/cm [26]. Therefore, the EC and TDS levels in this study did not inhibit the growth and development of the plants. Even in the study by Rasool et al. on industrial and urban wastewater treatment, the average EC in industrial area (1746 µS/cm) and urban area (1366 µS/cm) wastewater was higher than in this experiment, yet the plant was still able to survive and accumulate metals [22]. Fluctuations in EC and TDS may be related to ion uptake by plants and ion balance processes within the system, but overall the wastewater environment remains stable.

The ORP values remained negative throughout the cultivation period (from -61 mV to -26 mV), indicating a slightly reducing effect in the wastewater throughout the cultivation period. The negative ORP values and their decreasing trend over time suggest a decline in the wastewater's oxidizing capacity, with reduction reactions becoming more dominant in the system. In biological wastewater treatment systems, the decrease in ORP is commonly related to the consumption of dissolved oxygen and the metabolic activity of the microorganisms, especially under static conditions without supplemental oxygenation. Therefore, the ORP changes observed in this experient are consistent with the nature of biological treatment systems using aquatic plants. However, in this study, the ORP changes over time occurred gradually and did not cause significant disruption to the environmental conditions.

The results of wastewater sample analysis over time using the TXRF method for *E. crassipes* cultivation are presented in Table 2 and Fig. 6. The results show the presence of 12 elements, including: Si, S, Cl, K, Ca, Mn, Fe, Cu, Zn, As, Br, and Sr. These elements were monitored at the initial wastewater time (control sample) and throughout the *E. crassipes* cultivation process.

Table 2. Results of wastewater sample analysis over time

Element	Concentration, mg/l			
	Control sample (05/01/2026)	10/01/2026	15/01/2026	20/01/2026
Si	1068.2	80.9	164.8	163.7
S	107.8	62.2	79.9	117.5
Cl	105.3	72.1	88.8	120.7
K	6.88	6.07	6.76	8.74
Ca	14.87	12.73	13.08	16.39
Mn	0.003	0.002	0.002	0.004
Fe	3.77	0.66	0.56	0.48
Cu	0.004	0.003	0.003	0.002
Zn	0.063	0.034	0.018	0.046
As	0.013	0.006	0.006	0.004
Br	0.183	0.176	0.161	0.158
Sr	0.038	0.036	0.032	0.041

The results demonstrate that the concentrations of elements in the wastewater change significantly during the experiment period. Certain elements, particularly Fe, Br and As, showed a marked and continuous decrease without subsequent recovery, whereas macronutrients such as K and Ca declined initially but exhibited partial rebound at later stages. Overall, the changes in wastewater element concentrations over time demonstrate the combined effect of metal uptake by plants and the physicochemical processes occurring within the wastewater system.

For Fe, the initial concentration in the wastewater reached 3.77 mg/L and decreased sharply to 0.66 mg/L after 5 days, 0.56 mg/L after 10 days, and 0.48 mg/L after 15 days of treatment. The corresponding Fe removal efficiency was approximately 82.5 to 87.2%. This element showed the most significant and stable treatment efficiency throughout the experiment. Previous studies have demonstrated that in *E. crassipes*, Fe is predominantly retained in root tissues, with limited translocation to aerial parts (root > stem > leaf). Such preferential root accumulation reduces the likelihood of rapid re-release into the water column. Consequently, the absence of Fe rebound in this study supports the interpretation that iron removal is governed not only by uptake but also by physicochemical immobilization and rhizosphere retention processes [27]

A comparable continuous decline was also recorded for As. Specifically, As concentrations gradually decreased from 0.013 mg/L to 0.006 mg/L by days 5 and 10, and further to 0.004 mg/L on day 15, representing an overall removal efficiency of approximately 54-69%. Although the removal rate was slower compared to Fe, the steady downward trend demonstrates the plant's capability to reduce dissolved As levels in the aqueous phase. Previous kinetic investigations have shown that *E. crassipes* can effectively take up As under favorable conditions [28]. In addition, *E. crassipes* can remove As from contaminated water and accumulate it in plant tissues, with higher concentrations detected in roots compared to shoots [29]. The consistent reduction observed in this experiment therefore suggests true biological uptake and intracellular accumulation rather than temporary surface binding.

In contrast, K displayed a rebound pattern (6.88, 6.07, 6.76, and 8.74 mg/L). This trend may be related to the physiological characteristics of K in plants. K predominantly exists as a free, osmotically active ion in the cytosol and vacuole and remains largely in soluble form within plant tissues [30]. Unlike many heavy metals, K does not typically form insoluble precipitates in plant tissues. Therefore, its retention may be relatively dynamic, and partial redistribution or release back into the surrounding water could occur over time, which may explain the observed increase in aqueous K concentration [31].

Ca concentration initially decreased from 14.87 to 12.73 mg/l, followed by a gradual increase that ultimately exceeded the control level (16.39 mg/L). The early decline suggests uptake of Ca by *E. crassipes*. Previous studies have reported that *E. crassipes* is capable of accumulating Ca in plant tissues, with concentrations often higher in shoots than in roots [22]. However, the subsequent increase observed at the final stage indicates that Ca removal in the system was not sustained over time. This pattern may reflect the dynamic behavior of Ca in the plant-water system rather than stable sequestration, as observed for certain heavy metals.

For Zn, the concentration decreased from 0.063 mg/L to 0.034 mg/L and 0.018 mg/L at 5 and 10 days, respectively, but increased afterward to 0.046 mg/L on day 15. This trend indicates the non-monotonic fluctuation of Zn in the aqueous phase. However, this fluctuation cannot be concluded as a decrease in the absorption capacity of *E. crassipes*, but rather reflects the dynamic equilibrium of the wastewater-plant system, especially under conditions of low metal concentrations and complex wastewater background.

Cu and Mn exhibited low initial concentrations, so small fluctuations during treatment lead to relatively large changes in percentage, making careful calculation necessary when evaluating the treatment trend for these elements.

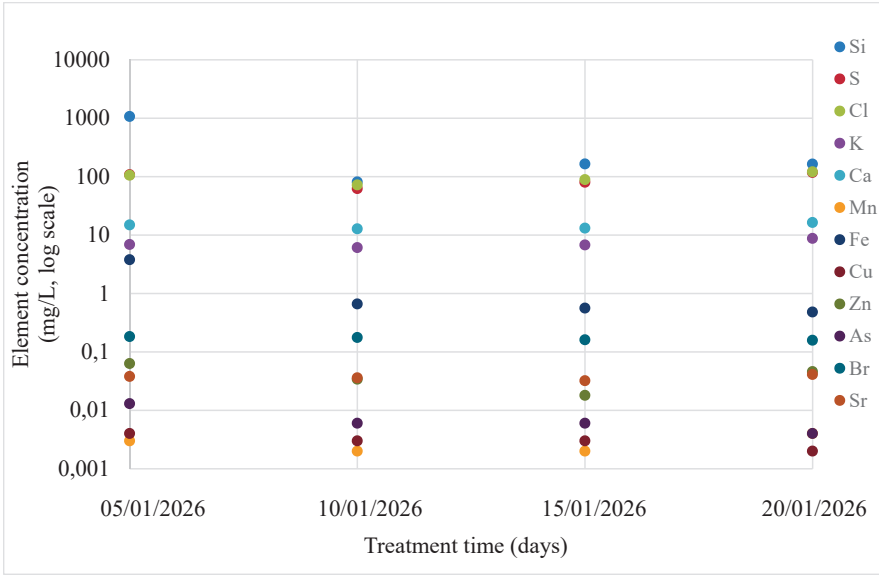

Fig. 6. Temporal variation of elemental concentrations in wastewater during phytoremediation with *E. Crassipes.*

Analysis of *E. crassipes* samples revealed that this study identified 12 elements, including: Si, S, Cl, K, Ca, Mn, Fe, Cu, Zn, As, Br, and Sr (Table 3). The content of these elements was determined separately for three parts of the plant (roots, stems, and leaves) at four sampling times.

Analysis results show that *E. crassipes* has a strong ability to accumulate elements during cultivation, with a distinct distribution between roots, stems, and leaves over time. The accumulation pattern depends on each element, reflecting the characteristic internal absorption, transport, and redistribution mechanisms of each group of substances.

The results showed the following general pattern: nutrient elements such as S, Cl, K, and Ca were present in high concentrations in all parts of the plant, especially the stem and leaves, reflecting their essential physiological roles in the structure and metabolism of E. crassipes. Heavy metals such as Fe, Mn, Cu, Zn, and As exhibited heterogeneous distribution among roots, stems, and leaves, with some elements preferentially accumulating in the roots at specific stages, whereas others showed increased concentrations in the aboveground parts over time.

Table 3. Results of metal analysis in *E. crassipes* sample

El.	Metal concentration in *E. crassipes*, mg/kg											
	05/01/2026			10/01/2026			15/01/2026			20/01/2026		
	roots	stem	leaf	roots	stem	leaf	roots	stem	leaf	roots	stem	leaf
Si	7398	7544	18789	14406	8089	19240	2855	7622	26813	5974	6249	3569
S	1479	1149	1851	1054	1119	1832	1599	1859	2652	1474	2066	2007
Cl	401	1523	3222	832	1129	3590	562	942	4128	748	4360	175
K	4785	30088	35152	3664	23257	44414	6227	25216	44197	15857	15781	9439
Ca	3479	18692	25167	4464	19954	40998	2687	16637	34429	15307	21169	3462
Mn	323	598	786	1504	752	974	909	473	720	490	614	1352
Fe	2714	414	630	5077	575	658	4692	477	400	3513	466	442
Cu	5.11	8.72	11.62	4.47	6.36	15.41	3.14	6.40	14.73	5.82	7.28	4.49
Zn	38.0	35.9	48.9	53.7	32.5	77.8	47.0	47.4	267.3	60.7	56.0	107.3
As	2.24	0.28	0.84	4.45	0.59	1.08	4.73	0.48	10.53	0.78	0.76	6.19
Br	3.95	7.88	7.69	2.52	5.40	11.89	3.43	8.57	6.79	5.56	8.54	0.29
Sr	60.7	224.2	311.2	62.6	199.6	370.2	37.7	196.6	373.1	174.8	155.3	47.3

For Fe, the highest accumulation levels were consistently recorded in the roots at most times, reaching 5077 mg/kg on January 10 and remaining high (4692 mg/kg on January 15; 3513 mg/kg on January 20), while the stem and leaves were significantly lower. This is consistent with the role of the root system in retaining metals through surface adsorption and micro-precipitation [13, 27]. This pattern is consistent with previous studies showing that Fe is predominantly retained in the roots of *E. crassipes* and has a low transport coefficient to the upper parts [20, 27]. The predominant accumulation in the roots limits redistribution back into the aquatic environment, thus explaining the sustained downward trend of Fe in the aqueous phase observed in the experimental system.

As also showed an initial accumulation trend in the roots (4.45 to 4.73 mg/kg mid-stage), followed by a significant increase in the leaves on January 15 (10.53 mg/kg) before a final decrease. Kinetic studies have demonstrated that *E. crassipes* is capable of efficient As absorption and the ability to remove As through accumulation in plant tissues has been noted [28,29]. The distribution pattern in the current study is consistent with bioabsorption and intrinsic transport mechanisms, rather than just surface adsorption.

K and Ca exhibited similar accumulation patterns. Both elements reached very high concentrations in the leaves midway through the experiment, with K fluctuating between 35152 to 44414 mg/kg and Ca peaking at 40998 mg/kg on January 10. The high accumulation of K is consistent with reports that the stems and leaves of *E. crassipes* contain approximately 5 to 6% K by dry weight [32] indicating strong uptake of essential nutrients. K and Ca accumulated primarily in the stem and leaves for most of the experiment, consistent with previous studies on the predominant distribution of K and Ca in the upper tissues of *E. crassipes* [22]. At the final sampling, both K and Ca decreased in the leaves and increased in the roots (root K 15857 mg/kg; root Ca 15307 mg/kg), suggesting internal redistribution as the plant's physiological state changed. This pattern reflects the characteristics of essential macronutrients: they accumulate highly in upper tissues and can be regulated and redistributed among organs over time.

The elements Mn, Cu, Zn, Br, and Sr do not consistently exhibit a dominant accumulation tendency in the roots. The distribution of these elements may be influenced by wastewater composition, competitive interactions between ions, and plant growth conditions. Therefore, the observed variability in this study most likely reflects intrinsic uptake and transport, rather than simple root fixation, suggesting the specificity of the treatment system under the particular experimental conditions.

The bioaccumulation factor (BF) and the translocation factor (TF) are presented in Tables 4 and 5, respectively.

Table 4. Bioaccumulation factor for *E. crassipes* and water samples as of January 20, 2026

Elements	Water (mg/L)	Roots (mg/kg)	BF (L/kg)
Si	164	5974	36.49
S	118	1474	12.54
Cl	121	748	6.20
K	8.744	15857	1813
Ca	16.4	15307	934
Mn	0.004	490	122423
Fe	0.482	3513	7289
Cu	0.002	5.82	2912
Zn	0.046	60.7	1320
As	0.004	0.784	196
Br	0.158	5.56	35.2
Sr	0.04	175	4371

Table 5. Translocation factor as of January 20, 2026

Element	Roots (mg/kg)	Leaf (mg/kg)	TF
Si	5974	3569	0.60
S	1474	2007	1.36
Cl	748	175	0.23
K	15857	9439	0.60
Ca	15307	3462	0.23
Mn	490	1352	2.76
Fe	3531	442	0.13
Cu	5.824	4.494	0.77
Zn	60.7	107.3	1.77
As	0.784	6.188	7.89
Br	5.558	0.294	0.05
Sr	175	47	0.27

The results of the BF calculations indicate that all analyzed elements have BF > 1, demonstrating that *E. crassipes* is capable of efficiently accumulating metals from the water environment. Heavy metals such as Mn, Sr, Cu, Zn, As, and Fe have very high BF values, indicating their highly efficient ability to directly absorb metals from the water into the root system. Notably, despite the very low concentrations of As and Cu in the water (0.002 to 0.004 mg/L), *E. crassipes* was still able to accumulate them in its roots, proving its ability to filter these heavy metals even at trace concentrations. Elements such as K and Ca also have

high BF values, consistent with the characteristics of *E. crassipes*, which has a rapid growth rate and requires many nutrients to maintain its biomass. Conversely, nonmetals and metalloids such as Cl, S, and Si have the lowest BF coefficients, demonstrating that *E. crassipes* exhibits selective adsorption, favoring heavy metals and alkali elements over common nonmetals. The high BF index in the roots confirms that *E. crassipes* is a potential plant for wastewater treatment technology using aquatic plants. The results are consistent with the observation that aquatic plants can accumulate significantly higher concentrations of metals in their tissues compared to the surrounding water environment [19,33,34]

The TF results showed a significant difference between the two groups of elements, reflecting the different accumulation and transport strategies of *E. crassipes*. The group of elements with TF<1, such as Ca, K, Fe, Si, Cl, Sr, had higher accumulation concentrations in the roots than in the leaves. The results indicate that the roots play a crucial role in regulating and accumulating these elements, contributing to a reduction in their concentration in the water through root accumulation. The retention of these elements in the roots is related to the plant's physiological defense mechanisms. For Si, accumulation primarily in the roots may contribute to increased mechanical strength of root cell walls, thereby helping *E. crassipes* adapt better to aquatic environmental conditions and the presence of pollutants [34].

The group with TF>1 includes heavy metals such as Mn, Zn, As, and S. The TF>1 result indicates that a significant portion of these metals are transported from the roots to the leaves, allowing them to bind with organic compounds to reduce toxicity or remove them from the system through biomass harvesting [34]. For S, TF > 1 is appropriate because S is an essential component of proteins and enzymes, so the transport of S to the leaves for metabolic and photosynthetic processes results in TF usually being greater than 1.

This result reflects that under experimental conditions, where elemental concentrations in the water were relatively low and did not induce severe metal stress, *E. crassipes* did not retain all elements exclusively in the roots but allowed them to undergo internal translocation and redistribution within the plant.

Conclusion

This study demonstrates the effectiveness of *E. crassipes* for treating industrial wastewater under static conditions. Environmental parameters remained stable throughout the experiment, providing favorable conditions for plant growth. TXRF analysis revealed the presence of twelve elements in the wastewater, most of which decreased over time, indicating effective removal, with iron exhibiting the highest and most stable removal efficiency (82.5 to 87.2%).

Elemental analysis of *E. crassipes* tissues revealed element-specific, time-dependent distribution patterns, reflecting active uptake and internal allocation within the plant system. Bioconcentration factors exceeded unity for all analyzed elements, confirming efficient uptake from the aqueous phase, even at trace concentrations. Translocation factors revealed element-specific internal distribution strategies, reflecting physiological regulation rather than limitations in uptake capacity.

Overall, the results confirm that *E. crassipes* is a promising phytoremediation species for industrial wastewater from the Tam Thang Industrial Park. Future studies should incorporate plant-free controls, maintain constant water volumes, and use independent experimental units to further clarify removal mechanisms and improve result reliability.

Acknowledgments

This research was supported by the project of Vietnam Ministry of Education and Training (Grant No. B2026-TDL-01). The authors also would like to thank The Joint Institute for Nuclear Research for supporting.

References

1. UNESCO, The United Nations World Water Development Report 2024: Water for Prosperity and Peace. Paris: UNESCO, 2024.
2. Connell D.W., Hawker D.W. Pollution in Tropical Aquatic Systems. Boca Raton: CRC Press, 1992.
3. UN-Habitat, WHO. Progress on wastewater treatment: Global status and acceleration needs for SDG indicator 6.3.1. Nairobi, Geneva: UN-Habitat and WHO, 2021.
4. Ahila K.G., Ravindran B., Muthunarayanan V., Nguyen D.D., Nguyen X.C., Chang S.W., Nguyen V.K., Thamaraiselvi C. Phytoremediation Potential of Freshwater Macrophytes for Treating Dye-Containing Wastewater. Sustainability. Basel: MDPI, 2021. V. 13. P. 329.
5. Ali S., Abbas Z., Rizwan M., Zaheer I., Yavas I., Ünay A., Abdel-Daim M., Bin-Jumah M., Hasanuzzaman M., Kalderis D. Application of Floating Aquatic Plants in Phytoremediation of Heavy Metals Polluted Water: A Review. Sustainability. Basel: MDPI, 2020. V. 12. P. 192.
6. Sharma M., Rawat S., Rautela A. Phytoremediation in sustainable wastewater management: An eco-friendly review of current techniques and future prospects. AQUA - Water Infrastructure, Ecosystems and Society. London: IWA Publishing, 2024. V. 73. P. 1946−1975.
7. Babu S.M.O.F., Hossain M.B., Rahman M.S., Rahman M., Ahmed A.S.S., Hasan M.M., Rakib A., Emran T.B., Xiao J., Simal-Gandara J. Phytoremediation of toxic metals: A sustainable green solution for clean environment. Applied Sciences. Basel: MDPI, 2021. V. 11. P. 10348.
8. Salt D.E., Blaylock M., Kumar N.P.B.A., Dushenkov V., Ensley B.D., Chet I., Raskin I. Phytoremediation: A novel strategy for the removal of toxic metals from the environment using plants. Nature Biotechnology. New York: Nature Publishing Group, 1995. V. 13. P. 468−474.
9. Bhutiani R., Rai N., Sharma P.K., Rausa K., Ahamad F. Phytoremediation efficiency of water hyacinth (E. crassipes), canna (C. indica) and duckweed (L. minor) plants in treatment of sewage water. Environment Conservation Journal. Dehradun: Gurukul Kangri University, 2019. V. 20. P. 143−156.
10. Nasir M., Nur M., Pandiangan D., Mambu S.M., Fauziah S., Raya I., Fudholi A., Irfandi R. Phytoremediation Study of Water Hyacinth (Eichhornia crassipes) on Zinc Metal Ion (Zn^{2+}). International Journal of Design & Nature and Ecodynamics. Edmonton: International Information and Engineering Technology Association, 2022. V. 17. P. 417–422.
11. Monroy-Licht A., Carranza-Lopez L., De la Parra-Guerra A. C., Acevedo-Barrios R. Unlocking the potential of Eichhornia crassipes for wastewater treatment: Phytoremediation of aquatic pollutants, a strategy for advancing Sustainable Development Goal-06 clean water. Environmental Science and Pollution Research. Berlin: Springer, 2024. V. 31. P. 43561−43582.

12. Lu X., Kruatrachue M., Pokethitiyook P., Homyok K. Removal of cadmium and zinc by water hyacinth, Eichhornia crassipes. Science Asia. Bangkok: Science Society of Thailand, 2004. V. 30. P. 93−103.
13. Eid E.M. Uptake prediction of nine heavy metals by Eichhornia crassipes grown in irrigation canals: A biomonitoring approach. Science of the Total Environment. Amsterdam: Elsevier, 2021. V. 782. P. 146887.
14. Khanh N.V., Vinh T.D., Nhi L.H.Y. Contents of heavy metals Hg, Cd, Pb, and Cr in bivalves from estuaries in Central Vietnam. Vietnam Journal of Marine Science and Technology. Hanoi: Vietnam Academy of Science and Technology, 2014. V. 14. P. 385−391.
15. Nguyen V. Khanh, Tran D. Vinh, Kenji Okubo, Kieu T. Kinh, Duong C. Vinh. Assessment of lead and cadmium contamination by sediments and bivalve species from the estuaries in Da Nang City, Vietnam. Journal of Environmental Science for Sustainable Society. 2015. V. 6. P. 1−6.
16. Hang L.T.T., Nhan N.T., Tri N.M. Assess the present status of the water quality of Ban Thach River belonging to Tam Ky City, Quang Nam Province and propose protection solutions. Modern Environmental Science and Engineering. 2021. V. 7. P. 148−153.
17. Hoang M.T., Nam N.X., Thuy T.V., Huyen M.T. Determination of pollution load into Truong Giang River, Quang Nam Province. VNU Journal of Science: Earth and Environmental Sciences. 2018. V. 34. P. 71−79.
18. Zhou J.M., Jiang Z.C., Qin X.Q., Zhang L.K., Huang Q.B., Xu G.L., Dionysiou D.D. Efficiency of Pb, Zn, Cd, and Mn removal from karst water by Eichhornia crassipes. International Journal of Environmental Research and Public Health. 2020. V. 17. Art. 5329.
19. Al-Wagaa A.H., Al-Gburi O., Al-Khafaji A.H. Water hyacinth (Eichhornia crassipes): An efficient plant in removing pollution and treatment of heavy metal in wastewater before flow in the Iraq rivers. Plant Archives. 2019. V. 19. No. 1. P. 505−510.
20. Hanna Instruments Inc. HI991300 & HI991301. Instruction Manual. Woonsocket: Hanna Instruments, 2018. MAN991300.
21. Zayed A., Gowthaman S., Terry N. Phytoaccumulation of trace elements by wetland plants: I. Duckweed. Journal of Environmental Quality. 1998. V. 27. No. 3. P. 715−721.
22. Rasool S., Ahmad I., Jamal A., Saeed M.F., Zakir A., Abbas G., Seleiman M.F., Caballero-Calvo A. Evaluation of phytoremediation potential of an aquatic macrophyte (Eichhornia crassipes) in wastewater treatment. Sustainability. 2023. V. 15. Art. 11533.
23. Ahmad I., Akhtar M., Zahir Z., Naveed M., Mitter B., Sessitsch A. Cadmium-tolerant bacteria induce metal stress tolerance in cereals. Environmental Science and Pollution Research. 2014. V. 21. P. 11054−11065.
24. Gupta A.K., Yadav D. Biological control of water hyacinth. Environmental Contaminants Reviews (ECR). 2020. V. 3. No. 1. P. 37−39.
25. Boyd C.E. pH, Carbon Dioxide, and Alkalinity. Water Quality: An Introduction. Springer, 2015. P. 153−178.
26. Center T.D., Hill M.P., Cordo H., Julien M.H. Water Hyacinth - Biological Control of Invasive Plants in the Eastern United States. USDA, Forest Service, FHTET-2002-04, 2002. P. 41−64.
27. Adelodun A.A., Afolabi N.O., Chaúque E.F.C., Akinwumiju A.S. The Potentials of Eichhornia crassipes for Pb, Cu, and Fe Removal from Polluted Waters. SN Applied Sciences. 2020. V. 2. Art. No. 1646.

28. Souza T.D.D., Borges A.C., Matos A.T., Veloso R.W., Braga A.F. Kinetics of Arsenic Absorption by the Species Eichhornia crassipes and Lemna valdiviana under Optimized Conditions. Chemosphere. 2018. V. 209. P. 866−874.
29. Iqbal, M.T. Mitigation of arsenic by water hyacinths (Eichhornia crassipes) plant. Asian Journal of Water, Environment and Pollution. 2011. V., P. 9−14
30. Marschner, P. Marschner's mineral nutrition of higher plants. Academic Press is an imprint of Elsevier. 2012.
31. Demidchik V., Straltsova D., Medvedev S.S., Pozhvanov G.A., Sokolik A., Yurin V. Stress-induced electrolyte leakage: The role of K^+-permeable channels and involvement in programmed cell death and metabolic adjustment. (5, Ed.) Journal of Experimental Botany. 2014. V. 65, P. 1259−1270.
32. Zhou W., Zhu D., Tan L., Liao S., Hu Z., Hamilton D. Extraction and retrieval of potassium from water hyacinth (Eichhornia crassipes). Bioresource Technology. 2007. V. 98. P. 226−231.
33. Zhang J., Li Y., Liu C., Li F., Zhu L., Qiu Z., Xiao M., Yang Z., Cai Y. Concentration Levels, Biological Enrichment Capacities and Potential Health Risk Assessment of Trace Elements in Eichhornia crassipes from Honghu Lake, China. Scientific Reports. 2019. V. 9. Art. No. 2431.
34. Rezania S., Mat Taib S., Md Din M.F., Dahalan F.A., Kamyab H. Comprehensive Review on Phytotechnology: Heavy Metals Removal by Diverse Aquatic Plants Species from Wastewater. Journal of Hazardous Materials. 2016. V. 318. P. 587−599.

Modeling of the Neutron Beam Parameters of the Time-of-Flight Spectrometer GNEIS Using GEANT4

Tiagelskaia A.M., Olkhovich N.M., Vorobyev A.S.

[1]NRC "Kurchatov Institute", B.P. Konstantinov Petersburg Nuclear Physics Institute, 188300, Gatchina, Leningrad district, Russia

Introduction

The time-of-flight spectrometer GNEIS [1-3] has been operating on the basis of the SC-1000 proton synchrocyclotron with a proton beam energy of 1 GeV at the NRC "Kurchatov Institute" – PNPI (Gatchina). A fast neutron pulse is produced by firing a proton beam at a water-cooled lead target located in the vacuum chamber of the SC-1000. The spectrometer GNEIS is effectively used to study neutrons-nucleus interactions in the neutron energy range from thermal to several hundred MeV, for both fundamental nuclear physics research and applied applications. In these studies, the neutron beam parameters of the spectrometer are of primary importance and are usually determined experimentally. However, additional verification of these parameters should be performed.

Today, the Monte Carlo method is widely used in planning experiments, calculating necessary corrections to measured observables, and also for assessing the possible results. It's worth noting that the power of modern computing technology is such that preliminary calculations can be performed on a desktop computer, without the need for large computing clusters. This significantly accelerates the process of refining approaches and testing the physical models used in the creation of experimental setups.

Some time ago, an attempt was made to simulate the neutron energy spectrum of one of the five neutron beams of the spectrometer GNEIS using the Geant4 package with various physical models (QGSP_INCLXX_HP, QGSP_BIC_HP and QGSP_BERT_HP) [4]. The resources of the computing cluster, which is part of the data processing center of the NRC "Kurchatov Institute" – PNPI, were used. It has been found that in the neutron energy range below 200 MeV the calculation describes the experimental data well, while above 200 MeV the significant difference is observed.

In this work, neutron beam parameters of the testing facility ISNP/GNEIS at the neutron time-of-flight spectrometer GNEIS were calculated on a desktop computer by means of the Monte Carlo method using the Geant4 package. For this purpose, a detailed geometric model of the neutron beam wiring system has been created, and its transmission (efficiency) has been calculated.

General description of the modeling

The geometric model was defined using internal geometric tools for creating figures and areas from the Geant4 package. The physical model QGSP_BIC_AllHP was used.

The schematic view of the neutron beam wiring system of the testing facility ISNP/GNEIS is presented in Fig. 1. This system consists of the vacuum system, the neutron pipeline with Al-windows, the neutron beam shutter and five collimators made of bronze,

steel and brass (K1 – K5). In Fig. 2 the dimensions of the neutron beam shutter, collimators K1 and K2 are shown as well as materials from which they made of. The collimators K3 and K4 were placed in the heavy concrete protecting wall of the main hall of SC-1000 (Fig. 3).

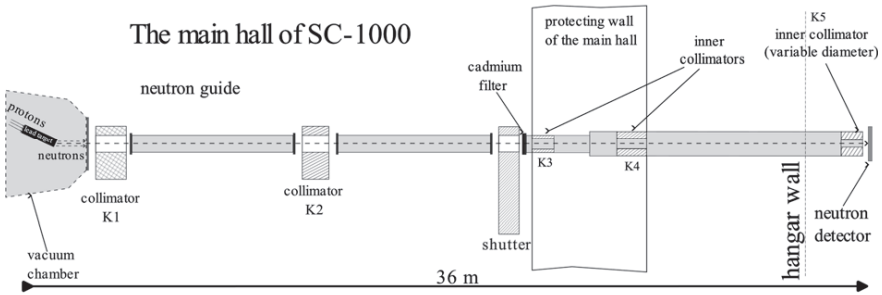

Figure 1. Schematic view of the neutron beam wiring system (not in scale).

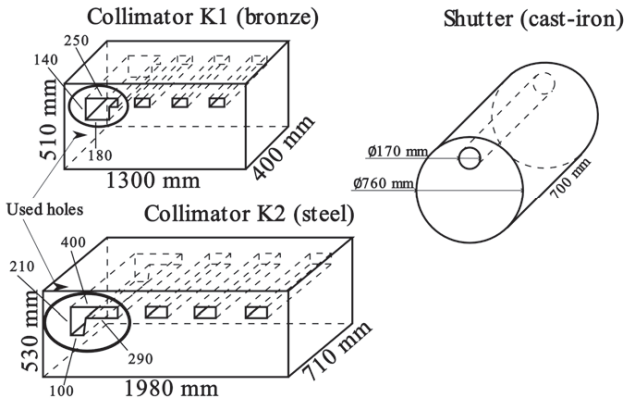

Figure 2. Structure of the neutron beam shutter, K1 and K2 collimators (not in scale). The area highlighted by the circle corresponds to our interests.

The K5 collimator has an adjustable shape and can be replaced depending on the need. In this calculation, the inner diameter of the K5 collimator was set to 50 mm.

Figures 4 and 5 show the created geometric model (digital twin) of the ISNP/GNEIS facility and the results of the particle trajectory generation obtained in Geant4, respectively. The monitoring points 1 (initial beam – at the output of the vacuum chamber of SC-1000) and 2 (beam at the location of the experimental equipment) for which the number of registered events is tracked are also indicated in Fig. 5.

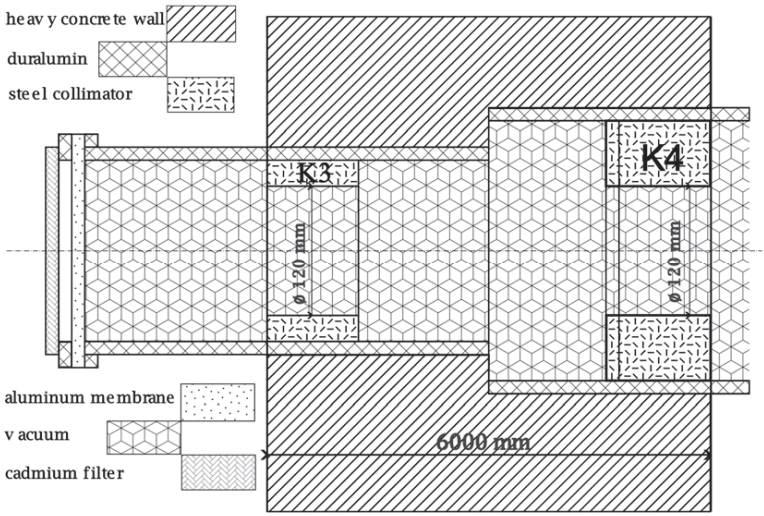

Figure 3. Schematic view of the collimators K3 and K4 of the neutron beam wiring system (not in scale).

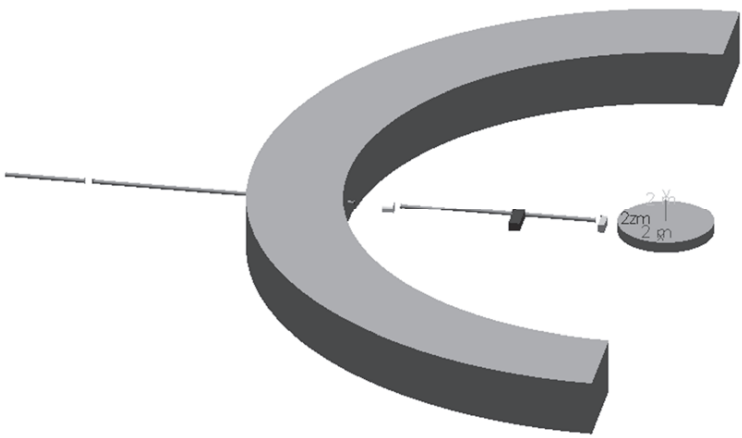

Figure 4. The digital twin of the ISNP/GNEIS facility.

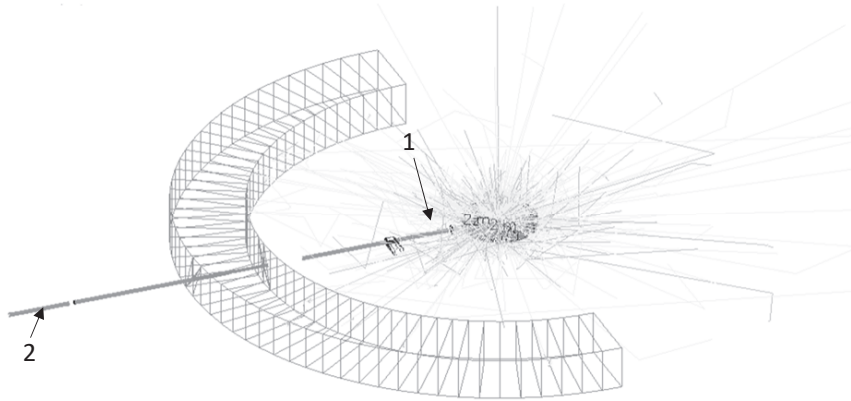

Figure 5. The generated particle tracks.

The construction of the model took place in two stages. At the first stage, the correctness of the arrangement of the facility elements in the model was checked in such a way as to ensure maximum transmission of the target radiation. For this, instead of a neutron production target, a virtual source with equal activity of neutrons and γ-quanta components was placed in the center of the model. This source was a uniform beam of neutrons or γ-quanta with a cross section in the form of a circle with a diameter of 18 cm, which direction was parallel to the axis of the neutron beam wiring system of the testing facility ISNP/GNEIS.

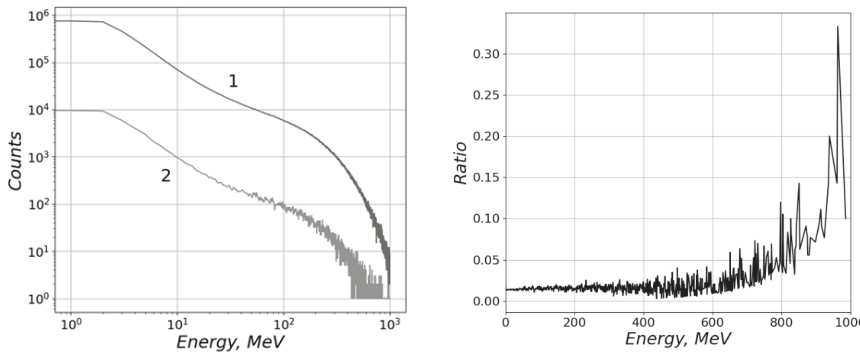

Figure 6. Left - the neutron energy spectra obtained at monitoring points 1 and 2: 1 – initial neutron energy spectrum, 2 – energy spectrum on “detector”. Right – the ratio of spectra at monitoring points 2 and 1.

The energy spectrum of the initial neutrons generated in the source was close to the experimental one [2] while for the initial γ-quanta a uniform distribution from 0 to 10 MeV was used. Figure 6 shows the neutron energy spectra obtained at the monitoring points 1 and 2 (left) as well as their ratio (right). It can be seen that the transmission of neutrons throughout

the wiring system depends on energy - neutrons with higher energy pass to the detector better than neutrons with lower energy (a visible discrepancy begins at about 400 MeV).

At second stage, after adjustments were made to the digital twin of the ISNP/GNEIS facility, the direct calculation has been started. As a result, the neutron energy spectrum has been obtained at the monitoring points 1 and 2 (Fig. 7), however, for point 2 it has not yet been achieved sufficient statistical accuracy. Note the results file contains information about the coordinates and momenta of the registered neutrons because of that it is possible to limit the direction of neutron motion to the solid angle determined by the collimator K2 without any additional calculation. Figure 7 (left) shows the neutron energy spectrum obtained as a result of such limitation in comparison with the original spectrum at the monitoring point 1. Further, using these limited statistics as input parameters for calculations can significantly reduce execution time. This is planned to be done later.

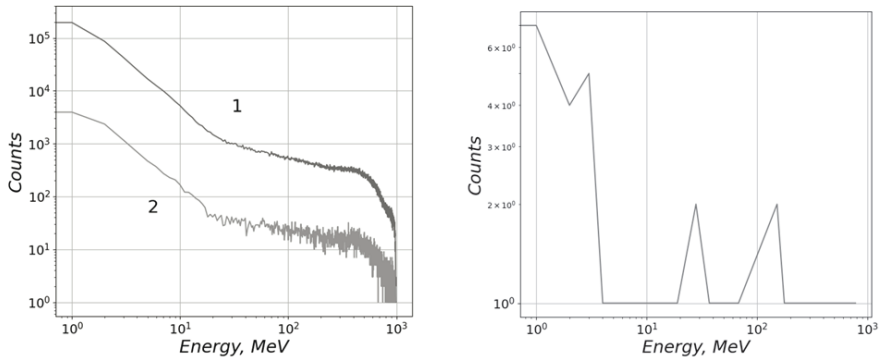

Figure 7. Simulated neutron energy spectrum of the ISNP/GNEIS facility:
(Left) 1 – at the monitoring point 1, 2 – after selecting by the solid angle (see text),
(Right) – at the monitoring point 2.

Results and discussion

As a result of the work using the Geant4 software package, the geometry of the ISNP/GNEIS facility was constructed (with some simplifications). Using the Monte Carlo method implemented in this software package, the geometry was verified by the virtual experiment with a parallel neutron beam of a certain energy spectrum.

The neutron beam parameters of the ISNP/GNEIS facility have been calculated at two monitoring points along the neutron wiring system. But the achieved statistics are not enough to make any precise conclusions.

Conclusion

In the future, it is planned to continue work on complicating the geometry of the facility by adding more real elements to it. It is also planned to increase the number of particle

beam parameters (neutrons and gamma quanta) collected during modeling, and to add modeling of other particles (protons, electrons, etc.). The accumulation of simulated results will continue.

References

1. N.K. Abrosimov, G.Z. Borukhovich, A.B. Laptev et al., Nucl. Inst. Methods, 1985, A242, P. 121.
2. O.A. Shcherbakov, A.S. Vorobyev, A.M. Gagarski, et al., IEEE Transactions of Nuclear Science, 2016, V. 63, No. 4, P. 2152.
3. O.A. Shcherbakov, A.S. Vorobyev, and E.M. Ivanov, Physics of Particles and Nuclei, 2018, V. 49, No. 1, P. 81.
4. A.V. Nakin, A.S. Vorobyev, O.A. Shcherbakov, Physics of Atomic Nuclei, 2019, V. 82, No. 12, P. 1661.

Научное издание

FUNDAMENTAL INTERACTIONS & NEUTRONS, NUCLEAR STRUCTURE, ULTRACOLD NEUTRONS, RELATED TOPICS

XXXII International Seminar on Interaction of Neutrons with Nuclei

Proceedings of the Seminar

ФУНДАМЕНТАЛЬНЫЕ ВЗАИМОДЕЙСТВИЯ И НЕЙТРОНЫ, СТРУКТУРА ЯДРА, УЛЬТРАХОЛОДНЫЕ НЕЙТРОНЫ, СВЯЗАННЫЕ ТЕМЫ

XXXII Международный семинар по взаимодействию нейтронов с ядрами

Труды семинара

Ответственная за подготовку сборника к печати *Л. В. Мицына*.

Сборник отпечатан с файла, предоставленного оргкомитетом.

E3-2026-50

Подписано в печать 06.11.2026
Формат 60×90/16. Бумага офсетная. Печать цифровая
Усл. печ. л. 8,25. Уч.-изд. л. 13,85. Тираж 50 экз. Заказ № 61379

Издательский отдел Объединенного института ядерных исследований
141980, г. Дубна, Московская обл., ул. Жолио-Кюри, 6.
E-mail: publish@jinr.ru
www.jinr.ru/publish/